Nano-Micro Letters
e-ISSN 2150-5551
CN 31-2103/TB
REVIEW
https://doi.org/10.1007/s40820-024-01526-x

Cite as
Nano-Micro Lett.
(2025) 17:33

Received: 12 June 2024
Accepted: 1 September 2024

Optimization Strategies of $Na_3V_2(PO_4)_3$ Cathode Materials for Sodium-Ion Batteries

Jiawen Hu[1], Xinwei Li[1], Qianqian Liang[1], Li Xu[1], Changsheng Ding[1] ✉, Yu Liu[2], Yanfeng Gao[1] ✉

HIGHLIGHTS

- Optimization strategies for high-performance $Na_3V_2(PO_4)_3$ (NVP) cathode material are well summarized and discussed, including carbon coating or modification, foreign-ion doping or substitution and nanostructure and morphology design.
- The foreign-ion doping or substitution is highlighted, involving the Na, V, and PO_4^{3-} sites, which include single-site doping, multiple-site doping, single-ion doping and multiple-ion doping.
- Challenges and future perspectives for high-performance NVP cathode material are presented.

ABSTRACT $Na_3V_2(PO_4)_3$ (NVP) has garnered great attentions as a prospective cathode material for sodium-ion batteries (SIBs) by virtue of its decent theoretical capacity, superior ion conductivity and high structural stability. However, the inherently poor electronic conductivity and sluggish sodium-ion diffusion kinetics of NVP material give rise to inferior rate performance and unsatisfactory energy density, which strictly confine its further application in SIBs. Thus, it is of significance to boost the sodium storage performance of NVP cathode material. Up to now, many methods have been developed to optimize the electrochemical performance of NVP cathode material. In this review, the latest advances in optimization strategies for improving the electrochemical performance of NVP cathode material are well summarized and discussed, including carbon coating or modification, foreign-ion doping or substitution and nanostructure and morphology design. The foreign-ion doping or substitution is highlighted, involving Na, V, and PO_4^{3-} sites, which include single-site doping, multiple-site doping, single-ion doping, multiple-ion doping and so on. Furthermore, the challenges and prospects of high-performance NVP cathode material are also put forward. It is believed that this review can provide a useful reference for designing and developing high-performance NVP cathode material toward the large-scale application in SIBs.

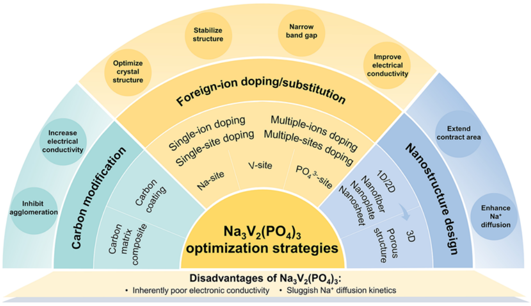

KEYWORDS Sodium-ion batteries; $Na_3V_2(PO_4)_3$; Cathode materials; Electrochemical performance; Optimization strategies

---

✉ Changsheng Ding, dingcs@shu.edu.cn; Yanfeng Gao, yfgao@shu.edu.cn
[1] School of Materials Science and Engineering, Shanghai University, Shanghai 200444, People's Republic of China
[2] Shanghai Institute of Ceramics, Chinese Academy of Sciences, Shanghai 200050, People's Republic of China

1 Introduction

Lithium-ion batteries (LIBs) have been predominant in the energy storage due to their high energy density and energy conversion efficiency compared to other energy storage technologies. However, it is challenging to satisfy the escalating demand of markets for electric vehicles, portable electronic devices and energy storage systems at the same time, originating from the burgeoning consumption and volatile prices of lithium resources [1–4]. To tackle these issues, sodium-ion batteries (SIBs) have been widely proclaimed to be the up-and-coming candidates for grid-scale energy storage systems because of earth-abundant reserves and widespread distribution of sodium resources [5–8]. The energy storage mechanism and battery components are similar for LIBs and SIBs, which enables the fabrication of SIBs to accommodate for the available process equipment of LIBs. More importantly, the cathode and anode of SIBs can adopt cheaper aluminum foil as current collector without involving alloying reaction between Al and Na and overcharging phenomenon, thereby satisfying low-cost and high-safety requirements of energy storage systems [9, 10]. Nevertheless, there remain some challenges and inadequacies in the application of SIBs, including low energy density and unfavorable long-term cycling stability, which limit the popularization and practical application of SIBs [11]. The oversized radius of Na^+ (1.02 nm) compared to Li^+ (0.76 nm) generates larger resistance and volume change during the sodiation/de-sodiation processes, resulting in sluggish diffusion kinetics and diminished electrochemical performance. In addition, the higher redox potential of Na/Na^+ (− 2.71 V) has an intrinsically negative effect on the energy density of SIBs compared with Li/Li^+ (− 3.02 V) [12–14].

The electrode materials greatly affect the electrochemical performance of SIBs. Up to now, a myriad of researchers have endeavored to seek for appropriate electrode materials for high-performance SIBs [15–20]. The choice of cathode material has a significant effect on the improvement of energy density of SIBs. At present stage, the advanced cathode materials are mainly divided into three types: layered transition metal oxides [21, 22], Prussian blue analogs [23, 24] and polyanionic compounds [17]. Although layered metal oxides possess an admirable theoretical capacity of about 240 mAh g^{-1}, the interlayer sliding and complex phase transitions during cycling process bring about severe lattice collapse and inferior cycling stability with rapid capacity decay [25]. Prussian blue analogs, with commercial advantages of low-cost and convenient synthesis, present excellent electrochemical properties. Unfortunately, they generally suffer from high interstitial water content (> 10%) within the framework, resulting in drastic structural collapse and capacity fading [26]. In contrast, polyanionic compounds with Na superionic conductor (NASICON) structure have been deemed as promising cathode materials owing to their robust and open three-dimensional (3D) skeletal structure, high ionic conductivity and good thermal stability [17, 27–30]. The NASICON-type materials as solid-state electrolytes were firstly proposed by Goodenough et al. [31]. Currently, numerous NASICON-type compounds have been reported widely and applied as electrodes or electrolytes for SIBs. The formula of NASICON-type materials can be represented as $Na_xM_2(XO_4)_3$, where x is the sodium content ($x = 0$ to 4), M is transition metal (M = V, Cr, Fe, Ti, Mn, etc.) and X is P, Si, Mo, etc. [32–34]. The stable structure of $Na_xM_2(XO_4)_3$ characterized by the strong binding energy of M–O chemical bond not only facilitates efficient migration of Na^+ but also mitigates volume variation during the Na^+ extraction and insertion processes, contributing to enhanced rate capability and cycling stability. Additionally, their flexible frameworks, with fine tunability, offer compatible structures and beneficial components meeting with multifunctional requirements of high-performance cathode materials [35].

As a typical NASICON-type cathode material, $Na_3V_2(PO_4)_3$ (NVP), with high structural stability and ionic conductivity, has received huge attention in a worldwide, which is similar to $LiFePO_4$ cathode material for LIBs [36, 37]. NVP can deliver a high reversible capacity of about 117.6 mAh g^{-1} and a stable voltage platform of about 3.4 V, corresponding to a favorable energy density of about 400 Wh kg^{-1} in theory. On account of the tunable NASICON system in NVP, there exist ample ion channels that can be constructed for fast Na^+ migration during high-rate cycling process, and thus NVP can obtain superior ion conductivity (10^{-9} to 10^{-11} cm^2 s^{-1}) [38, 39]. Furthermore, the high structural stability of NVP, only generating a minimal volume change (8.26%), can achieve long-term cycling stability in SIBs [39–41]. Unfortunately, NVP still confronts with two obstacles, intrinsically poor electronic conductivity and slow two-phase reaction ($Na_3V_2(PO_4)_3$ to $Na_1V_2(PO_4)_3$), leading to suboptimal rate performance and

https://doi.org/10.1007/s40820-024-01526-x

sluggish diffusion kinetics [42]. Therefore, it is urgent to optimize the overall electrochemical performance of NVP for fulfilling its commercial application in high-performance SIBs.

Up to present, enormous efforts have been carried out on the optimization of NVP cathode material, and many optimization strategies have been proposed to boost the electrochemical performance of NVP cathode material. There are some reviews that have focused on the polyanion NVP material in the recent few years [43–46]. It is noteworthy that these reviews provide some information on the crystal structure, electronic structure, electrochemical performance, preparation methods and modification strategies of NVP electrode material. For instance, the review [43] mainly focused on the crystal structure and electronic structure of NVP and summarized partly the modification strategies, only including ion doping or substitution and carbon coating. However, there was no exhaustive elaboration on the ion doping or substitution. The review [44] summarized comprehensively the synthesis approaches of NVP material and introduced some modification strategies and practical application of NVP in full cell. But it seems to be lacking of excellent organization and detailed discussion for the optimization strategy of foreign-ion substitution. The review [45] only reviewed partial modification strategies of NVP including carbon coating, foreign-ion doping and construction of heterogeneous composite materials. However, the discussion on the modification strategies was not comprehensive. The review [46] introduced the progress of NASICON framework electrodes, including NASICON-type electrode materials, synthesis approaches, computational investigation and partial strategies for electronic conductivity enhancement. Nowadays, the reviews on detailed and critical optimization strategies based on the latest progress of NVP are still scarce, especially systematical and comprehensive discussion. Hence, in this review, we will summarize the latest advances in the optimization strategies for improving the electrochemical performance of NVP cathode material in a fresh perspective, and clarify their effects on the sodium storage performance of NVP, which are of great significance to further develop high-performance NASICON-type cathode materials for SIBs. Three kinds of optimization strategies are mainly discussed, including carbon coating or modification, foreign-ion doping or substitution and nanostructure and morphology design, as shown in Fig. 1. Among them, the foreign-ion doping or substitution is highlighted, which involves the replacement in the Na, V and PO_4^{3-} sites, including single-site doping, multiple-site doping, single-ion doping, multiple-ion doping and so on. Furthermore, this review provides the prospects and challenges of NVP cathode material. It is believed that this review will be beneficial to guiding the design of high-performance NVP cathode material and promoting large-scale applications of NVP cathodes in the near future.

2 Structure and Electrochemical Performance of $Na_3V_2(PO_4)_3$

2.1 Crystal Structure

NVP possesses a rhombohedral lattice system belonging to R3 $\overline{c}$ space group (the hexagonal cell parameter: $a = b = 8.74$ Å and $c = 21.84$ Å), which is in good agreement with the first-principle calculation [46]. As shown in Fig. 2a, in the crystal structure of NVP, two octahedral VO_6 are connected to three tetrahedral PO_4 mutually to form a rigid 3D open skeleton $(V_2PO_4)_3$ resembling "lantern" unit which interlinks each other along the c-axis. Additionally, there are two different interstitial spaces for Na ion sites located at independent oxygen environments: Na1 site has sixfold coordination (CN = 6) at 6*b* sites along the c-axis and Na2 site has eightfold coordination (CN = 8) at 18e sites along the b-axis, in which the occupancy rates of Na atoms are 0.843 and 0.719, respectively [47]. The Na ions occupied at Na2 sites are more susceptible to be extracted during the electrochemical reaction process because of the relatively smaller Na2-O bond compared to the Na1-O bond

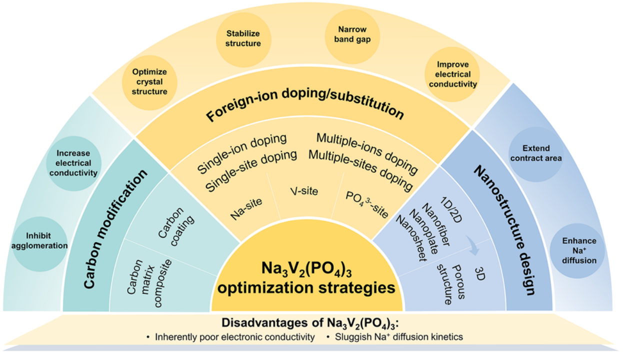

Fig. 1 Outline of optimization strategies for improving the electrochemical performance of NVP cathode materials

[43]. More importantly, the high corner-sharing structure with large interstitial spaces can provide a great number of Na ion channels and generate a low volume change (8.26%) for achieving high ionic conductivity and stable reversible cycle life. Furthermore, the high-angle annular dark field (HAADF)-scanning transmission electron microscopy (STEM) images of $NaV_2(PO_4)_3$ and $Na_3V_2(PO_4)_3$ along $[1\overline{11}]$ are displayed in Fig. 2b [35]. It is discernible that the phosphorus atoms (green spheres) and vanadium atoms (red spheres) in $NaV_2(PO_4)_3$ and $Na_3V_2(PO_4)_3$ frameworks still remain well consistency with the same structure after Na ion's extraction, demonstrating a highly reversible stability during the process of two-phase reaction of Na ions in the NASICON skeleton [48].

The migration mechanism and pathway of Na ions have been identified in the NASICON-type $Na_3V_2(PO_4)_3$ structure with the help of first-principles computations, including three types of channels: pathway1, pathway2 and pathway3 [49]. As depicted in Fig. 2c, there exist pathway1 along the x direction and pathway2 along the y direction, corresponding to similar and favored migration energies of 0.0904 and 0.11774 eV, respectively. It is not feasible for Na ion's migrating along the z direction owing to the high energy barrier (over 200 eV). Thus, the pathway3 will undergo a curved course, which will bypass the octahedron VO_6 and move into the gap between the adjacent tetrahedral PO_4 and octahedral VO_6, attributing to the possible activation energy of 2.438 eV. Moreover, the migration pathways of Na ions have been investigated not only at Na2 sites but also at Na1 sites, where Na ions are mobile in NVP framework. Wang et al. [50] proposed that the Na ions at Na1 sites would also engage in migration progress during the intercalation and deintercalation processes. The periodic density functional theory (DFT) simulations revealed three types of sodium-ion transportation routes in the NVP lattice. The first way of Na ion migration was directly from Na1 site to Na2 site with a highly activation barrier of 36.1 kcal mol^{-1}, which was unfavorable. As shown in Fig. 2d, there remained two kinds of similar ion-diffusion ways focused on the Na2 site to adjacent Na2 site. The path A followed a direct course with high energy barrier of 63.22 kcal mol^{-1} and the path B was divided into two sequential steps, which formed a Na1 vacancy in an intermediate state. Compared with path A, the path B, named as concerted ion-exchange route, had lower activation barrier of 14.0 kcal mol^{-1} and thermodynamic energy. Therefore, it is significant to understand the electrochemical performance of $Na_3V_2(PO_4)_3$ cathode based on the structure and migration behavior of Na ions in the NVP framework.

2.2 Electrochemical Performance

The electrochemical performance of NVP material mainly registers as its capacity, cycling stability and rate capability. In the cyclic voltammetry (CV) curves of NVP material, as displayed in Fig. 2e, there were two redox couples corresponding to V^{3+}/V^{4+} and V^{2+}/V^{3+} redox peaks at 3.4 and 1.6 V [51], respectively. In the high voltage of 3.4 V, two Na ions located at Na2 sites simultaneously involved in the reversible deintercalation and intercalation processes accompanied by two-phase transition reaction between $Na_3V_2(PO_4)_3$ and $NaV_2(PO_4)_3$, providing a theoretical capacity of 117.6 mAh g^{-1}. In fact, it is a difficult thing to achieve the theoretical capacity for pure NVP cathode material (Fig. 2f) [40, 52, 53]. For example, Dong et al. [54] reported that the NVP/C material only presented an initial capacity of 72.5 mAh g^{-1} at 1 C and lower capacity of 65.6 mAh g^{-1} after 100 cycles. For the relatively lower voltage platform, one additional Na ion would be intercalated into the Na2 site, providing 58.8 mAh g^{-1} capacity [55]. Consequently, it plays a vital role for NVP to be reasonably applied as cathode or anode with the electrochemical reactions as follows [56]:

$$\text{Anode reaction: } Na_3V_2^{3+}(PO_4)_3 + xNa^+ + xe^- \leftrightarrow Na_{3+x}V_{2-x}^{3+}V_x^{2+}(PO_4)_3 \tag{1}$$

$$\text{Cathode reaction: } Na_3V_2^{3+}(PO_4)_3 \leftrightarrow Na_{3-x}V_{2-x}^{3+}V_x^{4+}(PO_4)_3 + xNa^+ + xe^- \tag{2}$$

$$\text{Overall reaction: } Na_3V_2^{3+}(PO_4)_3 \leftrightarrow Na_{3-x}V_{2-x}^{3+}V_x^{4+}(PO_4)_3 + Na_{3+x}V_{2-x}^{3+}V_x^{2+}(PO_4)_3 \tag{3}$$

Additionally, some studies indicated that the additional reduction peak at about 3.2 V would also occur owing to the arrangement of Na ions by migrating from Na1 site to Na2 site in the local redox environment (Fig. 2g), while the peak disappeared fully after several cycles [57]. It is an amazing phenomenon that the appearance and disappearance of reduction peak at about 3.2 V did

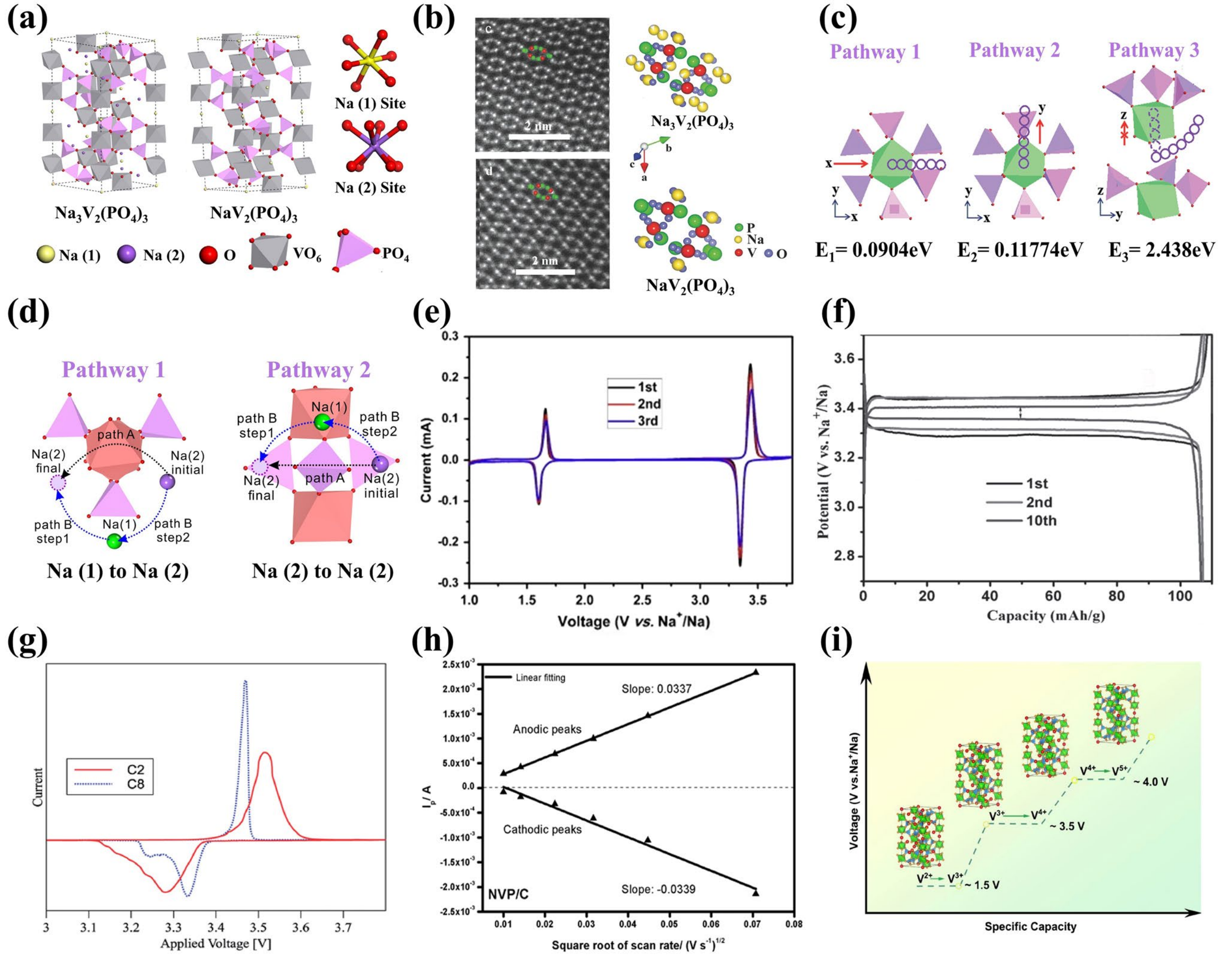

Fig. 2 **a** Crystal structures of $Na_3V_2(PO_4)_3$ material. Reproduced with permission. [47] Copyright 2017, Elsevier. **b** STEM-HAADF images of $Na_3V_2(PO_4)_3$ and $NaV_2(PO_4)_3$ along the $[1\overline{1}\overline{1}]$ projection. Reproduced with permission. [35] Copyright 2014, John Wiley and Sons. **c** Possible migration pathways of Na^+ in NVP lattice. Reproduced with permission. [49] Copyright 2014, Royal Society of Chemistry. **d** Sketch map of the direct diffusion route (path A) and stepwise ion-exchange route (path B) for Na migration. Reproduced with permission. [50] Copyright 2018, American Chemical Society. **e** CV curves of $Na_3V_2(PO_4)_3$/C. Reproduced with permission. [51] Copyright 2011, Elsevier. **f** Charge–discharge curves of $Na_3V_2(PO_4)_3$. Reproduced with permission. [40] Copyright 2013, Wiley-VCH. **g** CV curves of C2 (carbon content 1.76%) and C8 (carbon content 6.95%). Reproduced with permission. [57] Copyright 2016, Royal Society of Chemistry. **h** Relationship between I_p and $\nu^{1/2}$ for NVP/C. Reproduced with permission. [54] Copyright 2021, Author(s). **i** Schematic illustration of multiple $V^{2+}/V^{3+}/V^{4+}/V^{5+}$ redox reactions in NVP cathode. Reproduced with permission. [53] Copyright 2022, Elsevier

not affect the capacity of NVP [58]. Diffusion coefficient of Na^+ (D_{Na+}) of the pristine NVP can be calculated from the CV curves at different scan rates. An extremely low D_{Na+} of 4.05×10^{-11} cm^2 s^{-1} for the anodic reaction and 4.10×10^{-11} cm^2 s^{-1} for the cathodic reaction were obtained during the charge and discharge processes (Fig. 2h) [54], suggesting a sluggish kinetic characteristic of Na ion migration in the NVP. Thus, the pristine NVP cathode material exhibited low rate capability and poor cycling stability.

Furthermore, it has been a popular avenue to oxide V^{4+} to V^{5+} reversibly accompanied by more than two Na ions at a higher operating potential, resulting in improved specific capacity and energy density of NVP cathode (Fig. 2i) [53, 59, 60]. However, the electrochemical performance of pure NVP remains inadequate, which is attributed to two reasons briefly: (1) the weak intrinsic electronic conductivity with a wide bandgap, leading to poor rate performance and smaller specific capacity [61]; and (2) the larger size of Na ions impeding ion's transport, causing sluggish ion-diffusion kinetics and inferior cycling stability. Therefore, it is highly worthy of research to improve the overall electrochemical performance of NVP for achieving the desirable application in SIBs.

3 Optimization Strategies of $Na_3V_2(PO_4)_3$ Material

To enhance the electrochemical performance, numerous optimization strategies have been proposed and applied to NVP cathode material for the promotion of the overall conductivity and ion-diffusion ability [62–65]. In this section, the optimization strategies of NVP cathode material can be summarized into three aspects: (1) carbon coating or modification, (2) foreign-ion doping or substitution and (3) nanostructure and morphology design.

3.1 Carbon Coating or Modification

The coating or modification of carbon materials, which can boost the extrinsic conductivity dramatically, is an effective optimization strategy to improve the electrochemical properties of NVP [66]. Generally, the coating or modification of carbon materials can be divided into two methods, carbon coating and carbon matrix compositing, based on the current research progress and development trends [67–70]. Most of carbon coating or modification commonly contains high carbon loading content for preparing NVP/C composites, while the low carbon loading content with an appropriate thickness of carbon coating layer keeps challenging and also plays an amazing part in boosting the apparent electrical conductivity and electrochemical activity of NVP material. Table 1 gives the comparison of electrochemical performance of some reported NVP/C cathode materials based on the carbon coating or modification strategies.

3.1.1 Carbon Coating

The carbon coating has been extensively used to polish up the sodium storage performance of electrode materials owing to its facile preparing process and effective functions. The carbon coating on NVP can be achieved by solid-state reaction [71, 72], sol–gel method [73, 74], spray-drying method [75], electrospinning [76, 77] and other preparation methods [78–80]. The conductive carbon coating on the surface of NVP not only increases the electronic conductivity but also reduces the side reactions between NVP and electrolyte, as shown in Fig. 3a [81]. In general, the function of carbon coating layer is inevitably influenced by two factors. One is the thickness of carbon coating layer, which plays a critical role in affecting the electrochemical properties of NVP cathode and serves as a buffer layer to alleviate the volume change during the charge and discharge processes. Specifically, too thick carbon coating layer may impede the Na^+ mobility resulting in poor electrical conductivity [82], while too thin carbon coating layer cannot protect the crystal structure of NVP leading to unreliable structure stability during the electrochemical reaction process. The other one is the weight fraction of carbon layer, which exists an appropriate value because the high carbon content may impair the electrochemical activity of NVP [80]. Shen et al. [81] discussed the influence of different carbon contents (5, 7.5, 10, 12.5 and 15 wt%) on carbon-coated NVP materials, and found that the NVP/C nanocomposites with 10 wt% carbon showed a splendid enhancement of reversibility of Na^+ insertion/extraction, exhibiting 124.1 mAh g^{-1} discharge capacity at 0.1 C with 95% capacity retention after 120 cycles (Fig. 3b). Noticeably, the NVP/C-10% cathode revealed the best rate capability compared to other samples (Fig. 3c). Additionally, the conventional carbon sources for carbon coating are mainly commercially available organic compounds, such as citric acid [58, 83–85], glucose [68], polyethylene glycol [86] and oxalic acid [87, 88]. Kate et al. [58] constructed a graphitic and porous nanostructured carbon layer on NVP using citric acid as carbon source by sol–gel method. The NVP/C revealed many beneficial pores attributed to the thermal pyrolysis of citric acid at high temperature of 900 °C, and these pores increased the contact area of electrode and electrolyte and offered more active sites (Fig. 3d), boosting diffusion kinetics with rapid ion-transport rate.

https://doi.org/10.1007/s40820-024-01526-x

Table 1 Electrochemical performance of some published carbon-modified NVP cathode materials

Cathode material	Carbon source	Discharge capacity (mAh g^{-1})/Rate	Capacity retention/Cycles/Rate	Refs
$Na_3V_2(PO_4)_3$@C	Critic acid	99, 1 C	94%, 1400, 10 C	[58]
$Na_3V_2(PO_4)_3$/C-GA	Critic acid and graphene	104, 0.2 C	95.2%, 250, 0.1 C	[84]
$Na_3V_2(PO_4)_3$/C	Ethylene glycol	118, 0.2 C	81.5%, 1000, 10 C	[68]
$Na_3V_2(PO_4)_3$/C	Glucose	124.1, 0.1 C	83.9%, 10,000, 20 C	[81]
$Na_3V_2(PO_4)_3$/C	Oxalic acid	115.1, 0.1 C	91.3%, 500, 1 C	[87]
$Na_3V_2(PO_4)_3$/N-doped carbon	Critic acid	114.2, 0.2 C	92.1%, 400, 1 C	[69]
$Na_3V_2(PO_4)_3$/N-doped carbon	Critic acid and CNTs	106.5, 0.1 C	98.9%, 2000, 20 C	[42]
$Na_3V_2(PO_4)_3$/N,S-doped carbon	Critic acid	123.19, 0.1 C	99.62%, 250, 1 C	[93]
$Na_3V_2(PO_4)_3$/N,B-doped carbon	Oxalic acid	114, 1 C	–	[89]
$Na_3V_2(PO_4)_3$/C@CNTs	Critic acid and CNT	98.7, 0.1 C	81%, 500, 2 C	[54]
$Na_3V_2(PO_4)_3$@C@CNTs	Ethylene glycol and CNT	112, 1 C	95.89%, 20,000, 200 C	[70]
$Na_3V_2(PO_4)_3$/rGO	Reduced GO	116, 1 C	90.1%, 400, 10 C	[75]
$Na_3V_2(PO_4)_3$/C-Mes	Critic acid	123.19, 0.2 C	90.48%, 5000, 20 C	[65]
$Na_3V_2(PO_4)_3$/carbon dot	Oxalic acid	112.3, 0.5 C	98.4%, 20,000, 200 C	[96]

Furthermore, it is widely proclaimed that the heteroatoms (including N, S, B, P) doped into carbon coating layer of NVP/C, taking more extrinsic defects and active sites, can profoundly improve the electronic conductivity and facilitate sodium-ion transfer compared with the bare carbon coating layer [89]. Currently, nitrogen is one of the most extensive dopants due to more active sites scattered in carbon substrate leading to outstanding electrochemical performance of carbon coating layer [69, 90, 91], and nitrogen could be randomly doped in carbon layer and the surface of NVP crystal structure (Fig. 3e) [92]. Zhou et al. [93] synthesized N/S co-doped carbon skeleton enwrapped NVP/C@N,S-x% ($x=5$, 10, 15) nanoparticles using thiourea as nitrogen and sulfur sources. The synergistic effect of N and S elements had contribution to providing abundant defects and active sites in the carbon layer which produced ample Na ion-diffusion channels and boosted ionic conductivity. Benefiting from the pyrolysis of thiourea, coral-like morphology was formed and the specific micropores architectures were constructed for NVP/C@N,S-10%, providing rich conductive networks and mitigating volume expansion to enhance its structural stability (Fig. 3f). Consequently, the optimized NVP/C@N,S-10% material realized excellent sodium storage performance, exhibiting a desirable capacity of 123.19 mAh g^{-1} at 0.1 C and an eminent discharge capacity of 90.5 mAh g^{-1} at 60 C maintained to 59.2 mAh g^{-1} after 20,000 cycles (Fig. 3g).

3.1.2 *Carbon Matrix Compositing*

Compositing NVP with carbon nanotubes (CNTs) [54, 70], reduce graphene oxide (rGO) [94], mesoporous carbon (MC) [95] or carbon dots (CDs) [96] has drawn significant attention from researchers in the field of optimizing electrode materials. These various carbon matrices are gifted with peculiar structures and high conductivity, which are beneficial to constructing high-performance NVP materials for SIBs [97]. Furthermore, the special structures of carbon matrices can effectively regulate the growth process of NVP grains and block the agglomeration of NVP particles, in favor of improving the crystallinity of NVP material and facilitating its electrochemical reactions effectively.

CNTs as a kind of one-dimensional (1D) nanomaterials not only can be characterized with efficient conductive network through entanglement and adhesion but also can avoid accumulation of active grains, which are beneficial to improving the crystalline and electrochemical properties of electrode materials [98]. As depicted in Fig. 4a [99], the CNTs as a bridge between NVP and carbon layer provided highly conductive network for high-speed charge transfer to enhance the electrical conductivity of NVP particles. Dong et al. [54] induced the CNTs to NVP system for preparing NVP/C@CNTs composites by sol–gel method, delivering a high reversible capacity of 97.7 mAh g^{-1} at 0.1 C in contrast with the only 68.7 mAh g^{-1} discharge capacity for NVP/C. As revealed in the SEM images (Fig. 4b), a distinct

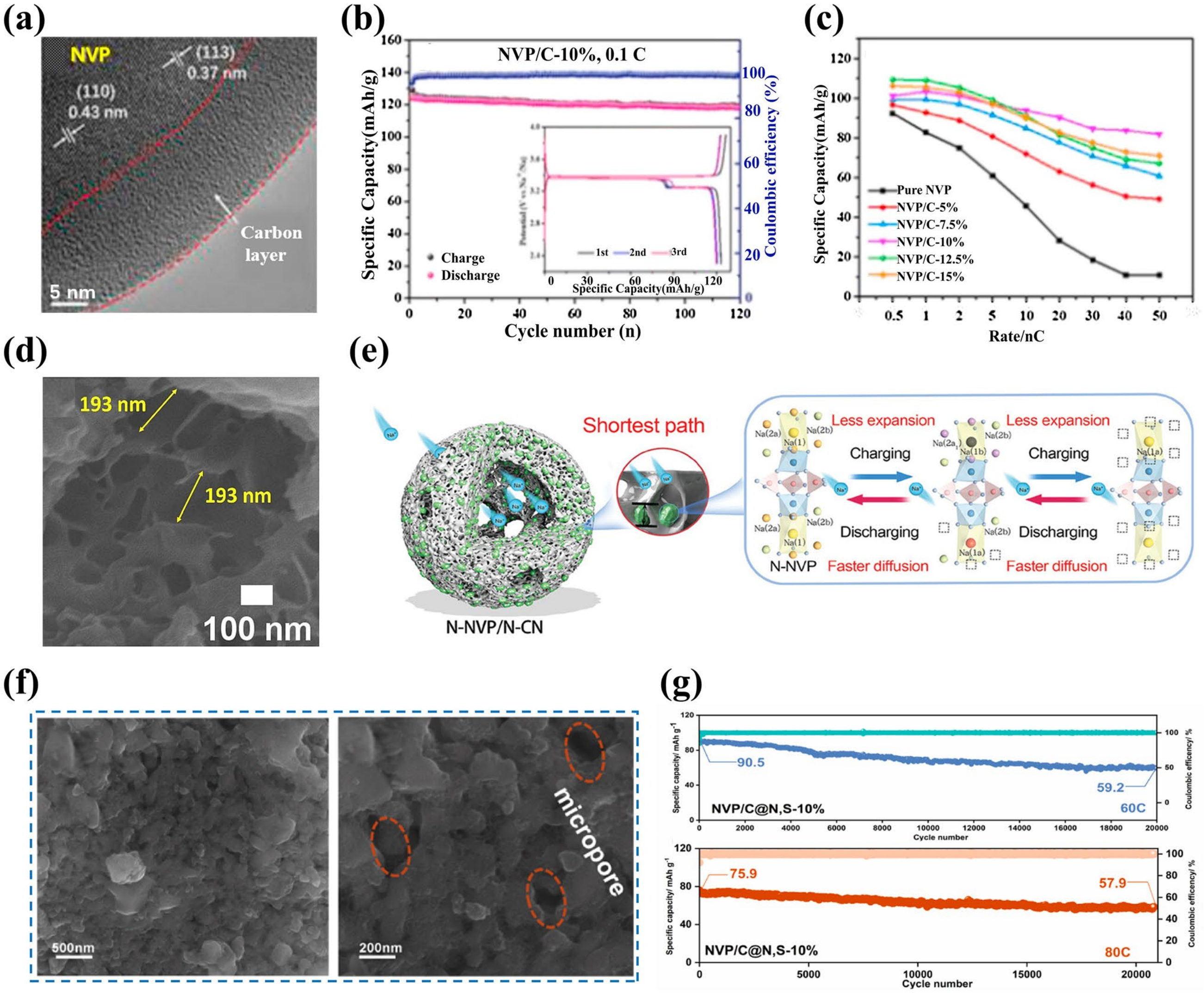

Fig. 3 **a** HRTEM (high-resolution transmission electron microscopy) image and **b** cycling performance of NVP/C-10%, **c** rate performances of NVP/C materials with different carbon contents. Reproduced with permission [81]. Copyright 2021, Elsevier. **d** SEM (scanning electron microscopy) image of NVP@C at 950 °C. Reproduced with permission [58]. Copyright 2023, Elsevier. **e** Schematic illustration of nanocage structure and surface crystal modification of N-NVP/N-CN for fast reversible three-phase reaction. Reproduced with permission [92]. Copyright 2023, Wiley. **f** SEM images and **g** cycling performance of NVP/C@N,S-10% material. Reproduced with permission. [93] Copyright 2023, Elsevier

difference in the NVP/C and NVP/C@CNTs cathodes tested at 1 C after 100 cycles was distinguished, and the distribution of NVP grains kept more homogeneous in the NVP/C@CNTs composite than in the NVP/C.

rGO with unique lamellar morphology, flexibility and high conductivity is commonly used as an ideal two-dimensional (2D) carbonaceous material introduced into electrode materials due to its constructive impacts on mechanical and electrochemical properties [94, 100, 101]. Chen et al. [102] reported that the rGO could form an efficient conductive network to accelerate the electrons migrate in the Ni-doped NVP material (Fig. 4c). Meantime, it also played a tentacle role at the edge of NVP nanoparticles to widen the specific surface area of whole system (Fig. 4d). Xu et al. [75] constructed porous NVP/rGO hollow microspheres by spray-drying approach. The rGO layer effectively elevated the electrons transfer and the unique hollow structure facilitated Na ions accessibility of electrolyte, resulting in a favorable discharge capacity of 116 mAh g^{-1} at 1 C and remarkable rate capacity of 107.5 mAh g^{-1} at 10 C (Fig. 4e).

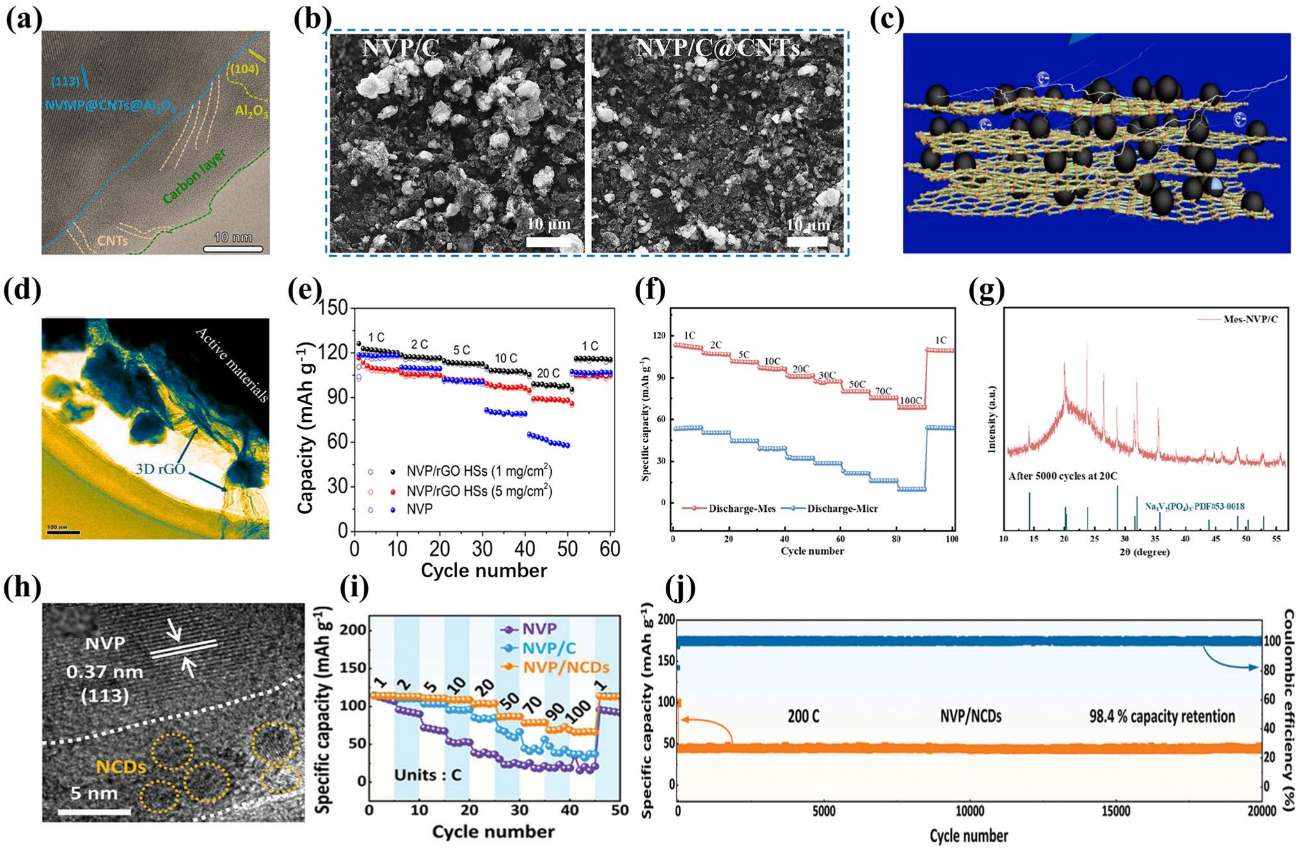

Fig. 4 **a** HRTEM image of NVMP@CNTs@1wt%Al$_2$O$_3$. Reproduced with permission. [99] Copyright 2024, Elsevier. **b** SEM images of NVP/C and NVP/C@CNTs electrodes cycled at 1 C for 100 cycles. Reproduced with permission. [54] Copyright 2021, the Author(s). **c** Schematic illustration and **d** HRTEM image of Nb$_{0.15}$-NVP/C@rGO. Reproduced with permission. [102] Copyright 2022, Elsevier. **e** Rate capability of NVP/G HSs and NVP. Reproduced with permission. [75] Copyright 2020, Elsevier. **f** Rate performance of Mes-NVP/C, **g** XRD (X-ray diffraction) pattern of Mes-NVP/C cycled over 5000 cycles at 20 C. Reproduced with permission. [65] Copyright 2024, American chemical society. **h** HRTEM image of NVP/NCDs, **i** rate performance of NVP/NCDs, **j** cycling performance of NVP/NCDs at 200 C. Reproduced with permission. [96] Copyright 2024, Wiley–VCH

MC, acted as carrier and support, can provide continuous channels and large surface area with interconnected porous structure, which ensure the fast transport of Na ions and electrons and sufficient electrolyte penetration and accommodate the volume variation during the expansion and contraction of electrode material [103, 104]. Nano-encapsulating of active materials combined with MC has been widely investigated to optimize sodium storage performance [95, 105]. Zhang et al. [65] proposed a ligand-confined growth strategy to confine the ultrasmall NVP nanoparticles in different carbon channels including microporous (Micr-NVP/C), mesoporous (Mes-NVP/C) and macroporous (Macr-NVP/C) carbon channels to seek the optimal carbon channel. The as-prepared Mes-NVP/C with sufficient ion-adsorption sites and well interconnected framework not only provided many convenient pathways for fast diffusion of Na ions and electrons but also effectively suppressed the agglomeration of NVP nanoparticles compared to the Micr-NVP/C and Macr-NVP/C cathode materials. Consequently, the Mes-NVP/C cathode achieved a high specific capacity of 70 mAh g^{-1} at 100 C (Fig. 4f), and exhibited satisfactory cyclic performance (90.48% capacity retention at 20 C after 5000 cycles). The NVP phase of Mes-NVP/C kept a good integrity after 5000 cycles (Fig. 4g), dramatically confirming the desirable ultrahigh-rate cycling stability. It was the nanoconfined NVP materials within mesoporous carbon channels that played a positive role in synchronously boosting rate capability and high-rate cycling stability.

CDs have been ingeniously adopted to integrate with electrode materials in energy conversion and storage fields on account of their fascinating physicochemical properties such as quantum tunneling effect and preeminent conductivity for elevating the electron-transfer ability [106, 107]. Pan' group [108] adopted a one-step solvothermal approach to synthesize CDs-modified NASICON-structured polyanion cathode material, where CDs were synthesized by hydrothermal method with sucrose as precursor, and revealed that CDs could be viewed as functional additive and nucleation sites to prompt morphology evolution of polyanion cathode material and harvest remarkable rate and cycling performance. Huang et al. [96] reported a facile trace carbon dot incorporation strategy to optimize the structure and sodium storage properties of NVP. The pale-yellow solid CDs were prepared from the mixing solution of tartaric acid, diethylenetriamine and ethanol with the oil bath heating. The as-developed NVP with incorporated CDs (NVP/NCDs) only contained surprisingly low carbon content of 0.76 wt%, and the trace CDs regulated the growth of NVP nanoparticles and significantly balanced the electrical conductivity and electrochemical activity of NVP. As shown in Fig. 4h, the CDs decorated with sufficient surface function groups would form a thinner and more uniform cathode/electrolyte interface (CEI) film combined with carbon coating on the surface of NVP/NCDs, which effectively boosted the interfacial charge diffusion and promoted rate capability significantly. As a result, the NVP/NCDs cathode delivered an impressive reversible capacity of 113.9 mAh g^{-1} at 1 C (Fig. 4i) and exceptional cyclability up to 20,000 cycles corresponding to the capacity retention of 98.4% (Fig. 4j). In addition, ultrafast charging performance was achieved for N/S co-doped CDs/NVP (NVP/NSC) cathode material based on an interfacial synergistic strategy [109], delivering an admirable capacity of 87.2 mAh g^{-1} at 100 C after 10,000 cycles. The assembled full cell NVP/NSC||HC (hard carbon) exhibited an excellent discharge capacity of 115.3 mAh g^{-1} at 5 C and 92.1% capacity retention after 800 cycles.

Generally, a suitable carbon coating layer can serve as armor to shelter NVP particles, which endows the interface contact between NVP and electrolyte with reduced interface impedance, while carbon coating layer has relatively low electrical conductivity in comparison to carbon matrix compositing because the carbon coating layer may hinder the migration of Na^+ ions and thus affect its electrochemical kinetics [66]. Conversely, for the carbon matrices in the NVP/C, there exists a low impact on lowering contact resistance between NVP and carbon matrix due to the uneven distribution of carbon matrix and the inhomogeneity of NVP particle sizes [43, 97]. Therefore, a synergistic effect can be achieved by combining carbon coating with carbon matrix to further improve electrical conductivity and boost interfacial kinetics for the NVP cathode material.

3.2 Foreign-Ion Doping or Substitution

The carbon coating or modification cannot effectively improve the intrinsic electronic and ionic conductivities of NVP cathode material. To introduce foreign ions into NVP material, as a mainstream strategy, plays a pivotal role to inherently reinforce the bulk-phase intrinsic electronic conductivity, narrow electron transport path and activate more active sites [92]. Generally, the foreign-ion doping or substitution mainly involves the Na, V, and PO_4^{3-} sites. To be specific, Na site can be replaced by monovalent alkali metal cations and divalent metal ions. Based on the trivalent vanadium V^{3+}, the occupation of V site can be divided into isovalent-ion and aliovalent-ion substituting. The replacement of PO_4^{3-} site can be performed by introducing monoatomic anion or multivalent anion. Additionally, synergistic effects of multiple dimensional doping combined with different sites can significantly boost the electrochemical performance and kinetic properties of NVP as well [110–113].

3.2.1 Na Site Doping

There are two kinds of chemical environments for Na ions occupying Na1 site and Na2 site, corresponding to the occupancy rate of 84.3% and 71.9%, respectively [71]. Therefore, the manipulation of Na site's coordination environment by doping metal ions is a useful strategy to elevate Na ion mobility and boost ion-transportation capability in the NASICON-type phosphate cathodes [114].

The K^+ having a larger radius (1.38 Å) and same number of electronic charges with Na^+, acted as pillar ion, can broaden Na ion-transport channels and enlarge the unit cell volume through replacing immobile Na ions, presenting a significant enhancement in rate capability and cycling stability of NASICON-type cathodes [115, 116]. The mechanism of K doping in NVP/C was elucidated through theoretical calculations by Yan's team [67], confirming that the K^+ activated the activity of Na^+ by preferentially occupying Na2 site and then Na1 site and optimized the electronic structure by reducing the bandgap of $Na_{2.9}K_{0.1}V_2(PO_4)_3$. Moreover, the introduction of K^+ could expand ion-transport channels, facilitate Na ion's transfer and weaken structural deformation during the fast deintercalation/intercalation processes of Na^+, harvesting satisfactory sodium storage performance. Shen et al. [117] reported that the K^+ was employed to dope Na site in NVP framework (Fig. 5a), which promoted Na ion migration, effectively alleviated volume variation and improved structural integrity. Consequently, the as-developed $Na_{2.95}K_{0.05}V_2(PO_4)_3$ cathode exhibited splendid sodium storage performance under all-climate (− 25–40 °C) associated with the desirable safety, delivering an initial discharge capacity of 97.8 mAh g^{-1} at 100 C in 40 °C and sustaining a capacity of 72 mAh g^{-1} at 2 C in − 25 °C (Fig. 5b, c). Subsequently, Yan's team [118] explored the effect of Li doping at Na site by synthesizing a series of $Na_{3-x}Li_xV_2(PO_4)_3/C$ ($x = 0$, 0.1, 0.2, 0.3, 0.4) cathode materials. Figure 5d displays the lattice structure of Li-doped NVP. The introduction of Li^+ ($x = 0.2$) could activate the activity of Na ions at Na2 sites efficiently and increase structural stability by inhibiting phase transition, rendering an awesome reversible capacity of 116.9 mAh g^{-1} at 0.2 C and 99.82% capacity retention after 500 cycles (Fig. 5e, f).

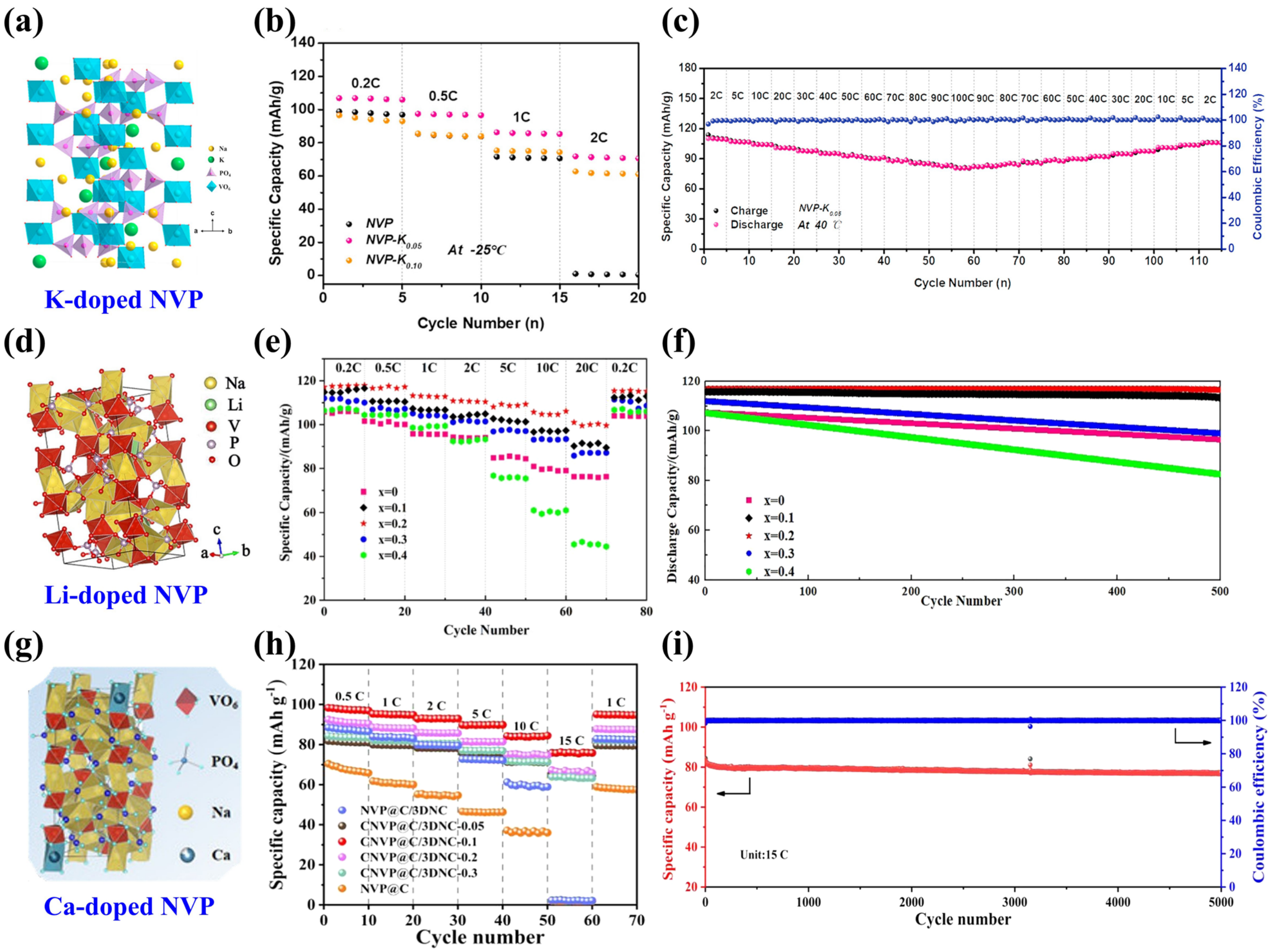

Fig. 5 **a** Schematic illustration of crystal structure of K-doped NVP, **b** rate performance of NVP, $NVP\text{-}K_{0.05}$ and $NVP\text{-}K_{0.10}$ samples at − 25 °C, **c** rate performance of $NVP\text{-}K_{0.05}$ at 40 °C. Reproduced with permission [117]. Copyright 2023, Elsevier. **d** Schematic illustration of crystal structure of $Na_{2.8}Li_{0.2}V_2(PO_4)_3$, **e** rate performance and **f** cycle performance of $Na_{3-x}Li_xV_2(PO_4)_3/C$. Reproduced with permission [118]. Copyright 2023, Elsevier. **g** Schematic illustration of crystal structure of Ca-doped NVP, **h** rate capability of NVP@C and CNVP@C/3DNC with different Ca amounts, **i** long-term cycling performance of CNVP@C/3DNC-0.1 at 15 C. Reproduced with permission [121]. Copyright 2022, American chemical society

Apart from the monovalent K and Li doping, high-valence Ca plays a favorable role to occupy part of Na site because of their similar electronegativity (Ca^{2+}: 1.16, Na^{+}: 1.024) and ionic radius (Ca^{2+}: 1.0 Å, Na^{+}: 1.02 Å), which significantly improves Na ion-diffusion kinetics and sodium storage performance of NVP material [119, 120]. Chen et al. [121] prepared $Na_{3-2x}Ca_xV_2(PO_4)_3$ with N-doped carbon nanosheet network (CNVP@C/3DNC-x, $x = 0.05$, 0.1, 0.2, 0.3) by a template-assisted sol–gel route, and the crystal structure of Ca-doped NVP is shown in Fig. 5g. The X-ray photoelectron spectroscopy (XPS) spectra showed clear signature of peaks at 347.3 and 350.9 eV corresponding to the Ca $2p_{2/3}$ and Ca $2p_{1/2}$ spin–orbit states. Meanwhile, there were two V $2p$ peaks at 517.0 and 523.7 eV corresponding to the V $2p_{2/3}$ and V $2p_{1/2}$, indicating that the Ca doping did not change the valence of vanadium and successfully occupied Na sites. Due to the beneficial effects from the regulation of Na site by Ca doping, more Na vacancies generated and thus raised intrinsic electronic conductivity and Na^{+} diffusion kinetics. The optimized CNVP@C/3DNC-0.1 released a superior specific capacity of 83.0 mAh g^{-1} at 15 C with 6.9% capacity decay after 5000 cycles, showing outstanding long-term cycling performance (Fig. 5h, i).

3.2.2 V-Site Doping or Substitution

There are mostly various V-substituted NVP cathode materials that have triggered extensive investigations since the substitution of V element holds many merits. Firstly, the replacement of V by inexpensive and nontoxic metal ions can reduce the cost of SIBs [122]. Secondly, it is a desirable thing to achieve satisfactory energy density by virtue of the multivalence states of V element (V^{3+}, V^{4+}, and V^{5+}), which can allow for the reversible multi-electron redox reactions at a high-voltage platform [123, 124]. Thirdly, various metal ions gift their own properties which are beneficial to enhancing the stability of structure, increasing reversible discharging capacity and elevating Na^{+} diffusion kinetics of NVP [125–127]. Specifically, the replacement of V in NVP can be divided into three aspects, including isovalent-ion substitution, aliovalent-ion substitution and multiple-ions substitution, as shown in Fig. 6.

3.2.2.1 Isovalent-Ion Substitution Trivalent metal ion's substitution, presenting electrical neutrality due to the equivalent valence state with V ion, can be easily achieved to optimize the structure of NVP material with fine-tunning property, which slightly impacts the overall structural integrity of NVP. The influences of isovalent-ion substitution are further discussed based on the different sizes of metal ions. For the smaller-size metal ions (Cr^{3+}, Al^{3+}, Ga^{3+}) substituting V, the stronger and shorter M–O chemical bond not only strengthens the oxygen ligand skeleton (MO_6) for the enhancement of overall structural stability but also accelerates the Na^{+} migration for faster kinetics, while the larger-size metal ions (Mn^{3+}, Fe^{3+}, Ru^{3+}, Sc^{3+}, Y^{3+}, etc.), acted as pillar ions, play a significant role in supporting the crystal framework and broadening the channels of Na^{+} diffusion, leading to higher ionic conductivity [73, 128–131].

One of the popular isovalent-ion substitutions in NVP cathode material is Cr^{3+} doping, in which Cr^{3+} possesses a slightly smaller radius of 0.755 Å than V^{3+} (0.78 Å), and it has been corroborated extensively for the great improvement of electrochemical performance [132–135]. Goodenough et al. [132] reported a series of Cr-doped $Na_3V_{2-x}Cr_x(PO_4)_3$ ($x = 0$, 0.2, 0.5, 1 and 2) cathode materials. All samples were well consistent with the rhombohedral NASICON structure in space group R $\overline{3}$ c and no apparent additional diffraction peaks appeared, suggesting a long-range order between the V and Cr in the NVP. Due to the smaller size of Cr, the lattice volume of Cr-doped NVP revealed a decreasing phenomenon (Fig. 7a). It is noteworthy that the $Na_3V_{1.5}Cr_{0.5}(PO_4)_3$ exhibited the most stable cycling performance in all samples. Moreover, as shown in Fig. 7b, the $Na_3V_{1.5}Cr_{0.5}(PO_4)_3$ cathode enabled three-electron redox reactions with V^{2+}/V^{3+} (1.6 V), V^{3+}/V^{4+} (3.6 V) and V^{4+}/V^{5+} (4.1 V) redox couples fully activated within a wide voltage window of 1.0–4.4 V. Another meaningful observation about $Na_3V_{1.5}Cr_{0.5}(PO_4)_3$ was the occurrence of a peculiar solid-solution reaction accompanied by the successful activation of V^{4+}/V^{5+}, which played a critical role in the stabilization of phase structural evolution during the successive sodiation/de-sodiation processes. Consequently, the $Na_3V_{1.5}Cr_{0.5}(PO_4)_3$ manifested a favorable discharge capacity of 150 mAh g^{-1} at 30 mA g^{-1} (Fig. 7c). Furthermore, Chen et al. [124] investigated in depth what a role the Cr behaved in a high redox potential with multielectron reactions and clarified intrinsic

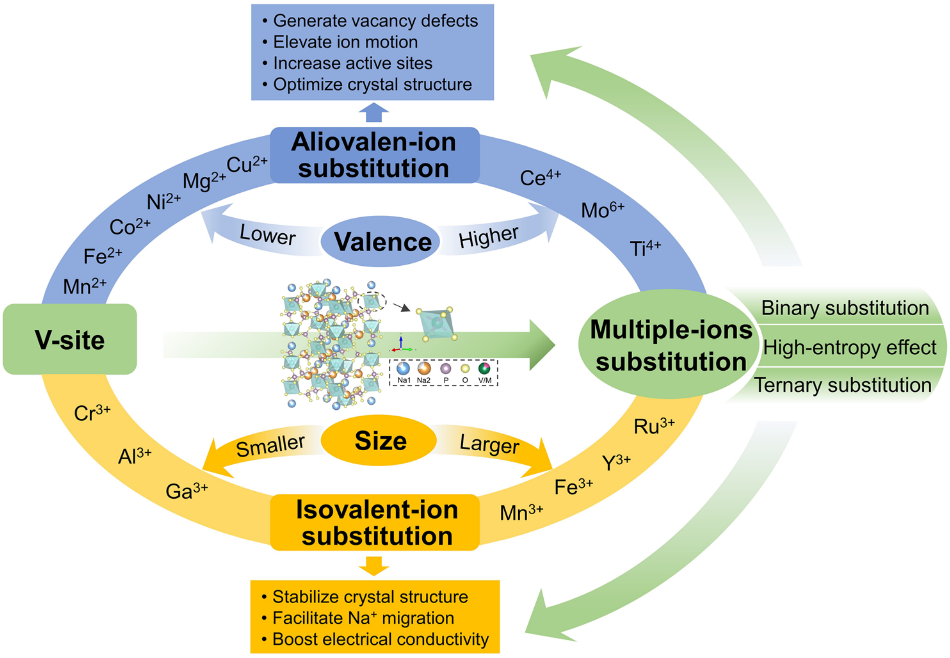

Fig. 6 Outline of foreign-ion doping or substitution in V site of NVP material and their advantages

reasons for how Cr activated the V^{4+}/V^{5+} redox couple. They verified that the $Na_3V_{1.5}Cr_{0.5}(PO_4)_3$ involved in a main sodium storage process of solid-solution reaction at high-voltage platforms of 3.4 and 4.1 V through a series of advanced characterization techniques. As displayed in the operando synchrotron-based XRD (Fig. 7d), all of the observed peaks showed well reversible change without asymmetric shifts attributed to the well-maintained polyanionic structure during the Na ion's insertion and extraction processes, indicating that the Cr doping had a positive effect on inhibiting crystal distortion and keeping long-term cyclic stability of NVP cathode material. Besides, with the combination of DFT calculations with electron paramagnetic resonance (EPR) spectroscopy, it was unveiled that the Cr-doped NVP had unpaired electron of Cr in the 3*d* orbital ($[Ar]3d^54s^1$) and a narrower forbidden bandgap than undoped NVP (V ($[Ar]3d^34s^2$)), which, as the intrinsic reasons, would make contribution to triggering the V^{4+}/V^{5+} redox couple and increasing energy density at a high operating voltage. Later, Zhang et al. [134] designed a rGO-supported $Na_3V_{1.5}Cr_{0.5}(PO_4)_3$ (VC/C-G) cathode material. Benefiting from the complete activation of multielectron reactions from V^{2+} to V^{5+}, the as-designed VC/C-G revealed ultra-stable sodium storage performance, achieving an appreciable energy density of approximately 470 Wh kg^{-1} with a reversible capacity of 176 mAh g^{-1} at 0.2 C (Fig. 7e). Mai' group [136] reported another $Na_3Cr_{4/3}V_{3/2}(PO_4)_3$@C (NVCP@C) cathode material, and they comprehensively clarified that there were two reversible structural evolutions corresponding to solid-solution reaction and two-phase reaction during the charge and discharge processes. It was satisfactory that the NVCP@C exhibited excellent electrochemical performance, yielding an ultrahigh initial discharge capacity of 175 mAh g^{-1} at 100 mA g^{-1} accompanying about 3.1 Na^+ ions insertion and durable long-term cycling performance with 86% capacity retention at 5000 mA g^{-1} after 2000 cycles (Fig. 7f and g).

Al is an inactive element introduced into NVP material, and it has been demonstrated that Al doping not only particularly stabilizes the phase structure but also impedes the occurrence possibility of side reactions during the charge and discharge processes [137–139]. Masquelier [140] firstly proposed the substitution of V by Al in the $Na_3V_{1.5}Al_{0.5}(PO_4)_3$, which realized a comparable increasement of the theoretical energy density (425 Wh kg^{-1}) than undoped NVP (396.3 Wh kg^{-1}) [141], resulting from the accessibility of higher-voltage V^{4+}/V^{5+} redox reaction and

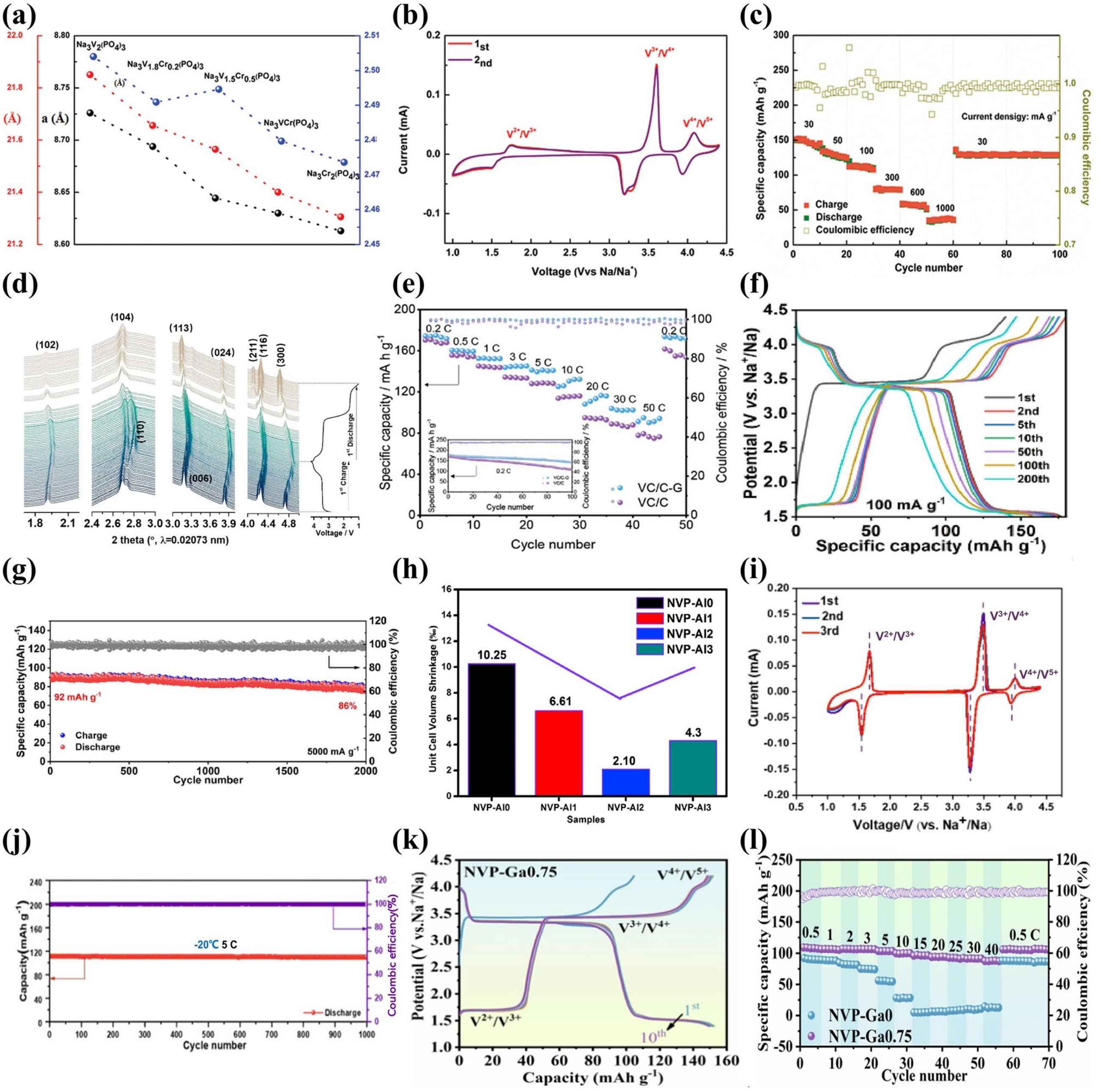

Fig. 7 **a** Variations of crystallographic parameters (lattice parameters of *a*, *c* and the ratio of *c*/*a*) for $Na_3V_{2-x}Cr_x(PO_4)_3$ ($0 \le x \le 2$), **b** CV curves of $Na_3V_{1.5}Cr_{0.5}(PO_4)_3$ at 0.5 mV s^{-1}, **c** rate capability of $Na_3V_{1.5}Cr_{0.5}(PO_4)_3$. Reproduced with permission [132]. Copyright 2020, Wiley-VCH. **d** Operando XRD patterns of $Na_3V_{1.5}Cr_{0.5}(PO_4)_3$ material at different charge/discharge states. Reproduced with permission [124]. Copyright 2021, American Chemical Society. **e** Rate properties of VC/C-G and VC/C. Reproduced with permission [134]. Copyright 2022, Wiley-VCH. **f** Charge/discharge profiles and **g** cycling performance of NVCP@C. Reproduced with permission [136]. Copyright 2023, Wiley-VCH. **h** Unit cell volume shrinkage of $Na_3V_{2\text{-}x}Al_x(PO_4)_3/C$ before and after 50 cycles. Reproduced with permission [47]. Copyright 2017, Elsevier. **i** CV profiles at 0.2 mV s^{-1} and **j** cycling performance of $Na_3V_{1.5}Al_{0.5}(PO_4)_3$. Reproduced with permission [142]. Copyright 2022, Elsevier. **k** Charge/discharge curves of NVP-Ga0.75, **l** rate performance within 2.2–4.2 V of NVP-Ga0 and NVP-Ga0.75. Reproduced with permission [61]. Copyright 2023, Elsevier

lighter weight of aluminum. Chen et al. [47] reported that Al^{3+} partial substitution in V site would provide more volume of interstitial gaps to enable more Na ions migrate due to its smaller ionic radius than V^{3+} (Al^{3+}: 0.0535 nm vs. V^{3+}: 0.064 nm), as well as significantly strengthen the structural robustness of NVP. It was clear that the cell volume generated distinct contraction after 50 cycles at high discharge rate in different samples. However, the $Na_3V_{1.98}Al_{0.02}(PO_4)_3$/C only had a marginal volume change (2.10%), compared with the undoped NVP (10.25%) (Fig. 7h). To improve the operating voltage, Jin's team [142] investigated the electrochemical reaction mechanism of $Na_3V_{1.5}Al_{0.5}(PO_4)_3$ cathode with reversible three-electron redox reactions in the potential range of 1.0–4.4 V. A new redox couple located at around 4.0 V was distinctly witnessed, which was attributed to the initiation of reversible V^{4+}/V^{5+} redox reaction (Fig. 7i), resulting in an impressive increase in the capacity (165 mAh g^{-1} at 0.1 C). Moreover, the framework of AlO_6 octahedron in $Na_3V_{1.5}Al_{0.5}(PO_4)_3$ had a more negative average charge of O atom than VO_6 in $Na_3V_2(PO_4)_3$, indicating that the V^{3+} substitution by Al^{3+} made a positive effect on enhancing the oxygen ligand skeleton and elevating the overall structural stability at high potential. As a result, the $Na_3V_{1.5}Al_{0.5}(PO_4)_3$ achieved a desirable low-temperature (− 20 °C) cycling performance (98.9% capacity retention after 1000 cycles at 5 C) (Fig. 7j).

Similar to Al element, Ga is another inactive element with ionic radius of 0.062 nm, which can substitute V to obtain improved rate capability and cycling performance [130, 139]. Chen et al. [61] reported that the introduction of Ga^{3+} could successfully activate the V^{4+}/V^{5+} redox couple of $Na_3V_{2-x}Ga_x(PO_4)_3$ (NVP-Gax, $x = 0$, 0.5, 0.75, 1) cathodes within a voltage window of 1.4–4.2 V, containing single-phase and bi-phase electrochemical reactions. A series of spectroscopic and electrochemical tests verified that the modified sample with $x = 0.75$ exhibited a superior structural stability and Ga^{3+} did not participate in the electrochemical reactions. The NVP-Ga0.75 presented a remarkable discharge capacity of 152.3 mAh g^{-1} at 1 C with a favorable energy density of 497.6 Wh kg^{-1} (Fig. 7k). Meanwhile, in 2.2–4.2 V, the NVP-Ga0.75 exhibited excellent rate capability with a high discharge capacity of 105 mAh g^{-1} at 1 C (Fig. 7l).

Among some larger-size metal ions, Fe^{3+} and Mn^{3+} dopants are capable of holding active electrochemical activities, significantly improving the capacity of NVP cathode materials and their doping is beneficial to satisfying the requirement of sustainable development and large-scale applications by virtue of their low-cost and eco-friendly advantages. Additionally, the doping of Fe^{3+} and Mn^{3+} into V site accompanies more than two-electron reactions during the electrochemical reaction process, which availably enhances the energy density of NVP cathodes. Thus, Fe^{3+} and Mn^{3+} doped NVP cathodes have been popularly investigated [129, 143, 144]. Chen et al. [129] performed a family of Mn^{3+} doped $Na_3V_{2-x}Mn_x(PO_4)_3$ ($x = 0$, 0.1, 0.3, 0.5, 0.7) (NVP-Mn(x)) cathodes by a simple solid-state reaction, and demonstrated that Mn^{3+} could activate multielectron reactions by successive conversions of V^{2+} to V^{5+} in a wide voltage window of 1.4–4.0 V. The crystal structure of NVP-Mn(0.5) is simulated in Fig. 8a. Benefiting from the relatively larger radius of Mn^{3+} (0.785 Å) compared to V^{3+} (0.78 Å), the NVP-Mn(x) cell took lattice expansion, which facilitated Na^+ migration and enhanced ionic conductivity. Similar to the oxygen ligand surroundings of $Na_3V_{1.5}Al_{0.5}(PO_4)_3$, the MnO_6 of NVP-Mn(0.5) possessed a more negative average charge of O (− 1.51249 e) than the VO_6 of undoped NVP (− 1.47935 e), significantly strengthening structural stability. In addition, in the hybridized Mn *3d* orbitals of NVP-Mn(0.5), the electron structure was optimized due to the reduced bandgap and thus improved the electronic conductivity. As illustrated in Fig. 8b, a new redox couple of Mn^{2+}/Mn^{3+} was discerned when being discharged to 1.4 V and finally Mn^{2+} disappeared at 3.7 V, indicating Mn^{2+}/Mn^{3+} couple participating in the electrochemical reactions. Coupled with the additional charge platforms located around 3.9 V (V^{4+}/V^{5+}) and 1.7 V (V^{2+}/V^{3+}) (Fig. 8c), the NVP-Mn(0.5) displayed an appealing reversible capacity of 170.9 mAh g^{-1} at 0.5 C. However, due to the presence of serious Jahn–Teller effect of MnO_6, it is easy for Mn^{3+} dissolving in electrolyte, posing a dilemma for enhancing cycling stability [140].

For the Fe^{3+} doping, Lin et al. [143] developed $Na_3V_{2-x}Fe_x(PO_4)_3$/C ($x = 0$, 0.1, 0.3, 0.5, 0.7) (NVP-Fe(x)) cathode materials via a solid-state reaction. Figure 8d, e revealed the crystal structure and Raman spectra of NVP-Fe(x), indicating that the larger radius of Fe^{3+} had a little impact on the NVP lattice and the NVP-Fe(0.5) carried the highest degree of order and thus would obtain the best electrochemical performance. The NVP-Fe(0.5) cathode material exhibited an exceptional initial capacity of 166.4 mAh g^{-1} at 1 C coinciding with a high energy density of 417.3 Wh kg^{-1}

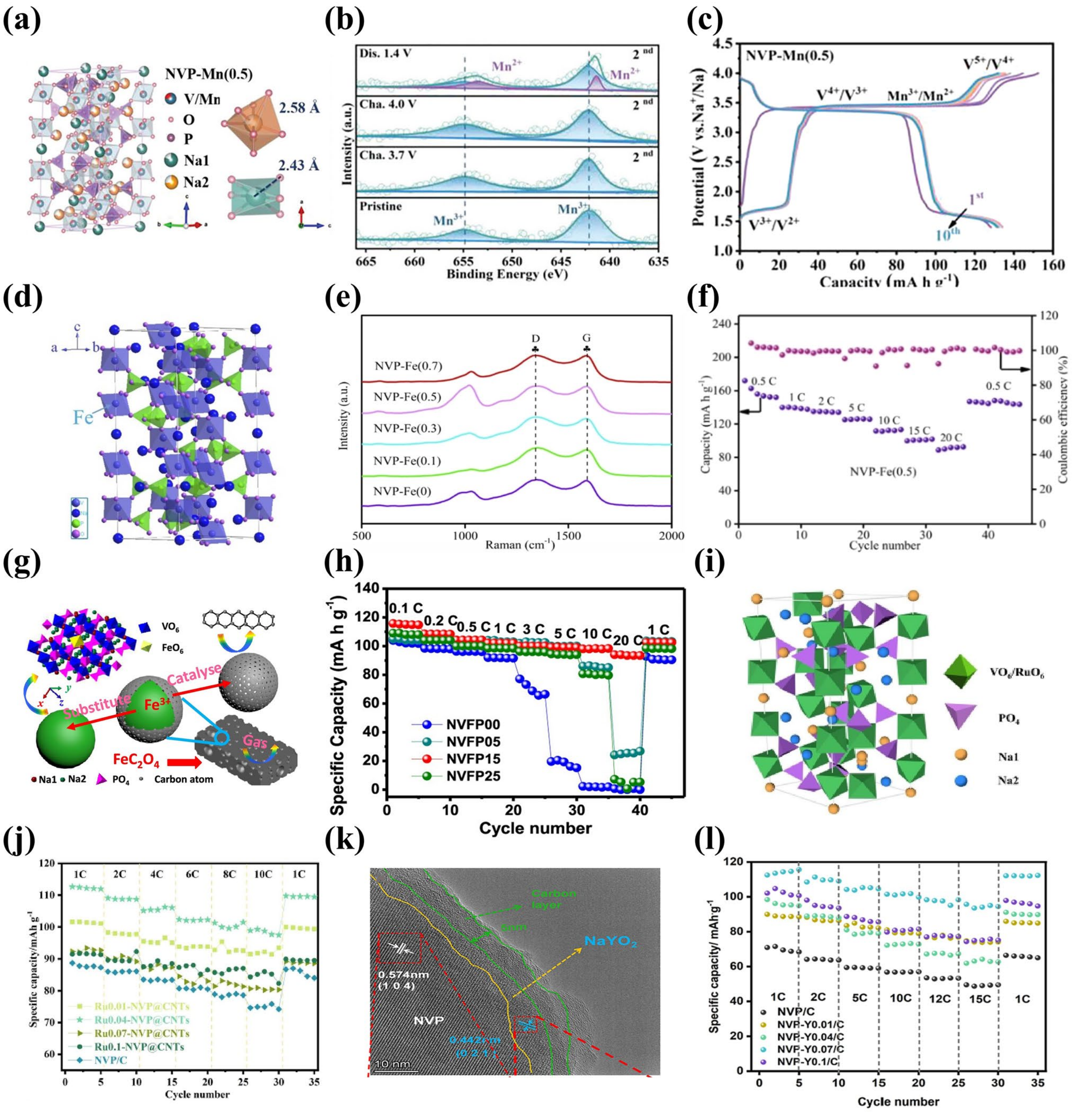

Fig. 8 **a** Crystal structure diagram of NVP-Mn(0.5), **b** XPS spectra of Mn 2*p* of NVP-Mn(0.5), **c** charge/discharge curves of NVP-Mn(0.5). Reproduced with permission [129]. Copyright 2023, Wiley-VCH. **d** Crystal structure diagram of Fe^{3+}-doped NVP, **e** Raman spectra of NVP-Fe(x), **f** rate performance of NVP-Fe(0.5). Reproduced with permission [143]. Copyright 2023, Elsevier. **g** Schematic illustration of Fe^{3+} ion into the V sites in NVP, **h** rate capability of different NVFP samples. Reproduced with permission [131]. Copyright 2019, American Chemical Society. **i** Crystal structure model of Ru^{3+} doped NVP, **j** rate capability of different Ru-doped NVP samples. Reproduced with permission [73]. Copyright 2024, Elsevier. **k** HRTEM image of NVP-Y0.07/C material, **l** rate capability of $Na_3V_{2-x}Y_x(PO_4)_3$/C. Reproduced with permission [145]. Copyright 2023, Elsevier

and superior rate performance with 84.6 mAh g^{-1} at 20 C (Fig. 8f), which were attributed to the successful activation of V^{4+}/V^{5+} redox couple by Fe^{3+} at a high working voltage to achieve three-electrons reaction. Similarly, Tong' group [62] synthesized $Na_3Fe_{0.8}V_{1.2}(PO_4)_3/C$ (NFVP/C) cathode material with an optimal crystal structure by a sol–gel method. With the help of DFT calculations, the NVFP/C showed a suitable ion-migration route with low diffusion barrier. The path 1 (P1) revealed smaller energy barrier of 0.14 eV than the path 2 (P2) (0.30 eV), which remarkably improved Na$^+$ diffusion kinetics. Two pairs of redox peaks were observed at 3.4 and 4.0 V, which was in good agreement with two stable platforms in the charge and discharge curves, presenting a high reversible capacity of 115.2 mAh g^{-1} at 0.5 C. Besides, Liu et al. [131] reported that Fe^{3+} could serve as a catalyst to not only effectively modulate carbon layer graphitization and bulk phase for improving electronic conductivity but also accelerate the infiltration of electrolyte for fast diffusion of Na$^+$ due to the decomposition of organic iron forming open porous structure (Fig. 8g). Consequently, the optimized $Na_3V_{1.85}Fe_{0.15}(PO_4)_3$@C (NVFP) cathode material obtained outstanding rate capability with a discharge capacity of 94.45 mAh g^{-1} at 20 C (Fig. 8h).

Recently, the replacement of other isovalent ions with larger radius than V^{3+} was also explored. Shi et al. [73] investigated the modified mechanism of Ru doping in V site and synthesized a Ru^{3+}-doped and CNT-enwrapped $Na_3V_{1.96}Ru_{0.04}(PO_4)_3$/C@CNT material (Fig. 8i). On account of the relatively larger ionic radius of Ru^{3+} than V^{3+} (Ru^{3+}: 0.68 Å vs V^{3+}: 0.64 Å), the modified material broadened and further stabilized the Na ion-migration channels accompanied by higher ionic conductivity and more stable structure with reversibility during the processes of Na$^+$ extraction and insertion. The $Na_3V_{1.96}Ru_{0.04}(PO_4)_3$/C@CNT had the low value of volume contraction rate that changed less than 3% in the discharge process, further confirming the extraordinary structural stability after the introduction of Ru ion. Consequently, the $Na_3V_{1.96}Ru_{0.04}(PO_4)_3$/C@CNT yielded an excellent rate capability with a high capacity of 99.97 mAh g^{-1} at 10 C (Fig. 8j) and superior cycling stability, and submitted an initial capacity of 82.3 mAh g^{-1} and a sustained capacity of 71.3 mAh g^{-1} at 80 C after 14,800 cycles. Subsequently, Shi et al. [88] also proposed that the larger radius Bi^{3+} (1.08 Å) doped into V site would effectively widen ion-transmission channels and promote the Na$^+$ diffusion kinetics of NVP. The synthesized $Na_3V_{1.97}Bi_{0.03}(PO_4)_3$/C@CNTs cathode revealed superior rate performance, submitting 84.34 mAh g^{-1} capacity at 80 C with 86.96% capacity retention after 6000 cycles. Moreover, Chen et al. [145] firstly reported Y^{3+} doping and successfully obtained $Na_3V_{2\text{-}x}Y_x(PO_4)_3$ ($_X$ = 0.01, 0.04, 0.07, 0.1) (NVP-Y$_X$) materials. The Y^{3+} possessed a distinctly larger radius of 0.9 Å than V^{3+} (0.64 Å), greatly expanded the Na ion-diffusion pathway and narrowed the crystal vibration, which bolstered Na ion-migration rate and reinforced the crystal structural stability. Notably, a new conductive phase of $NaYO_2$, with appealing electric conductivity, emerged between the active material and carbon layer (Fig. 8k), compellingly elevating the ionic conductivity. Consequently, the Na ion-diffusion coefficient of NVP-Y$_{0.07}$ approximately increased one order of magnitude than that of NVP/C. The NVP-Y$_{0.07}$ achieved a high discharge capacity of 125.2 mAh g^{-1} at 0.1 C and sustained 100.4 mAh g^{-1} capacity at 1 C after 300 cycles (Fig. 8l).

3.2.2.2 Aliovalent-Ion Substitution Although the isovalent-ion doping at V site has a minimal impact on the structural integrity of NVP, the electronic structure of NVP is hardly to further regulation. Thus, the doping of aliovalent ion is popularly appealing, consisting of low-valent ion doping and high-valent ion doping, which have a profound influence on the electrochemical performance of NVP materials. Specifically, the introduction of low-valent ion, thanks to the charge compensation mechanism, will generate favorable hole carriers (or electronic defects) and thus enhance the electronic conductivity, while the high-valent ion will provide additional free electrons and boost electron-transmission ability.

Among some divalent metal ions, Mn^{2+} and Fe^{2+}, with multielectron transfer potential, have been intensely studied because of their more fruitful properties, and the Mn^{2+} and Fe^{2+} doping not only widen the voltage window but also effectively enhance the sodium storage performance of NVP cathodes [140, 146–148]. The study demonstrated that the existence of Mn^{2+} in $Na_3V_{2\text{-}x}Mn_x(PO_4)_3$ ($x = 0, 0.1, 0.2, 0.3$) materials could stimulate more V^{4+} due to the charge compensation, thereby stabilize the crystal structure and enhance the electronic conductivity. As shown in Fig. 9a–c, the optimal $Na_3V_{1.8}Mn_{0.2}(PO_4)_3/C$ exhibited the largest Na$^+$ diffusion coefficient, superior rate performance with 106.8 mAh g^{-1} at 1 C and impressive cycling stability with 82% capacity retention at 30 C after 10,000 cycles [149]. In addition, Na-rich $Na_{3+x}Mn_xV_{2\text{-}x}(PO_4)_3$ cathode based on

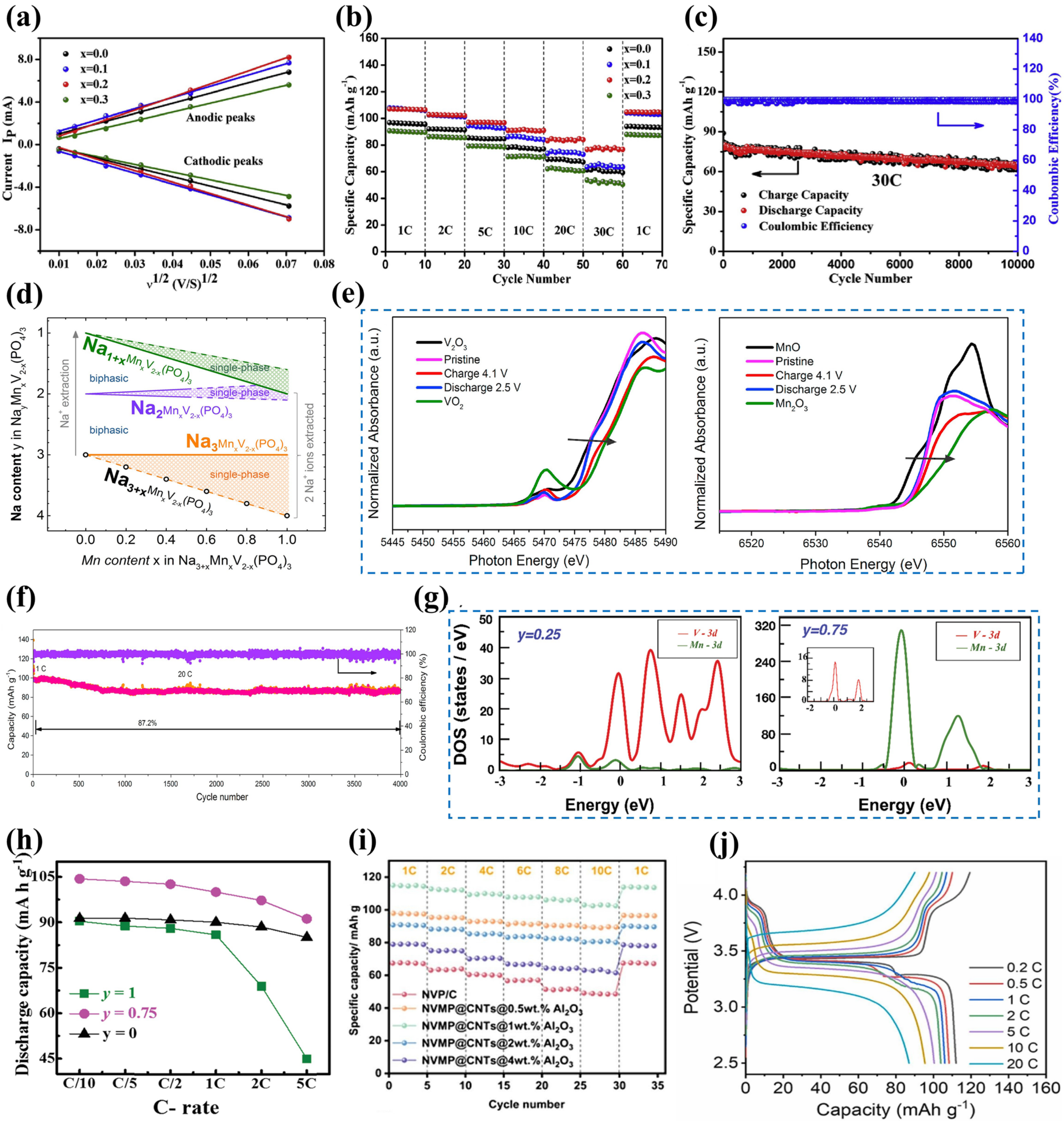

Fig. 9 **a** Corresponding relationship between $\nu^{1/2}$ and peak current, **b** rate capability of $Na_3V_{2\text{-}x}Mn_x(PO_4)_3$/C cathodes, **c** cycling performance of $Na_3V_{1.8}Mn_{0.2}(PO_4)_3$/C at 30 C. Reproduced with permission [149]. Copyright 2018, Elsevier. **d** Schematic illustration of Na^+ deintercalation regimes from $Na_{3+x}Mn_xV_{2\text{-}x}(PO_4)_3$ during Na^+ extraction. Reproduced with permission [150]. Copyright 2020, Elsevier. **e** XANES spectra of (Left)V K-edge and (Right) Mn K-edge of the NVMP/C electrode collected at different charge and discharge states, **f** cyclic stability at 20 C of NVMP/C. Reproduced with permission [152]. Copyright 2018, Elsevier. **g** Projected density of states of $Na_{3+y}V_{2-y}Mn_y(PO_4)_3$ cathodes, **h** rate capability of $Na_{3+y}V_{2-y}Mn_y(PO_4)_3$ cathodes. Reproduced with permission [151]. Copyright 2019, Wiley-VCH. **i** Rate capability of different NVMP samples. Reproduced with permission [99]. Copyright 2024, Elsevier. **j** Charge–discharge curves at different rates of NMVP/C@GO. Reproduced with permission [147]. Copyright 2023, Elsevier

Mn^{2+} substitution and extra Na^+ manifested great advantages in terms of its desirable electrochemical properties and beneficial phase transformation behavior [150–152]. Zakharkin et al. [150] synthesized a succession of $Na_{3+x}Mn_xV_{2-x}(PO_4)_3$ ($0 \leq x \leq 1$) cathode materials, and all Mn-substituted samples exhibited a high-voltage platform at approximately 3.9 V, resulting in that the energy density could be elevated about 8%-10% when $x \geq 0.4$ compared with undoped NVP material. As depicted in Fig. 9d, increasing Mn content had a positive impact on the enlargement of a beneficial solid-solution domain linking with sodiated, intermediate and de-sodiated phases. The highly reversible solid-solution phase change in $Na_{3.5}Mn_{0.5}V_{1.5}(PO_4)_3$ (NVMP) was validated [152]. Through the ex situ X-ray absorption near-edge structure spectra (ex situ XANES) and XPS, prominently reversible V^{3+}/V^{4+} and Mn^{3+}/Mn^{4+} redox couples during the charge and discharge processes were observed (Fig. 9e). More impressively, the NVMP delivered intriguing rate capability with 92.7 mAh g^{-1} at 60 C and exceptional capacity retention of 87.2% after 4000 cycles at 20 C (Fig. 9f). Besides, Ghosh et al. [151] comprehensively investigated the Na-rich $Na_{3+y}V_{2-y}Mn_y(PO_4)_3$ ($0 \leq y \leq 1$) cathode materials and elucidated the influence of different Mn^{2+} contents on the crystal structure and electrochemical performance. A phase miscibility gap was witnessed at $y = 0.5$, representing two solid-solution regions related to low and high Mn contents. According to the analysis of projected density of states (pDOS) in Fig. 9g, the electronic densities of Mn 3*d* and V 3*d* orbitals in the $Na_{3.25}V_{1.75}Mn_{0.25}(PO_4)_3$ and $Na_{3.75}V_{1.25}Mn_{0.75}(PO_4)_3$ were distinctly different. The $Na_{3.25}V_{1.75}Mn_{0.25}(PO_4)_3$ exhibited a negligible Mn 3*d* electronic density, while the $Na_{3.75}V_{1.25}Mn_{0.75}(PO_4)_3$ was adverse, suggesting that Mn^{3+}/Mn^{2+} redox couple was absent and presented in the former and later materials, respectively. Furthermore, Mn element would make more contribution than V element on account of the modulation of Mn redox couples, generating a greater number of valence electrons. The $Na_{3.75}V_{1.25}Mn_{0.75}(PO_4)_3$ cathode revealed high reversible capacities of 100 and 89 mAh g^{-1} at 1 and 5 C, respectively (Fig. 9h). To further ameliorate the poor electronic conductivity of Mn-substituted NVP cathodes, Qian et al. [99] introduced 1 wt% Al_2O_3 coating and CNTs in the $Na_3V_{5.92/3}Mn_{0.04}(PO_4)_3$ material (NVMP@CNT@1wt%Al_2O_3) to curb the dissolution of Mn^{2+} in electrolyte and bolster the electrical conductivity and structural integrity. By the virtue of the effect of Al_2O_3 coating and CNTs, the NVMP@CNT@1wt%Al_2O_3 cathode performed stable rate capability with 115, 112.8, 110, 107.9, 106.5, 103.0 and 114.09 mAh g^{-1} discharge capacity at 1, 2, 4, 5, 8, 10 and 1 C, respectively (Fig. 9i), and remarkable long-term cycling stability with 84.87% capacity retention after 6000 cycles. Moreover, Li et al. [147] reported a dual carbon-coated $Na_{3.5}Mn_{0.5}V_{1.5}(PO_4)_3$ (NMVP/C@GO) cathode material via a spray-drying route. Thanks to the positive impacts of Mn^{2+} doping and carbon conductive network, the NMVP/C@GO presented a favorable reversible capacity of 112 mAh g^{-1} at 2 C and excellent rate capability with 88 mAh g^{-1} discharge capacity at 20 C (Fig. 9j).

For Fe^{2+} doping, Na-rich $Na_4FeV(PO_4)_3$ cathode material has been widely explored, and the presence of mixed valence of Fe^{2+} and V^{3+} and multielectron redox reactions are contributive to increase meaningful capacity and energy density [153–157]. Masquelier et al. [156] investigated the crystal structure and local chemical environments of $Na_4FeV(PO_4)_3$ cathode material obtained from the electrochemical sodiation of $Na_3FeV(PO_4)_3$ material. Through a series of advanced measurements, it was confirmed that Na1 and Na2 sites were almost fully occupied in the $Na_4FeV(PO_4)_3$ lattice (Fig. 10a). There remained 2.76 Na^+ per formula unit extracted in the voltage region of 1.3–4.3 V, which was attributed to the successful activation of Fe^{2+}/Fe^{3+}, V^{3+}/V^{4+} and V^{4+}/V^{5+} redox couples. The activation of V^{4+}/V^{5+} usually had irreversible electrochemical behavior and thus limited the further enhancement of capacity. Subsequently, Masquelier et al. [154] thoroughly investigated the irreversible Na^+ de/intercalation process in $Na_4FeV(PO_4)_3$ cathode material through local and bulk perspectives. As displayed in Fig. 10b, during the charge process, there were three potential regions located at around 2.52, 3.45 and 3.99 V relating to the Fe^{2+}/Fe^{3+}, V^{3+}/V^{4+} and $V^{4+}/^{5+}$ redox couples, whereas during the discharge process, only two main regions were observed at about 3.44 and 2.48 V, indicating an asymmetric extraction/insertion behavior of Na^+ at a high potential in the $Na_4FeV(PO_4)_3$ material. The activation of V^{4+}/V^{5+} caused shorter V–O band in a distorted Fe and V local environment, further revealing the asymmetric sodium storage mechanism of $Na_4FeV(PO_4)_3$ material. Moreover, Xu et al. [158] demonstrated that the reversible activation of V^{4+}/V^{5+} mainly relied on the relative contents of Na1 and Na2 in the Fe^{2+}-doped NVP lattice, and enough Na2 content effectively ensured the activation of V^{4+}/V^{5+}. They prepared Na-rich $Na_{3.4}V_{1.6}Fe_{0.4}(PO_4)_3$ cathode material

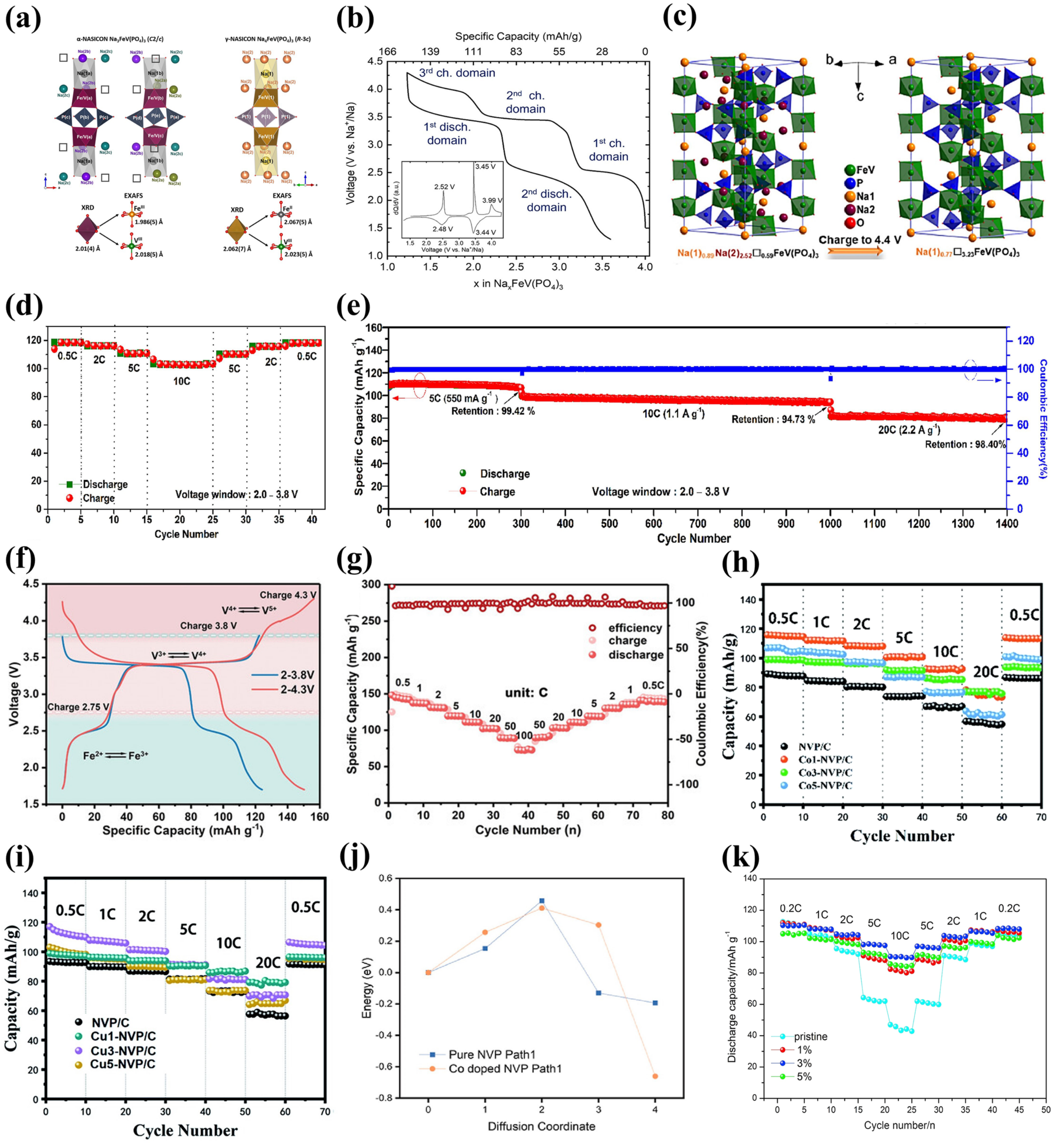

Fig. 10 **a** Schematic representations of Na$^+$ distributions in Na$_3$FeV(PO$_4$)$_3$ and Na$_4$FeV(PO$_4$)$_3$. Reproduced with permission [156]. Copyright 2021, American Chemical Society. **b** Charge and discharge curves for pre-sodiated Na$_4$FeV(PO$_4$)$_3$ electrode. Reproduced with permission [154]. Copyright 2022, American Chemical Society. **c** Polyhedral representation of NFVP unit cell, **d** rate performance of NFVP electrode, **e** Cycling performance of NFVP at 5, 10 and 20 C. Reproduced with permission [159]. Copyright 2020, Elsevier. **f** Charge–discharge profiles at 0.5 C of NVFP in different voltage windows of 1.7–3.8 and 1.7–4.3 V, **g** rate capability of NVFP in 1.7–4.3 V. Reproduced with permission. [160] Copyright 2023, Wiley-VCH. Rate performance of **h** Na$_{3+x}$V$_{2-x}$Co$_x$(PO$_4$)$_3$/C, **i** Na$_{3+x}$V$_{2-x}$Cu$_x$(PO$_4$)$_3$/C. Reproduced with permission [161]. Copyright 2021, Royal Society of Chemistry. **j** Energy barriers for NVP and Co-NVP along the diffusion pathway. Reproduced with permission [162]. Copyright 2023, Elsevier. **k** Rate performance of Na$_3$V$_{2-x}$Ni$_x$(PO$_4$)$_3$/C ($x=0$, 0.01, 0.03 and 0.05). Reproduced with permission [165]. Copyright 2017, Elsevier

which achieved an extraordinary reversible capacity of 133 mAh g^{-1} in a voltage domain of 2.0–4.1 V, resulting from the successive redox reactions of Fe^{2+}/Fe^{3+} and V^{3+}/V^{4+}/V^{5+}. Furthermore, the as-developed $Na_{3.41}£_{0.59}FeV(PO_4)_3$ (NVFP) sodium-deficient material (Fig. 10c) exhibited an astonishing reversible capacity of 170 mAh g^{-1} at 0.5 C in a wide voltage window of 1.5–4.4 V, showing three pairs of redox peaks located at about 2.55, 3.46 and 4 V coinciding with the Fe^{2+}/Fe^{3+}, V^{3+}/V^{4+} and V^{4+}/V^{5+} redox couples, respectively [159]. Together, in a voltage region of 2.0–3.8 V, the NVFP also exhibited excellent rate capability with a discharge capacity of 119 mAh g^{-1} at 0.5 C and extraordinary long cycling life (Fig. 10d, e). It was the admirable electrochemical performance that came from the slight volume change of 2.36% during the successive charging and discharging processes with a solid-solution reaction mechanism. Therefore, increasing output voltage by introducing additional Fe^{2+}/Fe^{3+} redox couple and activating high-voltage V^{4+}/V^{5+} redox couple could be a significant strategy to harvest satisfactory sodium storage performance. Zhou et al. [160] designed $Na_{3.5}V_{1.5}Fe_{0.5}(PO_4)_3$ (NVFP) cathodes by introducing Fe^{2+} into V site, and the sample emerged two new plateaus at approximately 2.8 and 4.2 V for reversible Fe^{2+}/Fe^{3+} and V^{4+}/V^{5+} redox couples, respectively (Fig. 10f). The EPR spectra further indicated that the iron with unpaired 3*d* orbital electron made a favorable effect on activating the high-voltage V^{4+}/V^{5+} redox couple, as well as the migration paths and electronic structure. As a result, in a voltage window of 1.7–4.3 V, the NVFP cathode showed an awesome discharge capacity of 148.2 mAh g^{-1} at 0.5 C (Fig. 10g), an enviable energy density of 501 Wh kg^{-1} and impressive cycling durability (84% capacity retention after 10,000 cycles at 100 C). Impressively, the assembled full cell HC‖NVFP displayed an ultra-stable cycling performance with 63.5% capacity retention after 3000 cycles at 50 C and a material-level energy density of 304 Wh kg^{-1}.

Another desirable doping strategy of bivalent transition metal ions is Co^{2+} or Cu^{2+} doping with minor content, and it has been demonstrated that Co^{2+} or Cu^{2+} substitution can sufficiently improve the electrochemical ability of NVP. Chen et al. [161] reported the effects of different contents of Co^{2+} or Cu^{2+} in $Na_{3+x}V_{2-x}M_x(PO_4)_3$/C (M = Co^{2+}, Cu^{2+}; $x = 0.01–0.05$) and fabricated the optimized $Na_{3.01}V_{1.99}Co_{0.01}(PO_4)_3$/C and $Na_{3.03}V_{1.97}Cu_{0.03}(PO_4)_3$/C cathode materials with high discharge capacities of 116 and 114 mAh g^{-1} at 0.5 C, respectively (Fig. 10h, i), which emphasized the low-level amount of dopants playing a crucial role in affecting the electrochemical performance of NVP. Some other Co^{2+}-doped NVP cathodes such as $Na_3V_{1.93}Co_{0.07}(PO_4)_3$/C were designed via defect regulation by Liu et al. [162], and their study indicated that the Co^{2+} doping not only produced beneficial hole carriers for elevating the electronic conductivity but also enlarged the interplanar spacing to accelerate ionic diffusion rate. Through the theoretical calculations, the introduction of Co^{2+} into V^{3+} site beneficially reduced the bandgap and weakened the energy barrier contributing to fast migration of Na^{+} in NVP (Fig. 10j). Consequently, the $Na_3V_{1.93}Co_{0.07}(PO_4)_3$/C composite achieved a high discharge capacity of 114.4 mAh g^{-1} at 0.1 C and a good reversible capacity of 104.6 mAh g^{-1} at 1 C. Besides, Jiang et al. [163] synthesized a succession of Cu-doped NVP/C composites with different contents of Cu dopants (0, 2.5%, 4%, 5% and 6%) via an oxygen vacancies strategy. The incorporation of Cu with oxygen vacancies could generate more electrons and promote the formation of V^{4+} resulting in a shorter V–O bond, which favorably improved the sodium storage performance and kinetic properties of NVP. Furthermore, the optimized cathode with 5% Cu displayed the highest discharge capacity of 111.4 mAh g^{-1} with capacity retention of 90.4% over 300 cycles at 1 C.

Partial substitution of V by Ni element could sufficiently enhance the cell structural stability and ameliorate ion-diffusion dynamics in the NVP structure owing to the introduction of Ni into V site reducing the sizes of VO$_6$ octahedrons and PO$_4$ tetrahedrons and widening the pathway for Na^{+} diffusion [164]. Zhang et al. [165] prepared Ni-doped NVP/C materials with different content of Ni via a sol–gel method, and the $Na_3V_{1.97}Ni_{0.03}(PO_4)_3$/C cathode showed good rate performance with 98.1 mAh g^{-1} at 5 C compared to the pristine NVP/C (64.3 mAh g^{-1}) (Fig. 10k). According to CV results, all Ni-doped samples possessed lower polarization than the pristine sample, and the $Na_3V_{1.97}Ni_{0.03}(PO_4)_3$/C with the sharpest and narrowest peaks exhibited enhanced structural reversibility.

Mg element is a typically inactive element, which is apt to decrease the theoretical capacity of $Na_3V_{2-x}Mg_x(PO_4)_3$, but additional ionic conductivity and holes produced from Mg^{2+} doping will improve the electrical conductivity. Coupled with Mg^{2+} having a smaller radius of 0.065 nm than V^{3+} (0.074 nm), structural stability is favorably strengthened [166]. The low-dose Mg^{2+}-doped $Na_3V_{1.95}Mg_{0.05}(PO_4)_3$ material yielded superior rate performance with the specific capacity decreased from 112.5 to 94.2 mAh g^{-1} for increasing rate from 1 to 30 C (Fig. 11 a). To explore the effects of large amounts of Mg dopants, Inoishio et al. [167] investigated a new $Na_{3+x}V_{2-x}Mg_x(PO_4)_3$ ($x=0.1$ to 0.7) family. Interestingly, the $Na_{3.2}V_{1.8}Mg_{0.2}(PO_4)_3$ obtained the highest specific capacity compared to other samples, while the $Na_{3+x}V_{2-x}Mg_x(PO_4)_3$ (x over 0.3) materials exhibited declined capacities (Fig. 11b). As shown in the ex situ XRD patterns of $Na_{3.5}V_{1.5}Mg_{0.5}(PO_4)_3$ material (Fig. 11c), an irreversible phase transition emerged in the V^{4+}/V^{5+} redox region, thereby leading to the lower discharge capacity. Subsequently, Ghosh et al. [168] illuminated the Na^+ de/intercalation mechanism of $Na_{3+y}V_{2-y}Mg_y(PO_4)_3$ ($y=0$, 0.25, 0.5, 0.75 and 1) cathode materials, and demonstrated that a complete two-phase process would gradually alter to a solid-solution process, along with the Mg^{2+} content increased in the NVP crystal. As performed in the operando XRD studies of $Na_{3.5}V_{1.5}Mg_{0.5}(PO_4)_3$ and $Na_4VMg(PO_4)_3$ cathodes (Fig. 11d), an intermediate $Na_3V_{1.5}Mg_{0.5}(PO_4)_3$ phase emerged, which was accompanied by 0.5 Na^+ extraction from $Na_{3.5}V_{1.5}Mg_{0.5}(PO_4)_3$ cathode, and the diffraction peaks progressively shifted toward higher 2 θ during the initial charge process, indicating the existence of a solid solution. It was worth noting that the overall cell volume variation only assessed 6.2% compared to the undoped NVP cathode (8.1%), owing to the unextracted Na^+ increasing the volume of Mg-doped phase and decreasing the lattice mismatch between the Na-rich and Na-poor phases, which significantly boosted structural integrity during cycling process. Conversely, a solid-solution mechanism was observed in the fully sodiated $Na_4VMg(PO_4)_3$ material over the entire Na de/intercalation range. To further enhance the electrochemical performance of Mg-doped NVP cathode, Zhao et al. [60] prepared Mg^{2+}-doped porous flower-like $Na_{3+x}V_{2-x}Mg_x(PO_4)_3/C$ ($x=0$, 0.02, 0.04, 0.06) composites. The optimized $Na_{3.04}V_{1.96}Mg_{0.04}(PO_4)_3/C$ (NVMP-4) lattice model was revealed in Fig. 11e. Based on the ex situ XPS analysis, when being charged to 4.2 V, the Mg^{2+} played a novel role to effectively trigger the partial V^{4+} oxidized to V^{5+} in the NVMP-4 cathode material. Coupled with the hierarchical mesoporous structure with carbon layer, the NVMP-4 exhibited exceptional specific capacity (123.8 mAh g^{-1} at 1 C) and excellent rate performance (73.8 mAh g^{-1} at 100 C) (Fig. 11f).

Additionally, Ca-doped NVP material delivers superior rate capability and cycling performance in comparison to Mg-doped counterpart material [169]. Zhao et al. [170] synthesized $Na_3V_{1.95}Ca_{0.05}(PO_4)_3$@C cathode material. The doping of Ca^{2+} with larger radius of 1.00 Å than V^{3+} (0.64 Å) not only enlarged cell volume and lattice spacing to provide broader Na^+ diffusion channels but also generated mixed valence V^{3+}/V^{4+} as charge compensation. The stronger Ca-O bond compared to V–O would remarkably reinforce structural integrity. Through the DFT calculations, the Ca-doped NVP exhibited a disappeared bandgap, lower Na^+ migration energy barrier and higher lattice energy than the undoped NVP (Fig. 11g), which endowed $Na_3V_{1.95}Ca_{0.05}(PO_4)_3$@C cathode with favorable electrochemical performance. The optimized sample delivered unprecedented rate capability with 113 mAh g^{-1} discharge capacity at 50 C and 84 mAh g^{-1} at 500 C, as show in Fig. 11h. Impressively, the $Na_3V_{1.95}Ca_{0.05}(PO_4)_3$@C cathode exhibited superior long-term cycling stability with almost 100% capacity retention after 12,000 cycles at 50 C and only 0.0027% capacity decay after 10,000 cycles at 100 and 200 C. Furthermore, Jiang et al. [171] prepared CNTs enwrapped Ca-doped $Na_3V_{2-x}Ca_x(PO_4)_3$ ($x=0.01$, 0.04, 0.10, Cax-NVP@CNTs) cathode materials via a facile sol–gel approach. Benefiting from the useful regulation of Ca^{2+} substitution, the Ca0.04-NVP@CNTs had a high initial capacity of 104.3 mAh g^{-1} at 5 C and excellent cycling stability with 99% capacity retention at 50 C after 4000 cycles.

In addition, Ti^{4+} possesses a higher valence and smaller radius than V^{3+}, which is beneficial for generating more Na vacancies and enhancing the crystal structure stability. Thus, the Ti^{4+} dopant has been widely employed to substitute V^{3+} for phosphate cathode materials [172, 173]. Ding et al. [174] prepared a series of $Na_3V_{2-x}Ti_x(PO_4)_3/C$ ($x=0$, 0.05, 0.1, 0.15) materials through one-step solid-phase method. With increasing the content of Ti^{4+}, the crystal volume decreased slightly due to TiO_6 octahedron being smaller than VO_6 octahedron, and more vacancies of Na sites were generated for Na^+ diffusion (Fig. 11i). As a result, when the $x=0.1$, the Ti-doped NVP exhibited a satisfactory discharge capability of 123.3 mAh g^{-1} at 0.1 C and excellent rate capability with 89.5 mAh g^{-1} at 30 C (Fig. 11j). Moreover, Huang et al. [175] prepared $Na_{2.85}V_{1.85}Ti_{0.15}(PO_4)_3$ cathode material by a simple solid-phase reaction, delivering a high specific capacity of 101.2 mAh g^{-1} at 10 C with 60% capacity retention after 2000 cycles. Apart from Ti^{4+} substitution, a much higher valence of Mo^{6+} substitution could also improve the

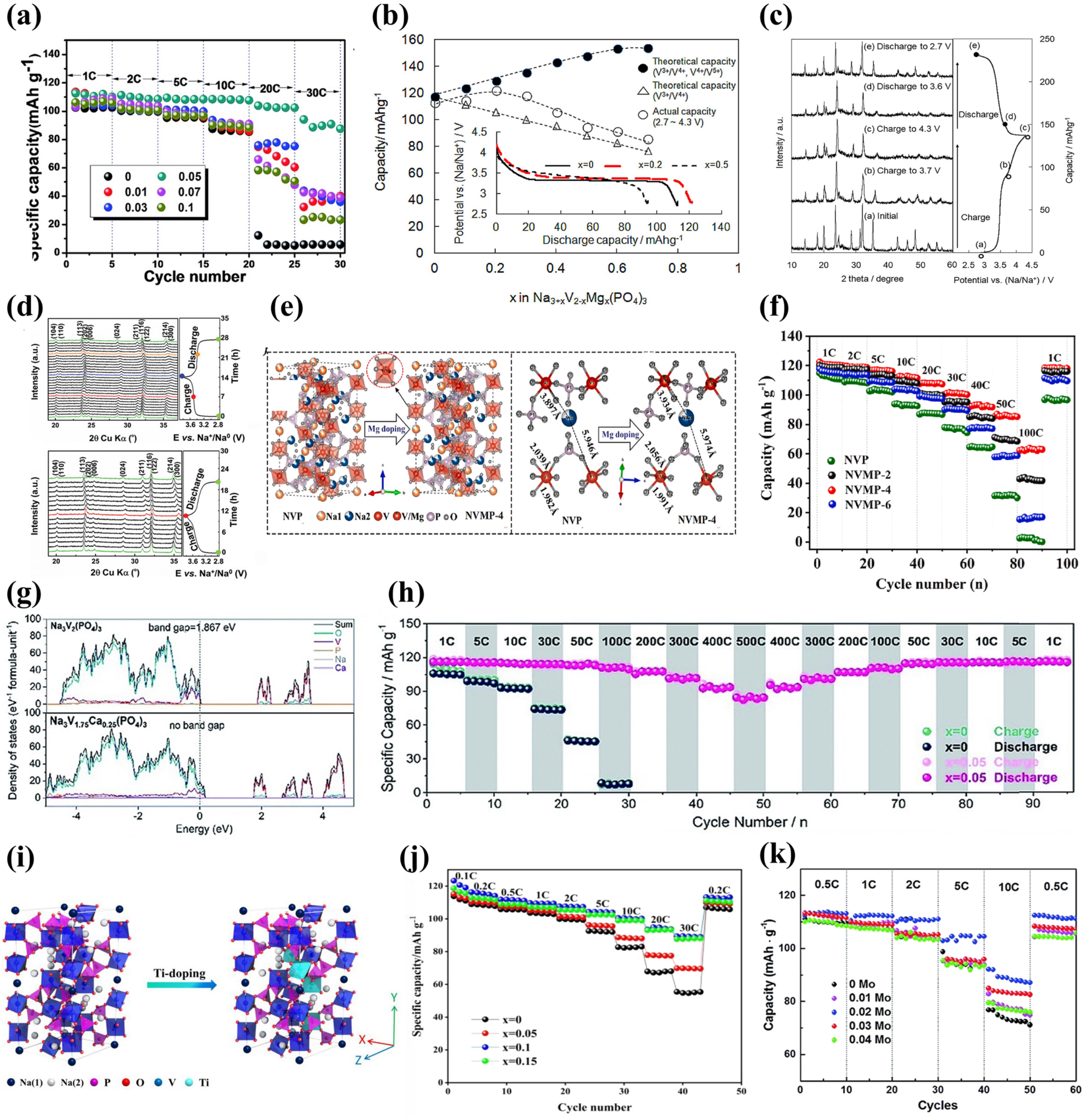

Fig. 11 **a** Rate capability of $Na_3V_{2-x}Mg_x(PO_4)_3/C$ ($x=0$, 0.01, 0.03, 0.05, 0.07 and 0.1). Reproduced with permission [166]. Copyright 2015, Royal Society of Chemistry. **b** First discharge capacity and theoretical capacity for $Na_{3+x}V_{2-x}Mg_x(PO_4)_3$ with different x values, **c** XRD patterns of $Na_{3.5}V_{1.5}Mg_{0.5}(PO_4)_3$ at different charge–discharge state. Reproduced with permission [167]. Copyright 2017, Wiley-VCH. **d** Operando XRD patterns of $Na_{3+y}V_{2-y}Mg_y(PO_4)_3$ with $y=0.5$ (top) and 1 (below). Reproduced with permission [168]. Copyright 2021, Wiley-VCH. **e** Crystallographic framework of NVP and NVMP-4, **f** rate performance of $Na_{3+x}V_{2-x}Mg_x(PO_4)_3/C$. Reproduced with permission [60]. Copyright 2024, Elsevier. **g** Density of states (DOS) for $Na_3V_2(PO_4)_3$ and $Na_3V_{1.75}Ca_{0.25}(PO_4)_3$, **h** rate capability of $Na_3V_{1.95}Ca_{0.05}(PO_4)_3$@C and $Na_3V_2(PO_4)_3$@C electrodes. Reproduced with permission [170]. Copyright 2019, Royal Society of Chemistry. **i** Schematic diagram of crystal structure of Ti-doped NVP/C, **j** rate capability of Ti-doped NVP/C. Reproduced with permission [174]. Copyright 2023, American Chemical Society. **k** Rate performance of $Na_{3-5x}V_{2-x}Mo_x(PO_4)_3$ ($x=0.01$–0.04). Reproduced with permission [176]. Copyright 2018, Royal Society of Chemistry

sodium storage performance of NVP. Li et al. [176] fabricated a series of $Na_{3-5x}V_{2-x}Mo_x(PO_4)_3/C$ ($x = 0$, 0.01, 0.02, 0.03, 0.04) cathode materials using a solid-state reaction. Due to the higher valence of Mo^{6+}, vacancies would be generated to balance the charge in the NVP system, favorably facilitating the transmission of Na^+ ion for faster diffusion kinetics. The optimized $Na_{2.9}V_{1.98}Mo_{0.02}(PO_4)_3/C$ cathode revealed a superior reversible capacity of 90 mAh g^{-1} at 10 C (Fig. 11k) and better cycling performance with 83.5% capacity retention after 500 cycles.

3.2.2.3 Multiple-Ions Substitution Although single cationic substitution at V site can effectively improve the electrochemical performance of NVP cathode materials, some limitations still exist. Multiple-ions doping or substitution in NVP can integrate the respective advantages of individual cation and earn favorable electrochemical properties, which covers the binary substitution, ternary substitution and high-entropy effects.

For binary substitution, Zhao et al. [140] selected Fe and Ni elements to partially substitute V and synthesized $Na_3Fe_{1-x}VNi_x(PO_4)_3$ ($x = 0$, 0.2, 0.4, 0.8) cathode materials by a sol–gel method. The crystal structure of Fe and Ni co-doped NVP (NFVNP) is shown in Fig. 12a. Too much Ni content exerted an adverse impact on the specific capacity. Meanwhile, the Ni doping performed a better improving effect than Fe in declining charge transfer resistance. The modified $Na_3Fe_{0.8}VNi_{0.2}(PO_4)_3$ cathode obtained a reversible capacity of 102.2 mAh g^{-1} (close to its theoretical value 105 mAh g^{-1}) at 0.1 C in the voltage region of 2.0–3.8 V with two distinct plateaus associated with Fe^{2+}/Fe^{3+} and V^{3+}/V^{4+} redox reactions (Fig. 12b). The $Na_3Fe_{0.8}VNi_{0.2}(PO_4)_3$ cathode displayed favorable low-temperature performance with 89.7 mAh g^{-1} capacity at 2 C and − 10 °C and stable cycling performance with 84.6% capacity retention after 1400 cycles (Fig. 12c). Kim et al. [110] proposed that the Fe and Cr co-doping could significantly enhance structural stability, increase electrical conductivity and optimize phase transition behavior of NVP cathode (Fig. 12d). The optimized $Na_3V_{1.5}Cr_{0.4}Fe_{0.1}(PO_4)_3$ cathode material achieved ultrahigh-rate capability and outstanding cycle life, delivering a about 71 mAh g^{-1} discharge capacity at 100 C with 95% capacity retention after 10,000 cycles (Fig. 12e, f). Moreover, Zhao et al. [177] investigated the $Na_4FeV_{1/3}Ti_{2/3}(PO_4)_3$ (NFVT) cathode and uncovered quasi-monophase behavior in the NFVT material, which was related to multiple electron transfer of Ti^{2+}/Ti^{3+}, Fe^{2+}/Fe^{3+} and $V^{3+}/V^{4+}/V^{5+}$. Figure 12g displays four regions based on the potential of redox reaction during the charge and discharge processes of NFVT. The potential platform of Fe and Ti tended to be more sloping and the potential platform of V in NFVT was leaner than that in $Na_4FeV(PO_4)_3$ (NFV), leading to increased specific capacity. Meantime, the additional Ti^{3+} in NFVT was beneficial for the enhancement of Fe^{2+}/Fe^{3+} and V^{4+}/V^{5+} reactivity (Fig. 12h). The quasi-monophase process in NFVT was studied in depth by in situ XRD in Fig. 12i. Especially, there was obvious differentiation at about 32° in NFV and NFVT accompanied by a frail peak and a successive peak, respectively. As a result, the NFVT with symmetric quasi-monophase presented highly reversible phase transition and an integral crystal structure, driving an ultrafast charging ability (only 3.63 min to reach 80% state of charge at 2 C), stable cycling performance with 0.043% capacity degradation per cycle, and an ideal energy density of over 350 Wh g^{-1} (Fig. 12j).

In addition, the Mn^{3+} substitution in NVP is still plagued with the Jahn–Teller distortion, giving rise to unsatisfactory cyclic stability and rate performance. Therefore, introducing other metal ions to inhibit the Jahn–Teller effect of Mn^{3+} is employed to obtain high-performance NVP cathodes [178]. Chen et al. fabricated a sequence of $Na_{3.25+x}V_{1.75-x}Mn_xNi_{0.25}(PO_4)_3$ ($x = 0$, 0.25, 0.5, 0.75, 1, VMN-x) cathode materials by Ni and Mn co-substitution. The study demonstrated that Mn^{2+} played a vital role to elevate the reversible capacity attributed to the additional Mn^{2+}/Mn^{3+} redox reaction. The inert Ni^{2+} ion acted as a stabilizer was favor for suppressing the Jahn–Teller effect of Mn ions and thus reinforced the crystal structural integrity. The VMN-0.5 exhibited the best electrochemical performance, yielding a high discharge capacity of 108.1 mAh g^{-1} at 0.2 C and an initial capacity of 80.1 mAh g^{-1} at 20 C with 63.5% capacity retention after 10,000 cycles (Fig. 12k). Hu et al. [125] designed $Na_{3.2}MnTi_{0.8}V_{0.2}(PO_4)_3$ (NMTVP-0.2) cathode with reversible 3.2-electrons redox reaction, which contributed from the five redox couples of V^{5+}/V^{4+} (≈ 4.1 V), Mn^{4+}/Mn^{3+} (≈ 4.0 V), Mn^{3+}/Mn^{2+}(≈ 3.6 V), V^{4+}/V^{3+}(≈ 3.4 V) and Ti^{4+}/Ti^{3+} (≈ 2.1 V) during the electrochemical reaction process (Fig. 12l). As a result, the NMTVP-0.2 yielded an appealing reversible capacity of 172.5 mAh g^{-1} at 50 mA g^{-1} (Fig. 12m) and an admirable energy density of 527.2 Wh kg^{-1}.

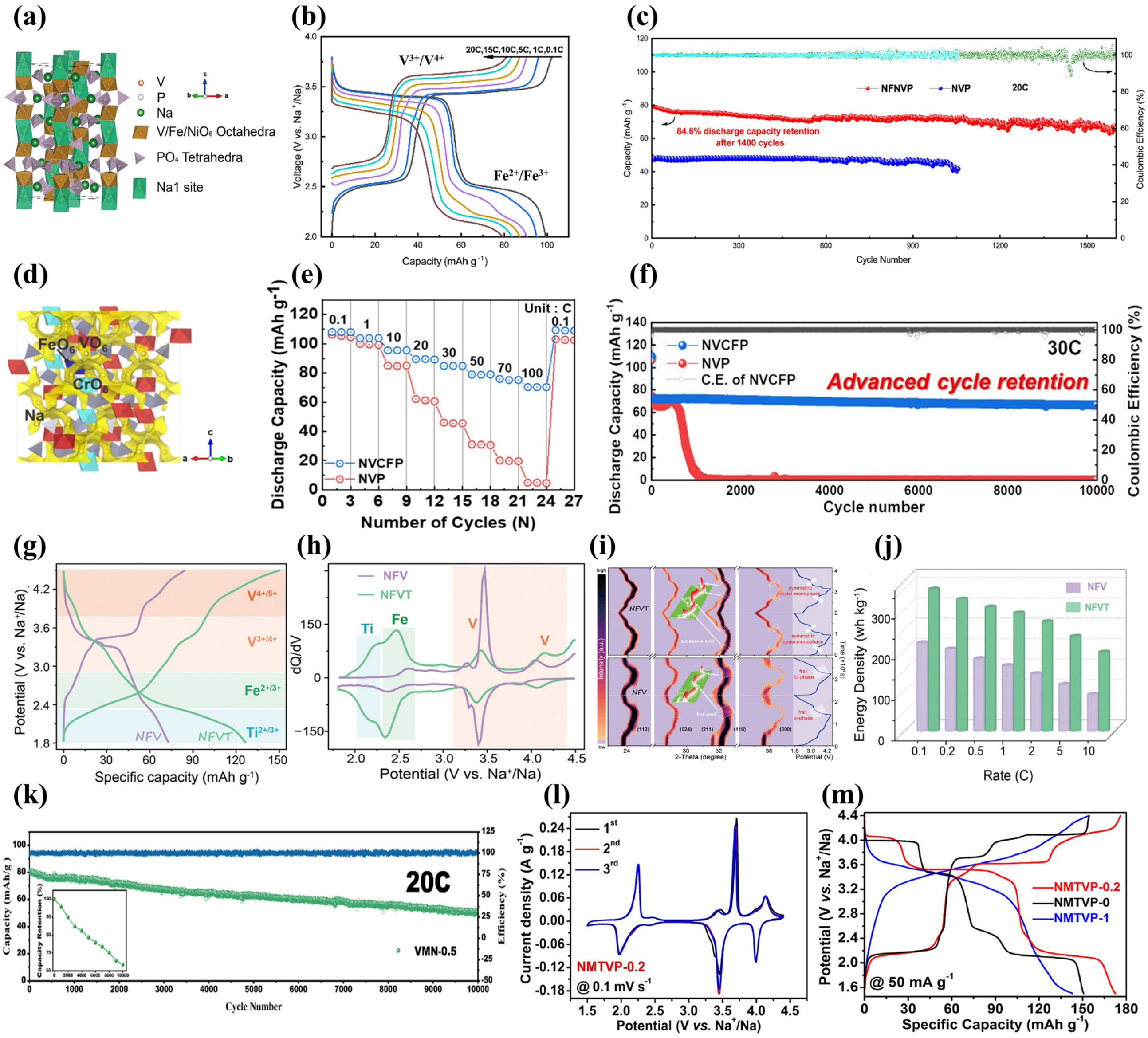

Fig. 12 **a** Crystal structure model of NFVNP, **b** charge–discharge curves at different rates of NFVNP in 2.0 – 3.8 V, **c** cycling performance of NFVNP and NVP at 20 C. Reproduced with permission. [140] Copyright 2022, American Chemical Society. **d** Crystal structure model of NVCFP, **e** rate capability and **f** cycling performance of NVCFP and NVP. Reproduced with permission. [110] Copyright 2024, American Chemical Society. **g** Charge–discharge curves at 0.1 C and **h** dQ/dV curves of NFV and NFVT, **i** in situ XRD contour map of NFVT and NFV cathodes along with the first two cycles at 0.1 C, **j** energy density at different rates in NFV and NFVT half cells. Reproduced with permission. [177] Copyright 2024, Wiley-VCH. **k** Cycle performance of VMN-0.5 at 20 °C. Reproduced with permission. [111] Copyright 2023, Wiley-VCH. **l** CV curves of NMTVP-0.2, **m** charge–discharge curves of NMTVP-1, NMTVP-0.2 and NMTVP-0.2. Reproduced with permission. [125] Copyright 2023, Wiley-VCH

Compared with binary substitution, ternary substitution possesses the ability of multiple dimensional optimized regulation. Sun et al. [113] carried out a fresh type of Fe/Mn/Co co-doped $Na_{3+2x}V_{2-3x}(FeMnCo)_x(PO_4)_3$ ($x = 0.05$, 0.1, 0.15, NFMC-x) cathode materials. The heteroatomic introduction of larger ionic radius of Mn^{2+} and Co^{2+} (Mn^{2+}: 67 pm, Co^{2+}: 74.5 pm, V^{3+}: 64 pm) enlarged cell volume and provided plentiful crystal gap to boost Na^+ diffusion kinetics, and the introduction of smaller radius of Fe^{3+} (55 pm) not only regulated the crystalline state by sustaining the Mn and Co at low state (M^{2+}) but also ameliorated lattice distortion originated from the excessive ionic introduction. In the lattice of NFMC-0.1 compared to NVP, as shown in Fig. 13 a, the distance of adjacent Na2 and V increased from 3.88 to 3.90 Å for Na2 and from 5.98 to 6.14 Å for V and the V–O band length in MO_6 unit increased from 1.97 to 2.22 Å. Therefore, it was the change of M–O band length that was contributive to provide larger removable space for Na ion's migration and gain or loss electrons and perfect the electrochemical performance of NVP. Moreover, the synergy of ternary substitution in NFMC cathodes produced an extra high-voltage platform of 3.8 V associated with the multiple redox couples of $Mn^{2+}/Mn^{3+}/Mn^{4+}$, Co^{2+}/Co^{3+} and V^{4+}/V^{5+}, leading to increased capacities. Figure 13b presents

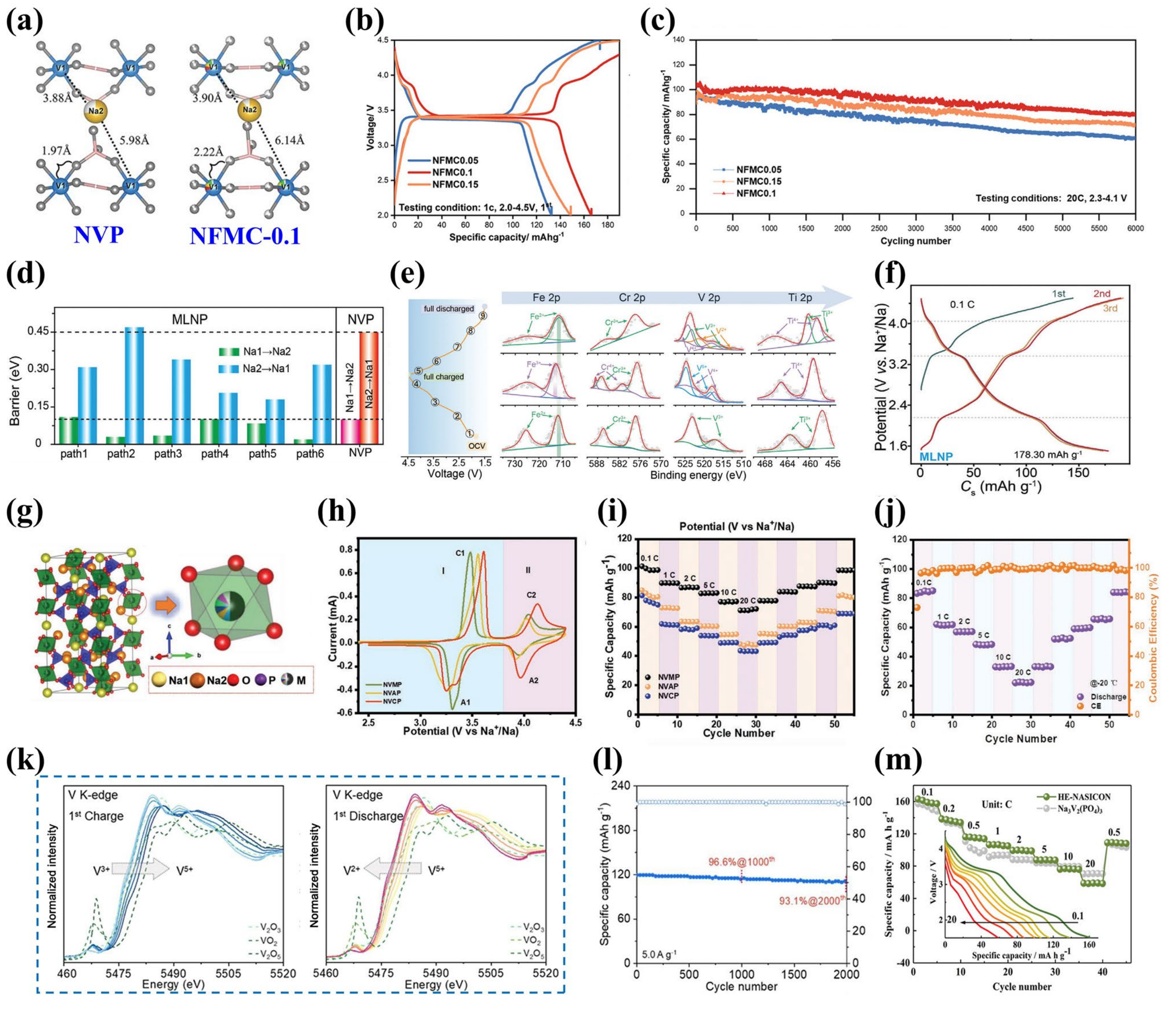

Fig. 13 **a** Visualization of crystal structure and atomic occupation of NVP and NFMC0.1, **b** charge–discharge curves and **c** cycling performances of NFMC samples. Reproduced with permission [113]. Copyright 2023, Wiley-VCH. **d** Comparison of migration energy barriers within different Na^+ groups of MLNP and NVP, **e** XPS spectra of Fe 2*p*, Cr 2*p*, V 2*p* and Ti 2*p* spectra at different charge/discharge states, **f** charge–discharge curves at 0.1 C of MLNP. Reproduced with permission [126]. Copyright 2024, Wiley-VCH. **g** Schematic of NVMP crystal structure, **h** CV curves at 0.2 mV s^{-1} and **i** rate performance of NVMP, NVAP and NVCP cathodes, **j** rate capability of NVMP cathode at − 20 °C. Reproduced with permission [180]. Copyright 2023, Wiley-VCH. **k** V K-edge XANES spectra of HE-V1.6 in charge and discharge processes, **l** cycling performance of HE-V1.6 electrode at 5.0 A g^{-1}. Reproduced with permission [181]. Copyright 2024, American Chemical Society. **m** Rate performance of HE-NASICON and $Na_3V_2(PO_4)_3$ cathodes. Reproduced with permission [182]. Copyright 2022, Wiley-VCH

that the specific capacities of all doped samples surpassed the theoretical capacity (117.6 mAh g^{-1}) of NVP, and the NFMC-0.1 cathode material exhibited the best rate capacity with highly structural stability and excellent cycling performance (Fig. 13c). In addition, Gu et al. [126] reported that a homeostatic solid-solution reaction mechanism could be achieved by diversifying reaction pathways in the as-prepared $Na_{3.5}Fe_{0.5}V_{0.5}Cr_{0.5}Ti_{0.5}(PO_4)_3$ (MLNP) cathode material and combining the merits of progressive TM ions (V, Fe, Ti and Cr) with multilevel redox couples, which overcame the high barrier of bottleneck of V^{4+}/V^{5+} at high voltage. In the reciprocal migration of Na1 ↔ Na2 course, the process of Na1 → Na2 (path1) was sluggish with endothermic process, but the Na2 → Na1 (path2) was exothermic with low barrier, indicating that the absorb of inactive Na1 was more difficult than its release. As shown in Fig. 13d, the MLNP with lower migration energy barriers of pathways than NVP further encouraged the absorb of inactive Na1, enabling a higher capacity. The different migration modes combined with different sites were attributed to the various TMO_6 octahedra in MLNP accompanying multilevel redox reactions, compared to only VO_6 in NVP. Through the ex situ XPS analysis in Fig. 13e, a successive oxidization course of Ti^{3+}/Ti^{4+}, Fe^{2+}/Fe^{3+}, V^{3+}/V^{4+} and Cr^{3+}/Cr^{4+} in the charge process and a successional reduction course of Cr^{4+}/Cr^{3+}, V^{5+}/V^{4+}, V^{4+}/V^{3+}, Fe^{3+}/Fe^{2+}, Ti^{4+}/Ti^{3+} and V^{3+}/V^{2+} in the discharge process were observed, effectively propelling sufficient Na storage and enhancing reversible capacity in subsequent cycling. The variation of cell volume was barely 1.73% in MLNP material. Moreover, the MLNP cathode delivered a high reversible capacity of 178.30 mAh g^{-1} at 0.1 C (Fig. 13f), met with the pursuit of energy density reaching 440 Wh kg^{-1}, and exhibited fascinating cycling durability with 0.0061% capacity decay per cycle for 500 cycles at 5 C.

Recently, to further improve the electrochemical performance of NVP, a high-entropy concept involving the incorporation of five or more TM elements with apt molarity is employed to optimize NASICON-type cathode materials [112]. High-entropy substitution is beneficial for the optimization of crystal structure resulting from the chemical orders for mixed cations and generated vacancies [179–181]. Li et al. [180] designed a high-entropy $Na_3VAl_{0.2}Cr_{0.2}Fe_{0.2}In_{0.2}Ga_{0.2}(PO_4)_3$ (NVMP) cathode material by introducing five metal elements (Al, Cr, Fe, In, Ga) into V site (Fig. 13g), aiming to suppress the irreversible phase transition at the voltage range of over 4 V. Two redox pairs corresponding to V^{3+}/V^{4+} and V^{4+}/V^{5+}, presenting lower polarization and higher reversibility of Na^+ de/intercalation compared to $Na_3VAl(PO_4)_3$ (NVAP) and $Na_3VCr(PO_4)_3$ (NVCP), were distinguished in Fig. 13h. According to the ex situ XRD measurement, all characteristic peaks exhibited high reversibility during the charge and discharge processes, disclosing the crystal structural evolution of NVMP corresponding to a beneficial solid-solution behavior for improving electrochemical reversibility and structural robustness. The high-entropy effect played a pivotal role to inhibit the irreversible phase transition caused by high potential V^{4+}/V^{5+} redox reaction. Thereby, the NVMP cathode with a minimal cell volume change of 1.1% achieved a high discharge capacity of 102 mAh g^{-1} at 0.1 C (Fig. 13i) and could obtain satisfactory rate performance (83 mAh g^{-1} reversible capacity 0.1 C) even at an extreme temperature of − 20 °C (Fig. 13j). Hao et al. [181] reported a $Na_{3.32}V_{1.6}Cr_{0.08}Fe_{0.08}Mn_{0.08}Mg_{0.08}Ca_{0.08}(PO_4)_3$ (HE-NVP) cathode material via a simple sol–gel approach. In combination of in situ XANES and in situ XRD results, a successful reversible activation of V^{4+}/V^{5+} redox couple (Fig. 13k), a solid-solution reaction and a biphasic conversion reaction accompanied by highly structural reversibility were confirmed. The HE-NVP afforded a remarkable discharge capacity of 120 mAh g^{-1} at 5.0 A g^{-1} with 93.1% capacity retention after 2000 cycles (Fig. 13l). Moreover, some other high-entropy polyanionic cathode materials such as $Na_{3.4}Fe_{0.4}Mn_{0.4}V_{0.4}Cr_{0.4}Ti_{0.4}(PO_4)_3$ (HE-NASICON) were proposed by Li et al. [182]. Their research unveiled that the HE-NASICON achieved multi-cationic redox reactions and mitigated the structural degradation in a wide voltage window (1.5–4.5 V), enabling a superior reversible capacity of 161.3 mAh g^{-1} at 0.1 C (Fig. 13m), along with a robust structural stability.

3.2.3 *PO_4^{3-}-Site Doping or Substitution*

Compared to the replacement of Na and V sites, research on the substitution of inactive anion PO_4^{3-} in NVP is less. PO_4^{3-}-site doping or substitution, as a feasible route, can also effectively retard the capacity loss and enhance cycling stability. At present, anion doping is mainly concluded to two aspects, the monoatomic anion F^- substitution and the multivalent anion substitution such as SiO_4^{4-} [183], SO_4^{2-} [184], BO_3^{3-} [185, 186] and MoO_4^{2-} [187]. Generally, the F^- substitution has been widely explored compared with multivalent anion substitution [53, 185].

3.2.3.1 Monoatomic Anion Substitution Due to the anion F^- featured by strong electronegative and inductive effect, a higher redox potential could be obtained during the charge and discharge processes for the F-doped NVP cathodes, which considerably boosted sodium storage performance [188–190]. Chen et al. [191] synthesized a series of F-doped $Na_3V_2(PO_4)_{3-x}F_x$/C ($x=0$, 0.01, 0.04, 0.07) cathode materials via a simple solid-state method. They demonstrated that the F-substitution not only mitigated the structural degradation from irreversible $Na_3V_2(PO_4)_3$ to $V_2(PO_4)_3$ (Fig. 14 a), but also effectively shortened the pathways of Na^+ ion and electron transportation. The variation of cell volume of F-doped NVP cycled at 200 mA g^{-1} for 1000 cycles is calculated in Fig. 14b, exhibiting strikingly declined shrinkage of cell volume in all F-doped NVP materials compared to NVP. Therefore, the optimized $Na_3V_2(PO_4)_{1.93}F_{0.07}$ cathode material achieved enhanced structural stability and improved Na^+ kinetics behavior, rendering better rate capability with a good discharge capacity of 113 mAh g^{-1} at 10 mA g^{-1} (Fig. 14c) and 86% capacity retention after 1000 cycles at 200 mA g^{-1}. Subsequently, Chen et al. [192] reported a F-doped and V-defects $Na_3V_{1.98}(PO_4)_{1.97}F_{0.3}$/C cathode with an extra potential platform at about 4.0 V corresponding to the V^{4+}/V^{5+} redox pair, presenting 116.9 mAh g^{-1} reversible capacity at 0.1 C and an impressive D_{Na^+} of 3.66×10^{-13} cm^2 s^{-1} which was three orders of magnitude higher than that of undoped NVP/C material (7.41×10^{-16} cm^2 s^{-1}).

3.2.3.2 Multivalent Anion Substitution It is the multivalent anion substitution that is supposed to be more effective and feasible to realize the precisely optimized preparation owing to the more similar anionic structure in comparison to the monoatomic anion F^- [183]. Except for the BO_3^{3-} holding triangle ionic structure, the ionic structures of SiO_4^{4-}, SO_4^{2-} and MoO_4^{2-} are identical with the tetrahedral PO_4^{3-}, presenting better electrochemical performance by virtue of the structural compatibility than BO_3^{3-} [185, 187, 193, 194]. Hu et al. [185] comprehensively investigated the evolution of crystal and electronic structure of $Na_3V_2(PO_4)_{3-x}(BO_3^{3-})_x$ ($0\leq x\leq1$) cathode materials. It was unveiled that the BO_3^{3-} substitution played a critical role to optimize crystal structure and effectively narrow the bandgap in a new energy state. As manifested in Fig. 14d, the BO_3^{3-} would occupy the tetrahedral interstitial site, which almost altered the framework of the optimized $Na_3V_2(PO_4)_{3-1/6}(BO_3)_{1/6}$ material. Additionally, the strength of B-O bond was much weaker than that of P-O bond and the V–O band length was marginally reduced owing to the substitution of B (Fig. 14e), promoting the migration of Na^+ ions. The $Na_3V_2(PO_4)_{3-1/6}(BO_3)_{1/6}$ exhibited improved discharge capacities of 100 and 70 mAh g^{-1} at 5 C and 10 C, respectively (Fig. 14f). Qiu et al. [186] also pointed out the profound influence of BO_3^{3-} substitution on the phase transition and electrochemical reactions of NVP. The anion group BO_3^{3-} into PO_4^{3-} site played three roles to expand the domain of solid solution, accelerate the structural transformation to V^{2+}-containing phase and mitigate the short-scale heterogeneity of P and Na nucleus.

Introducing isostructural SiO_4^{4-} into NVP framework would greatly optimize NVP lattice and improve its rate capability and cyclic stability. To be specific, the larger radius and lower electronegativity of Si^{4+} compared to P^{5+} (Si^{4+}: 0.024 nm vs. P^{5+}: 0.017 nm; electronegativity: Si^{4+}: 1.90 vs. P^{5+}: 2.19) rendered more stronger Si–O bond than P-O bond, which enhanced structural stability. Furthermore, the produced structural variation would broaden the ion's diffusion pathways and thus increase electrical conductivity. The as-synthesized $Na_{3.1}V_2(PO_4)_{2.9}(SiO_4)_{0.1}$ cathode (Fig. 14g) impressively obtained an increased occupancy ratio at Na2 site from 0.7090 to 0.7395, which harvested higher Na storage capacity with a higher specific capacity of 82.5 mAh g^{-1} at 20 C compared to undoped NVP with only 49.7 mAh g^{-1} (Fig. 14h) [183]. Chen et al. [195] synthesized $Na_{3.1}V_2(PO_4)_{2.9}(SiO_4)_{0.1}$/C@rGO cathode material, and demonstrated that the SiO_4^{2-} not only widened the transportation channels of Na^+ but also was beneficial for the formation of vesicular structure, which enlarged contact region between active material and electrolyte. Coupled with the advantages of rGO, the optimized cathode delivered a favorable discharge capacity of 113.6 mAh g^{-1} at 0.1 C and good cyclic stability with 79.0% capacity retention after 1000 cycles at 1 C (Fig. 14i). In combination of DFT calculations and thermodynamic analysis, Kapoor et al. [184] exploited the different effects of the partial or full substitution of PO_4^{3-} by SiO_4^{4-} or SO_4^{2-} and unlocked the uncharted multicomponent Na-V-P-(Si/S)-O quinary phase diagram (Fig. 14j). Specifically, the SO_4^{2}-doping could raise the voltage of each V redox pairs including V^{2+}/V^{3+}, V^{3+}/V^{4+} and V^{4+}/V^{5+} at the cost of the massive amount of Na^+ intercalated. But owing to the enlargement of low voltage of V^{2+}/V^{3+}, the overall average voltage would be lower. Oppositely, the replacement of PO_4^{3-} by a dose of SiO_4^{4-} dopants would activate the high voltage of V^{4+}/V^{5+} and thus enhance

https://doi.org/10.1007/s40820-024-01526-x

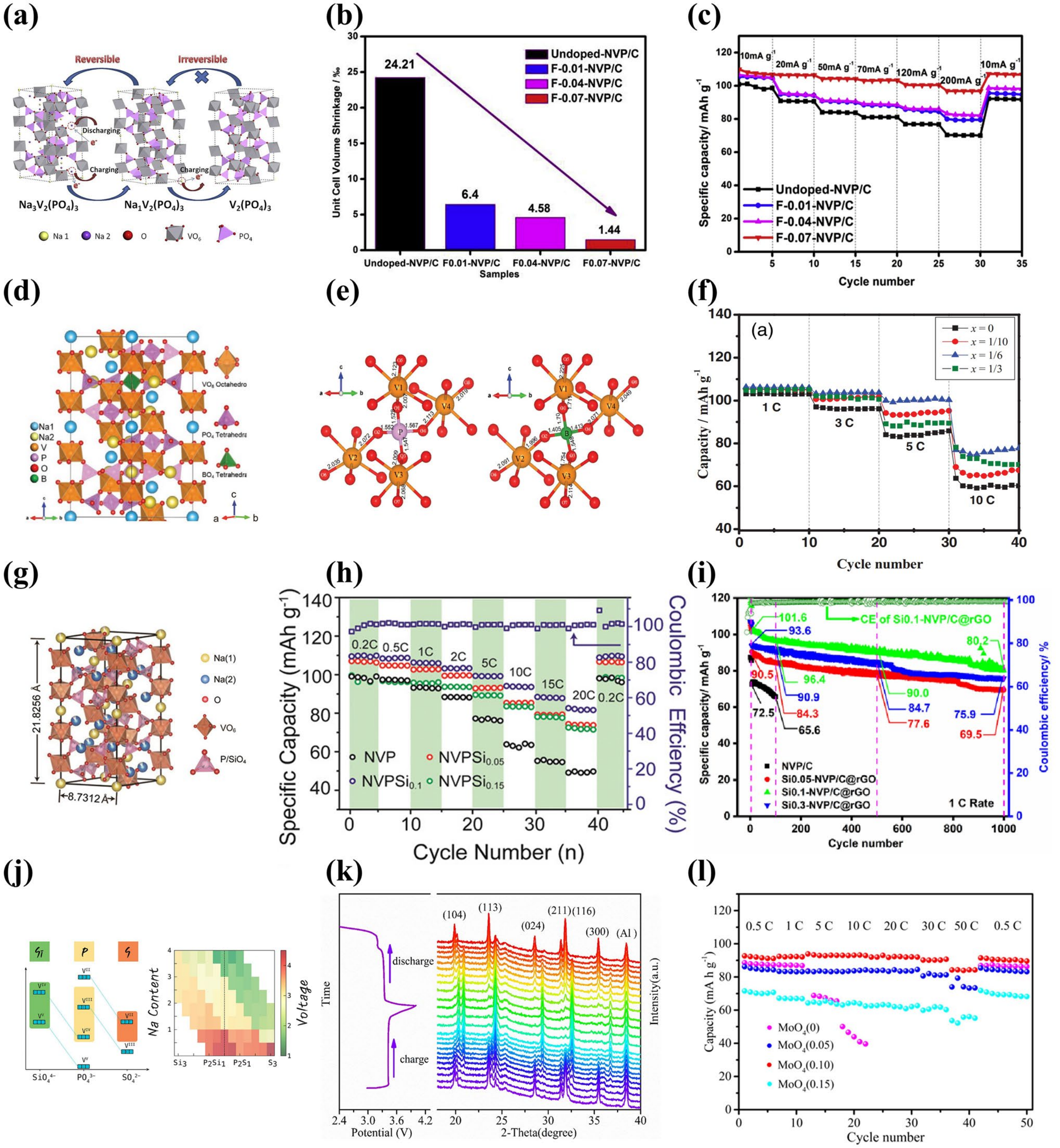

Fig. 14 **a** Schematic diagram of structural degradation for $Na_3V_2(PO_4)_3$, **b** percentage of unit cell volume shrinkages before and after 1000 cycles at 200 mA g^{-1} and **c** rate capability of $Na_3V_2(PO_4)_{3-x}F_x$/C ($x=0$, 0.01, 0.04 and 0.07) composites. Reproduced with permission [191]. Copyright 2017, Wiley-VCH. **d** Crystal structure of $Na_3V_2P_{3-x}B_xO_{12}$ ($x=1/6$), **e** local distortion around the doping site of $Na_3V_2P_{3x}B_xO_{12}$ (Left) ($x=0$) and (Right) ($x=1/6$), **f** rate capability of $Na_3V_2P_{3-x}B_xO_{12}$ ($x=0$, 1/10, 1/6, 1/3) electrodes. Reproduced with permission [185]. Copyright 2017, Wiley-VCH. **g** Schematic illustration of crystal structure $NVPSi_{0.1}$, **h** rate performance of $NVPSi_x$ ($x=0$, 0.05, 0.10, 0.15). Reproduced with permission [183]. Copyright 2020, Wiley-VCH. **i** Cycling performance of $Na_{3+x}V_2(PO_4)_{3-x}(SiO_4)_x$/C@rGO ($x=0.05$, 0.1, 0.3) at 1 C. Reproduced with permission [195]. Copyright 2020, Wiley-VCH. **j** Multicomponent Na-V-P-(Si/S)-O quinary phase diagram. Reproduced with permission [184]. Copyright 2022, American Chemical Society. **k** XRD patterns of NVP-MoO_4 (0.10) electrodes during the first charge–discharge cycle, **l** rate capability of NVP-MoO_4 (x) cathodes. Reproduced with permission [187]. Copyright 2021, Elsevier

the average voltage without necessary extraction of Na from the Na1 site, which was not experimentally accessible for the activation of V^{4+}/V^{5+} in practical NVP composites.

Furthermore, Liu et al. [187] firstly proposed that MoO_4^{2-} partially replacing PO_4^{3-} could also propel Na^+ diffusion kinetics and sodium storage performance. They developed a succession of $Na_{(3+2x)}V_2(PO_4)_{(3-x)}(MoO_4)_{(x)}$ (NVP-MoO_4(x), $x = 0$, 0.05, 0.10, 0.15) cathode materials via a convenient solid-state reaction. The result of pDOS revealed the effect of MoO_4^{2-} substitution, and the modified NVP-MoO_4(0.1) sample obtained a reduced bandgap (3.67 eV) compared to NVP-MoO_4(0) (4.97 eV) accompanied by some newborn energy states at the bottom of conduction band, which further optimized the local lattice structure and electronic structure of NVP. Meantime, the in situ XRD measurement presented highly structural reversibility of NVP-MoO_4(0.1) sample during the subsequent electrochemical cycling process (Fig. 14k). Consequently, the obtained NVP-MoO_4(0.1) cathode performed a dramatic improvement in the rate capability with 84.2 mAh g^{-1} discharge capacity at 50 C (Fig. 14l).

3.2.4 Multi-Sites Doping or Substitution

Multi-sites doping or substitution by virtue of the different doping sites in the NVP system, an optimization strategy combined with their independent benefits, has favorable contribution to the enhancement of electrochemical performance [196]. To substitute the Na and PO_4^{3-} sites, Dou et al. [197] reported a $Na_{3.24}K_{0.10}V_{2.01}(PO_4)_3(SiO_4)_{0.14}$ (KSi-NVP) cathode material. The introduction of SiO_4^{3-} into PO_4^{3-} site elevated the occupancy ration at Na2 site from 0.3489 to 0.4041, suggesting that more Na^+ would participate electrochemical reaction to increase capacity. Meanwhile, the introduction of K^+ into Na site as pillar ions lowed the occupancy ration at Na1 site from 0.1484 to 0.1176, which was of significance for the enhancement of structural stability in the KSi-NVP material. The optimized KSi-NVP exhibited a satisfactory discharge capacity of 116.3 mAh g^{-1} at 0.5 C, as well as ultra-long cycling life for 10,000 cycles at 20 C with merely 0.0056% capacity decay per cycle (Fig. 15a, b).

Besides, Chen et al. [198] proposed a Fe and F co-doped strategy by replacing the V and PO_4^{3-} sites and synthesized a series of $Na_3V_{2-x}Fe_x(PO_4)_{3-x}F_{3x}$/C@CNTs ($x = 0$, 0.01, 0.03, 0.05, 0.07) materials. The doping of cationic Fe^{3+} not only enlarged intercellular voids but also facilitated the formation of porous structure (Fig. 15c), which greatly boosted the ionic conductivity and ameliorated the volume expansion/shrinkage. F^- was favor for reducing the particle size, which shortened the diffusion pathways of Na^+ and further improved the ionic conductivity. Coupled with the highly conductive interconnected network by the combination of carbon coating and CNTs, ultimately, the $Na_3V_{1.95}Fe_{0.05}(PO_4)_{2.95}F_{0.15}$/C@CNTs harvested eye-catching high-rate capability and splendid long cycling stability, delivering a 92.2 mAh g^{-1} capacity at 120 C with 65.1% capacity retention after 3000 cycles and 80.1 mAh g^{-1} at 450 C (Fig. 15d). Subsequently, Chen et al. [188] selected Ta^{5+}, having higher valence and larger size than V^{3+}, to partially substitute V site and F^- to partially substitute PO_4^{3-} site, and obtained $Na_3V_{1.95}Ta_{0.05}(PO_4)_{1.93}F_{0.21}$/C@CNTs (NVTPF0.07/C@CNTs) composites. The n-type effect of Ta^{5+} dopant effectively increased electronic conductivity by inducing more amounts of free electrons. The introduction of Ta^{5+} expanded the transportation pathways of Na^+ and strengthened the structural stability of NVP system. Interestingly, a nascent conductive TaN phase incorporated with NVP bond formed a specific TaN/NVP heterojunction (Fig. 15e), significantly accelerating the Na^+ diffusion. Benefiting from the synergistic effects of Ta and F co-doping, the NVTPF0.07/C@CNTs cathode material showed a reversible capacity of 121.5 mAh g^{-1} at 0.1 C, 63.49% capacity retention after 1500 cycles at 60 C and exceptional rate performance with 91.3 mAh g^{-1} specific capacity at 10 C (Fig. 15f-h). In addition, the replacement of Na and V sites by K^+/Mg^{2+} co-doping was achieved by Das et al. [115]. The modified $Na_{2.91}K_{0.09}V_{2.93}Mg_{0.07}(PO_4)_3$@C/rGO (NVPMK@C/rGO) cathode material displayed a high discharge capacity of 116.6 mAh g^{-1} at 1 C (Fig. 15i). Together, the assembled symmetrical full cell by NVPMK@C/rGO electrodes sustained 95% capacity retention after 500 cycles at 10 C (Fig. 15j).

Based on the above discussion, it can be found that the foreign-ion doping or substitution in the Na, V and PO_4^{3-} sites is a very effective optimization strategy to improve the electrochemical performance of NVP cathode material. Specifically, it is worthwhile to consider that some transition metal elements with the advantages of eco-friendliness, low-cost and enabling high electrochemical properties, such as Fe, Mn, Al, Mg and Ti, are responsible for the best metal ion's

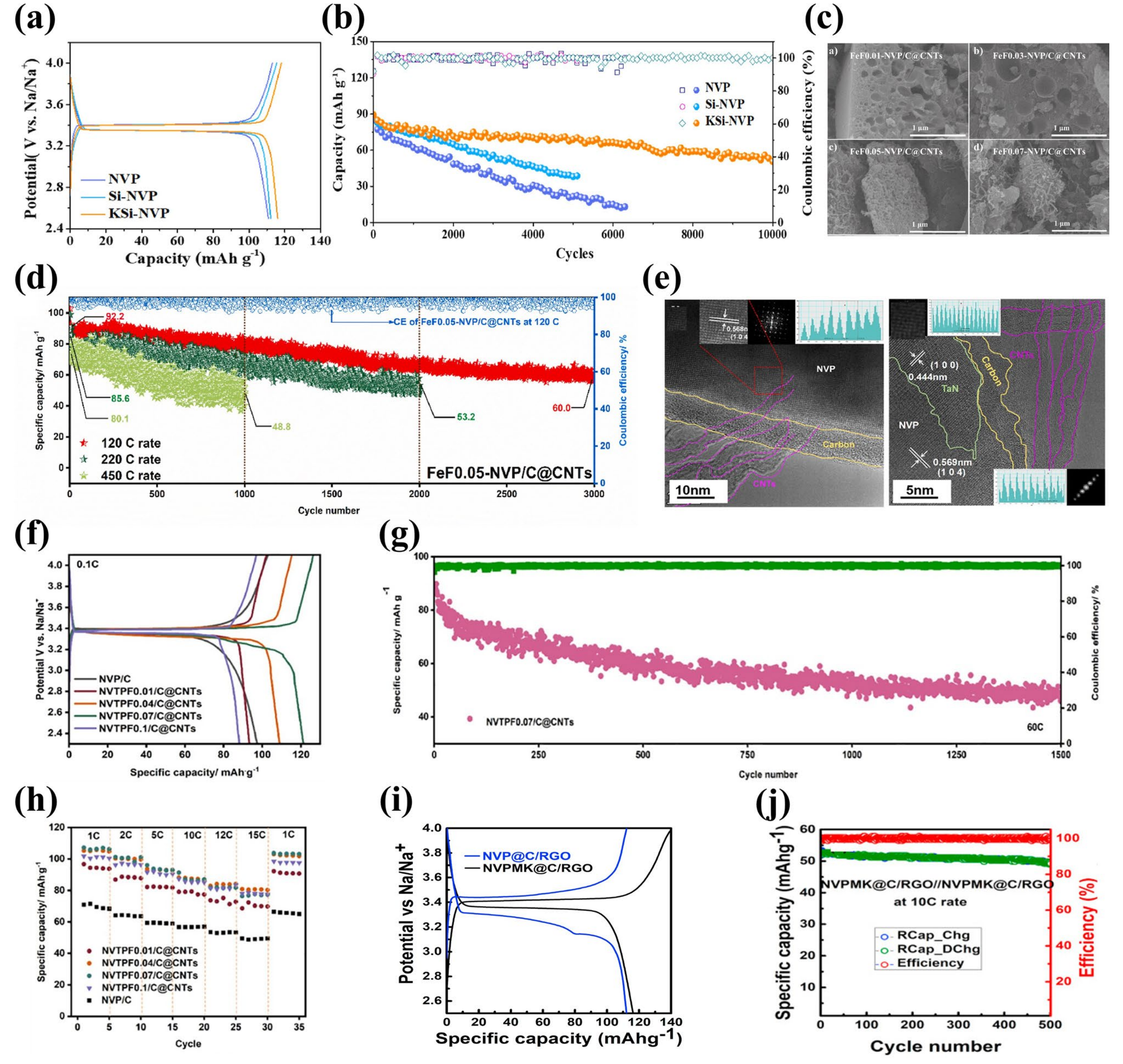

Fig. 15 **a** Charge–discharge curves at 0.5 C and **b** cycling performance at 20 C of NVP, Si-NVP and KSi-NVP. Reproduced with permission [197]. Copyright 2023, Elsevier. **c** SEM images of FeF0.01-NVP/C@CNTs, FeF0.03-NVP/C@CNTs, FeF0.05-NVP/C@CNTs and FeF0.07-NVP/C@CNTs composites, **d** cycling performance of FeF0.05-NVP/C@CNTs at 120, 220 and 450 C. Reproduced with permission [198]. Copyright 2021, Elsevier. **e** HRTEM images of NVTPF0.07/C@CNTs materials, **f** charge–discharge curves of different NVTPF/C@CNTs cathodes, **g** cycling performance of NVTPF0.07/C@CNTs at 60 C, **h** rate capability of different NVTPF/C@CNTs cathodes. Reproduced with permission [188]. Copyright 2024, Elsevier. **i** Charge–discharge curve at 1 C, **j** cycling performance at 10 C of NVPMK@C/RGO//NVPMK@C/RGO. Reproduced with permission [115]. Copyright 2020, Elsevier

substitution in NVP. Moreover, F^- and SiO_4^{4-} should be considered as the best anion doping in NVP due to the strong electronegative or identical ion structure with PO_4^{3-}. The doping or substitution in different sites exhibits various effectiveness for enhancing the sodium storage performance of NVP cathode material. Notably, the replacement of V site has been regarded as a more effective approach to boost the properties of NVP material compared with the doping or substitution in Na and PO_4^{3-} sites, which includes isovalent-ion substitution, aliovalent-ion substitution and multiple-ions substitution, presenting different potentialities for optimizing the electrochemical performance of NVP material. Moreover, it is the multiple-ions doping or substitution in V site that can incorporate the respective advantages of every metal ion and achieve excellent electrochemical performance of NVP material. In addition, multi-sites doping or substitution, combining with the independent benefits of different doping sites, is also proven to be an effective strategy to enhance the electrochemical performance of NVP material. Table 2 compares the electrochemical performance of some foreign-ion doped NVP cathode materials introduced previously.

3.3 Nanostructure and Morphology Design

Different dimensional structures with unique morphologies of NVP cathode materials have been constructed and demonstrated as an effective way to enhance their rate capability and cycle stability [199–201]. Based on various kinds of preparation methods and nanotechnologies, three types of dimensional structures with notable morphologies can be designed for the NVP materials, such as 1D nanofibers/nanowires, 2D nanoflake/nanosheet/nanoplate and 3D nanosphere/hierarchical porous/hollow structures. The nano-designing endows NVP with many advantages. Firstly, the unique morphologies with larger specific surface area can promote electrolyte penetration and boost electrons transportation. Secondly, the nanostructure shortens Na^+ ions diffusion distance and elevates ionic conductivity. Lastly, the nano-construction of NVP materials generates additional voids and cavities for the great alleviation of cell volume change and thus stabilizes the crystal structural of NVP. The electrochemical performance of some reported NVP cathode materials with different structures and morphologies is listed in Table 3.

Electrospinning method, as a facile and environmental friendliness technique, is popularly employed to obtain 1D nanofiber materials with good properties. Wu et al. [200] synthesized $Na_3V_2(PO_4)_3$/C (NVP/C) nanofibers with smooth and uniform surface morphologies through electrospinning method with choosing oxalic acid as reductant, complexing agent and carbon source. As shown in Fig. 16a, the optimized 1D NVP/C nanofibers, which were characterized by homogenous and smooth surface and mean diameter of approximately 400 nm without any protrusions, could be witnessed. As a result, the modified NVP/C nanofibers cathode showed a good discharge capacity of 113 mAh g^{-1} at 0.1 C and better rate performance (Fig. 16b). Liu et al. [201] designed cross-welded $Na_3V_2(PO_4)_3$/C nanofibrous mats (NVP/C-NM) via electrospinning route, which selected ionic liquid as phosphoric acid source and carbon source to make sure the spinnability in the PAN-based electrospinning system and form a compact and continuous carbon layer. The NVP/C-NM served as a current collector and had a helpful impact on enlarging contact area between electrode and electrolyte, resulting in higher electrochemical performance compared with NVP/C nanofibers and NVP/C nanoparticles. As displayed in Fig. 16c, d, the NVP/C-NM cathode presented impressive rate capability and stable cycling performance. Besides, the structure and morphology of NVP nanomaterials can be regulated by introducing a template as guide, such as N-dimethylformamide (DMF), cetyltrimethylammonium bromide (CTAB), polyethylene glycol (PEG) and metal–organic frameworks (MOFs), which can obtain different nano-dimensional NVP materials [87, 202]. Mai's group [203] proposed a simple self-sacrificed template method and successfully synthesized 1D NVP nanofibers (NVP-F). By adding DMF and controlling reaction time (from 0.5 to 20 h), the resultant 1D NVP nanofibers with diameters of 20–80 nm and length of about millimeters were observed, which evolved from microsphere to 3D nanofiber network (Fig. 16e). Importantly, it was 3D nanofiber network that generated more gaps for providing more Na^+ ion-transport channels and enlarged specific surface area for sufficient penetration of electrolyte. Consequently, the NVP-F harvested superior cycling stability, sustaining 95.9% capacity over 1000 cycles at 10 C, together with excellent high-rate performance (94 mAh g^{-1} at 100 C) (Fig. 16f, g).

The 2D NVP nanoplates (NVP/C-P) with abundant pores effectively shortened Na^+ ions diffusion paths and enlarged specific surface area (Fig. 16h) [204]. Compared to the bare NVP and NVP/C particles, the NVP/C-P cathode material delivered a higher discharge capacity of 117 mAh g^{-1} at 0.2 C, and exhibited superior rate capability (87.3 mAh g^{-1} specific capacity at 50 C) (Fig. 16i) and outstanding cycling stability (82.6% capacity retention at 50 C over 10,000 cycles). Guo et al. [205] skillfully synthesized 2D $Na_3V_2(PO_4)_3$ (NVP) nanoflakes with plane dimensional sizes of 100 to 150 nm, drawing support from the soft template of ethylene glycol (EG). The NVP nanoflakes could promote crystal nucleation and subsequently transform into super electronic network in the heat treatment. As depicted

https://doi.org/10.1007/s40820-024-01526-x

Table 2 Comparison of electrochemical performance of some reported foreign-ion doped NVP cathode materials

Site	Cathode material	Doping ion	Voltage range (V)	Discharge capacity (mAh g^{-1})/Rate	Capacity retention/Cycles/Rate	Refs
Na	$Na_{2.9}K_{0.1}V_2(PO_4)_3/C$	K^+	2.5–3.8	107.7, 0.2 C	95%, 300, 0.2 C	[67]
	$Na_{2.95}K_{0.05}V_2(PO_4)_3$	K^+	2.5–3.8	100.1, 0.5 C	80%, 1000, 10 C	[117]
	$Na_{2.8}Li_{0.2}V_2(PO_4)_3/C$	Li^+	2.5–3.8	116.9, 0.2 C	99.82%, 500, 0.2 C	[118]
	$Na_{2.8}Ca_{0.1}V_2(PO_4)_3@C\text{-}gC_3N_4$	Ca^{2+}	2.3–3.9	106.4, 0.1 C	93.6%, 3000, 10 C	[121]
V	$Na_3V_{1.5}Cr_{0.5}(PO_4)_3$	Cr^{3+}	1.0–4.4	150, 30 mA g^{-1}	96%, 400, 30 mA g^{-1}	[132]
	$Na_3V_{1.5}Cr_{0.5}(PO_4)_3$	Cr^{3+}	1.0–4.2	163.2, 0.1 C	87.5%, 1000, 1 C	[124]
	$Na_3Cr_{4/3}V_{3/2}(PO_4)_3@C$	Cr^{3+}	1.5–4.4	175, 100 mA g^{-1}	83%, 2000, 100 mA g^{-1}	[136]
	$Na_3Cr_{0.5}V_{1.5}(PO_4)_3$ /C@rGO	Cr^{3+}	1.0–4.4	176, 0.2 C	80.49%, 100, 0.2 C	[134]
	$Na_3V_{1.6}Cr_{0.4}(PO_4)_3$	Cr^{3+}	2.5–4.1	115, 0.1 C	95%, 100, 0.1 C	[135]
	$Na_3V_{1.98}Al_{0.02}(PO_4)_3/C$	Al^{3+}	2.3–3.8	102.7, 10 mA g^{-1}	99.2%, 50, 10 mA g^{-1}	[47]
	$Na_3V_{1.5}Al_{0.5}(PO_4)_3$	Al^{3+}	1.0–4.4	165, 0.1 C	87.9%, 500, 5 C	[142]
	$Na_3V_{1.25}Ga_{0.75}(PO_4)_3$	Ga^{3+}	1.4–4.2	152.3, 1 C	84.52%, 600, 10 C	[61]
	$Na_3V_{1.25}Ga_{0.75}(PO_4)_3$	Ga^{3+}	2.2–4.2	105, 1 C	92.3%, 400, 1 C	[61]
	$Na_3V1_{.5}Mn_{0.5}(PO_4)_3$	Mn^{3+}	1.0–4.0	170.9, 0.5 C	/	[129]
	$Na_3V_{1.5}Fe_{0.5}(PO_4)_3$	Fe^{3+}	1.0–4.5	166.4, 1 C	80.41%, 50, 1 C	[143]
	$Na_3Fe_{0.8}V_{1.2}(PO_4)_3/C$	Fe^{3+}	1.5–4.5	115.2, 0.5 C	97.8%, 500, 5 C	[62]
	$Na_3V_{1.85}Fe_{0.15}(PO_4)_3@C$	Fe^{3+}	2.3–4.3	103.9, 1 C	91.45%, 1200, 1 C	[131]
	$Na_3V_{1.96}Ru_{0.04}(PO_4)_3/C@CNTs$	Ru^{3+}	2.3–4.1	112.7, 1 C	86.63%, 14,800, 80 C	[73]
	$Na_3V_{1.97}Bi_{0.03}(PO_4)_3/C@CNTs$	Bi^{3+}	2.3–4.1	112.6, 0.1 C	82.41%, 9000, 12 C	[88]
	$Na_3V_{1.93}Y_{0.07}(PO_4)_3$	Y^{3+}	2.3–4.1	125.2, 0.1 C	85.5%, 2000, 250 C	[145]
	$Na_3V_{1.8}Mn_{0.2}(PO_4)_3/C$	Mn^{2+}	2.5–4.0	106.8, 1 C	82%, 10,000, 30 C	[149]
	$Na_{3.75}V_{1.25}Mn_{0.75}(PO_4)_3$	Mn^{2+}	2.5–4.1	100, 1 C	96%, 100, 5 C	[151]
	$Na_{3.5}Mn_{0.5}V_{1.5}(PO_4)_3$	Mn^{2+}	2.5–4.1	108.3, 2 C	87.2%, 4000, 20 C	[152]
	$Na_3V_{5.92/3}Mn_{0.04}(PO_4)_3/C@CNTs@1wt\%Al_2O_3$	Mn^{2+}	2.3–4.1	115.9, 1 C	84.87%, 6000, 30 C	[99]
	$Na_{3.5}Mn_{0.5}V_{1.5}(PO_4)_3$ @GO	Mn^{2+}	2.5–4.2	112, 2 C	81.3%, 400, 2 C	[147]
	$Na_{3.4}V_{1.6}Fe_{0.4}(PO_4)_3$	Fe^{2+}	2.5–4.1	133, 0.5 C	96%, 2000, 20 C	[158]
	$Na_{3.5}V_{1.5}Fe_{0.5}(PO_4)_3$	Fe^{2+}	1.7–4.3 2.0–3.8	148.2, 0.5 C 112, 0.5 C	72%, 500, 5 C 92%, 1000, 5 C	[160]
	$Na_{3.01}V_{1.99}Co_{0.01}(PO_4)_3/C$	Co^{2+}	2.5–4.0	116, 0.5 C	83.2%, 1000, 10 C	[161]
	$Na_{3.03}V_{1.97}Cu_{0.03}(PO_4)_3/C$	Cu^{2+}	2.5–4.0	114, 0.5 C	93.1%, 1000, 10 C	[161]
	$Na_3V_{1.93}Co_{0.07}(PO_4)_3/C$	Co^{2+}	2.3–4.1	114.4, 0.1 C	80.51%, 1000, 10 C	[162]
	$Na_3V_{1.95}Ca_{0.05}(PO_4)_3/C$	Ca^{2+}	2.0–3.9	111.4, 1 C	90.4%, 300, 1 C	[163]
	$Na_3V_{1.97}Ni_{0.03}(PO_4)_3/C$	Ni^{2+}	2.0–3.8	108.2, 1 C	93.5%, 50, 5 C	[165]
	$Na_3V_{1.95}Mg_{0.05}(PO_4)_3/C$	Mg^{2+}	2.5–4.0	112.5, 1 C	81%, 50, 20 C	[166]
	$Na_{3.04}V_{1.96}Mg_{0.04}\ (PO_4)_3/C$	Mg^{2+}	2.5–4.2	123.8, 1 C	89.1%, 3000, 20 C	[60]
	$Na_3V_{1.95}Ca_{0.05}(PO_4)_3@C$	Ca^{2+}	2.0–4.3	116, 1 C	93%, 1000, 1 C	[170]
	$Na_3V_{1.965}Ca_{0.04}(PO_4)_3@C$ @CNTs	Ca^{2+}	2.3–4.1	117.4, 0.1 C	95%, 4000, 50 C	[171]
	$Na_3V_{1.9}Ti_{0.1}(PO_4)_3/C$	Ti^{4+}	2.0–4.2	123.3, 0.1 C	62.3%, 8000, 20 C	[174]
	$Na_{2.85}V_{1.85}Ti_{0.15}(PO_4)_3$	Ti^{4+}	2.3–3.9	101.5, 2 C	60%, 2000, 10 C	[175]
	$Na_{2.9}V_{1.98}Mo_{0.02}(PO_4)_3$	Mo^{6+}	2.2–3.8	112.5, 0.5 C	83.5%, 500, 10 C	[176]
	$Na_3Fe_{0.8}VNi_{0.2}(PO_4)_3$	Fe^{2+}, Ni^{2+}	2.0–3.8	102, 0.1 C	84.6, 1400, 20 C	[140]
	$Na_3V_{1.5}Cr_{0.4}Fe_{0.1}(PO_4)_3$	Fe^{2+}, Cr^{3+}	2.5–4.3	114.7, 0.1 C	90%, 10,000, 30 C	[110]
	$Na_4FeV_{1/3}Ti_{2/3}(PO_4)_3$	Fe^{2+}, Ti^{3+}	1.3–4.3	125.83, 0.1 C	92.8%, 500, 0.5 C	[177]
	$Na_{3.75}V_{1.25}Mn_{0.5}Ni_{0.25}(PO_4)_3$	Mn^{2+}, Ni^{2+}	2.0–4.0	108.1, 0.2 C	85.8%, 1000, 5 C	[111]
	$Na_{3.2}Mn\ Ti_{0.8}\ V_{0.2}\ (PO_4)_3$	Mn^{2+}, Ti^{4+}	1.5–4.4	172.5, 50 mA g^{-1}	84.1%, 100, 100 mA g^{-1}	[125]
	$Na_{3.2}V_{2.7}(FeMnCo)_{0.1}(PO_4)_3$	Fe^{3+}, Mn^{2+}, Co^{2+}	2.3–4.1 2.0–4.5	122.2, 0.1 C 166.3, 1 C	88.1%, 800, 1 C 80.1%, 800, 1 C	[113]
	$Na_{3.5}Fe_{0.5}V_{0.5}Cr_{0.5}Ti_{0.5}(PO_4)_3$	Fe^{2+}, Cr^{3+}, Ti^{3+}	1.5–4.5	178.3, 0.1 C	69.48%, 5000, 5 C	[126]
	$Na_3VAl_{0.2}Cr_{0.2}Fe_{0.2}In_{0.2}Ga_{0.2}(PO_4)_3$	Al^{3+}, Cr^{3+}, Fe^{3+}, In^{3+}, Ga^{3+}	2.5–4.4	102, 0.1 C	86.8%, 5000, 20 C	[180]

Table 2 (continued)

Site	Cathode material	Doping ion	Voltage range (V)	Discharge capacity (mAh g^{-1})/Rate	Capacity retention/Cycles/Rate	Refs
	$Na_{3.32}V_{1.6}Cr_{0.08}Fe_{0.08}Mn_{0.08}Mg_{0.08}Ca_{0.08}(PO_4)_3$	Cr^{3+}, Fe^{2+}, Mn^{2+}, Mg^{2+}, Ca^{2+},	1.2–4.2	120, 5.0 A g^{-1}	93.1%, 2000, 5.0 A g^{-1}	[181]
	$Na_{3.4}Fe_{0.4}Mn_{0.4}V_{0.4}Cr_{0.4}Ti_{0.4}(PO_4)_3$	Fe^{2+}, Mn^{2+}, Cr^{3+}, Ti^{3+}	1.5–4.5	161.3, 0.1 C	85.3%, 1000, 5 C	[182]
$PO_4{}^{3-}$	$Na_3V_2(PO_4)_{1.93}F_{0.0}/C$	F^-	2.3–4.2	113, 10 mA g^{-1}	86%, 1000, 200 mA g^{-1}	[191]
	$Na_3V_{1.98}(PO_4)_{2.9}F_{0.3}/C$	F^-	2.3–4.2	116.9, 0.1 C	89.3%, 100, 1 C	[192]
	$Na_3V_2(PO_4)_{3-1/6}(BO_3)_{1/6}$	$BO_3{}^{3-}$	2.5–4.0	105, 1 C	98.7%, 300, 5 C	[185]
	$Na_{3.1}V_2(PO_4)_{2.9}(SiO_4)_{0.1}$	$SiO_4{}^{2-}$	2.3–3.9	109.4, 0.2 C	98%, 500, 1 C	[183]
	$Na_{3.1}V_2(PO_4)_{2.9}(SiO_4)_{0.1}/C@rGO$	$SiO_4{}^{2-}$	2.3–4.1	113.6, 0.1 C	76.7%, 2000, 6 C	[195]
	$Na_{3.2}V_2(PO_4)_{2.9}(MoO_4)_{0.1}$	$MoO_4{}^{2-}$	2.4–4.3	108.9, 1 C	91.5%, 150, 1 C	[187]
Multiple-site	$Na_{3.24}K_{0.10}V_{2.01}(PO_4)_3(SiO_4)_{0.14}$	K^+, $SiO_4{}^{2-}$	2.3–4.1	116.3, 0.5 C	44%, 10,000, 20 C	[197]
	$Na_3V_{1.95}Fe_{0.05}(PO_4)_{2.95}F_{0.15}/C@CNTs$	Fe^{3+}, F^-	2.3–4.1	111.1, 0.1 C	65.1%, 3000, 120 C	[198]
	$Na_3V_{1.95}Ta_{0.05}(PO_4)_{1.93}F_{0.21}/C@CNTs$	Ta^{5+}, F^-	2.3–4.1	121.5, 0.1 C	63.49%, 1500, 60 C	[188]
	$Na_{2.91}K_{0.09}V_{2.93}Mg_{0.07}(PO_4)_3@C/rGO$	K^+, Mg^{2+}	2.5–4.0	116.6, 1 C	/	[115]

Table 3 Electrochemical performance of some reported NVP cathode materials with different dimensional nanostructures and morphologies

Cathode material	Method	Structure/Morphology	Discharge capacity (mAh g^{-1})/Rate	Capacity retention/Cycles/Rate	Refs
$Na_3V_2(PO_4)_3/C$	Electrospinning	Nanofibers	113, 0.1 C	97%, 100, 0.05 C	[200]
$Na_3V_2(PO_4)_3/C$	Ionic liquid (IL)-assisted electrospinning	Nanofibrous mats	117.4, 0.1 C	89.07%, 400, 1 C	[201]
$Na_3V_2(PO_4)_3/C$	Self-sacrificed template method	Nanofibers	113, 1 C	95.9%,1000, 10 C	[203]
$Na_3V_2(PO_4)_3/C$	Hydrothermal and post calcination	Nanoplates	117, 0.2 C	82.6%, 10,000, 50 C	[204]
$Na_3V_2(PO_4)_3/C$	Soft-template	Nanoflakes	115.4, 0.5 C	78.5%, 50,000, 100 C	[205]
$Na_3V_2(PO_4)_3/C$	Microwave-assisted hydrothermal	Nanosheets	116.6, 0.2 C	78.31%, 1000, 100 C	[206]
$Na_3V_2(PO_4)_3/C$	Hydrothermal	Hierarchical porous microspheres	116.3, 0.5 C	91.9%, 1000, 5 C	[208]
$Na_3V_2(PO_4)_3/C$	Solvothermal	Core–shell micellar structure	115.2, 1 C	79.53%, 1000, 10 C	[202]
$Na_3V_2(PO_4)_3/C$	MOFs assisted sol–gel	Hierarchical porous micro-nano particles	110.4, 0.5 C	97.8%, 500, 1 C	[210]
$Na_3V_2(PO_4)_3/C$	Spray-drying	Micro-nano spherical	106, 2 C	50%, 5000, 50 C	[211]

in Fig. 16j, the NVP nanoflakes were homogeneously dispersed in the electronic network and effectively mitigated the restacking problem of 2D nanoflakes. Meantime, the existence of massive interstitial voids between nanoplates elevated rapid charge transfer across the electrode/electrolyte interface. The NVP nanoflakes exhibited ultrahigh-rate performance with about 71.2 and 56.2 mAh g^{-1} discharge capacities at 200 and 300 C, respectively (Fig. 16k). Astonishingly, the optimized NVP yielded a high initial specific capacity of 84.1 mAh g^{-1} at 100 C with 78.5% capacity retention after 50,000 cycles (Fig. 16l).

However, the low-dimensional structures of nanomaterials (nanofibers, nanoplates and nanoflakes) are prone to agglomerate during the high-temperature treatment and repetitive charging/discharging processes, resulting in the loss of active materials and inferior sodium storage performance [206]. To deal with this issue, some researches ingeniously employed low-dimensional nanomaterials to construct 3D

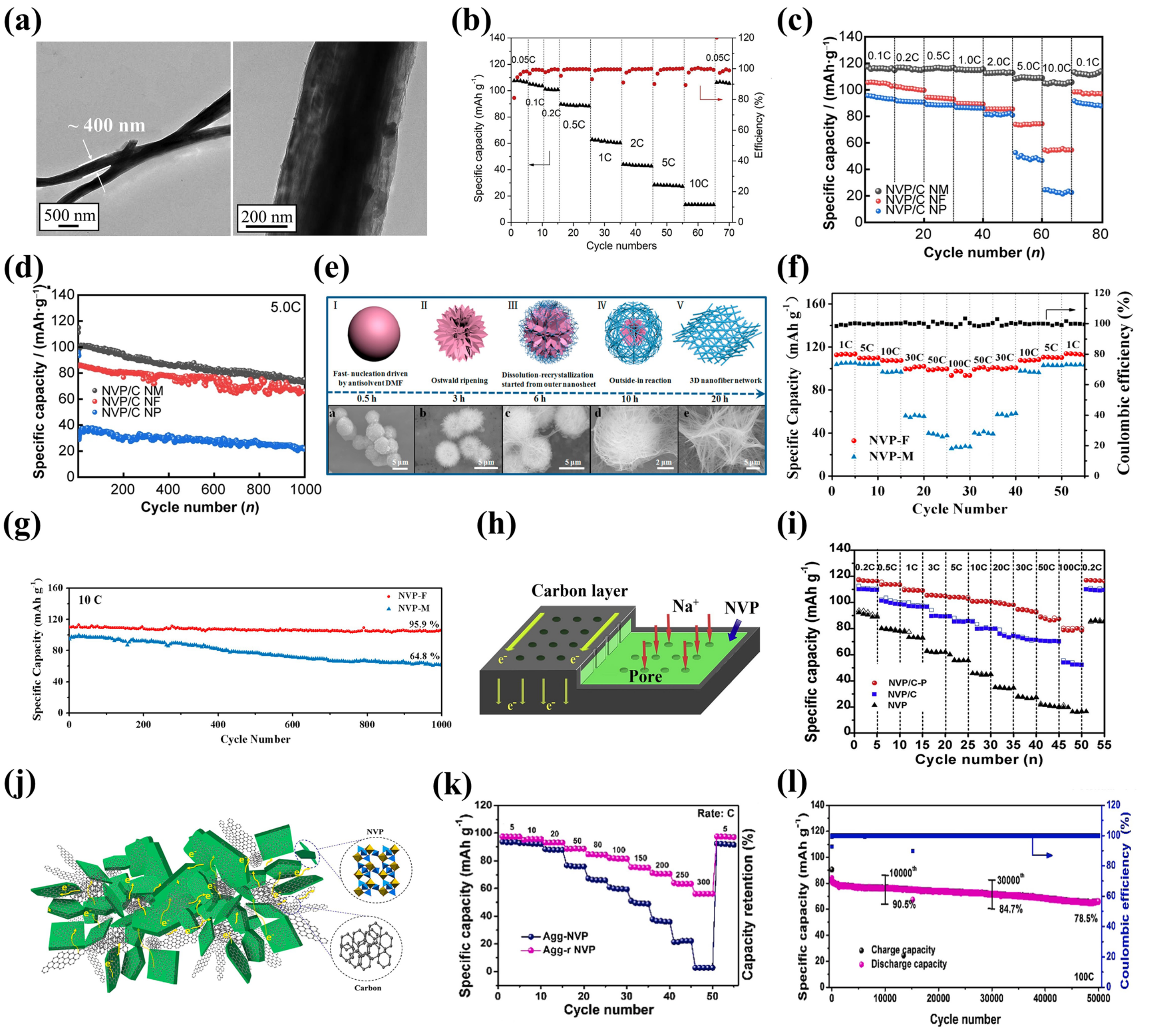

Fig. 16 **a** TEM images of $Na_3V_2(PO_4)_3/C$ sample with oxalic acid, **b** rate performances of $Na_3V_2(PO_4)_3/C$ sample with oxalic acid. Reproduced with permission [200]. Copyright 2018, Elsevier. **c** Rate capability of NVP/C-NM and **d** cycling performance at 5.0 C of NVP/C-NM, NVP/C NF and NVP/C NP. Reproduced with permission [201]. Copyright 2021, Youke Publishing. **e** Schematic illustrations of the time-dependent solvothermal reaction: self-sacrificed evolution mechanism from microsphere to nanofiber network, **f** rate capability and **g** cycling performance of NVP-F and NVP-M electrodes. Reproduced with permission [203]. Copyright 2016, Elsevier. **h** Schematic illustration of constructions of NVP/C-P, **i** rate capability of NVP, NVP/C and NVP/C-P. Reproduced with permission [204]. Copyright 2018, Elsevier. **j** Schematic diagram of Agg-r NVP nanoflakes, **k** rate capability of Agg-NVP and Agg-r NVP, **l** cycling performance of Agg-r NVP electrode at 100 C. Reproduced with permission [205]. Copyright 2018, Elsevier

hierarchical porous architectures, which could not only significantly suppress the agglomeration of NVP nanomaterials but also further reduce the transmission distance of Na^+ ions and electrons [207–209]. Cao et al. [208] used a hydrothermal method to synthesize 3D $Na_3V_2(PO_4)_3/C$ hierarchical microspheres (NVP-MSs) assembled from loosely interconnected 2D nanoflakes, which had the thickness of about 20–30 nm and existed distinct open space between them (Fig. 17a). As shown in Fig. 17b, the morphological evolution of NVP hierarchical microspheres could be controlled

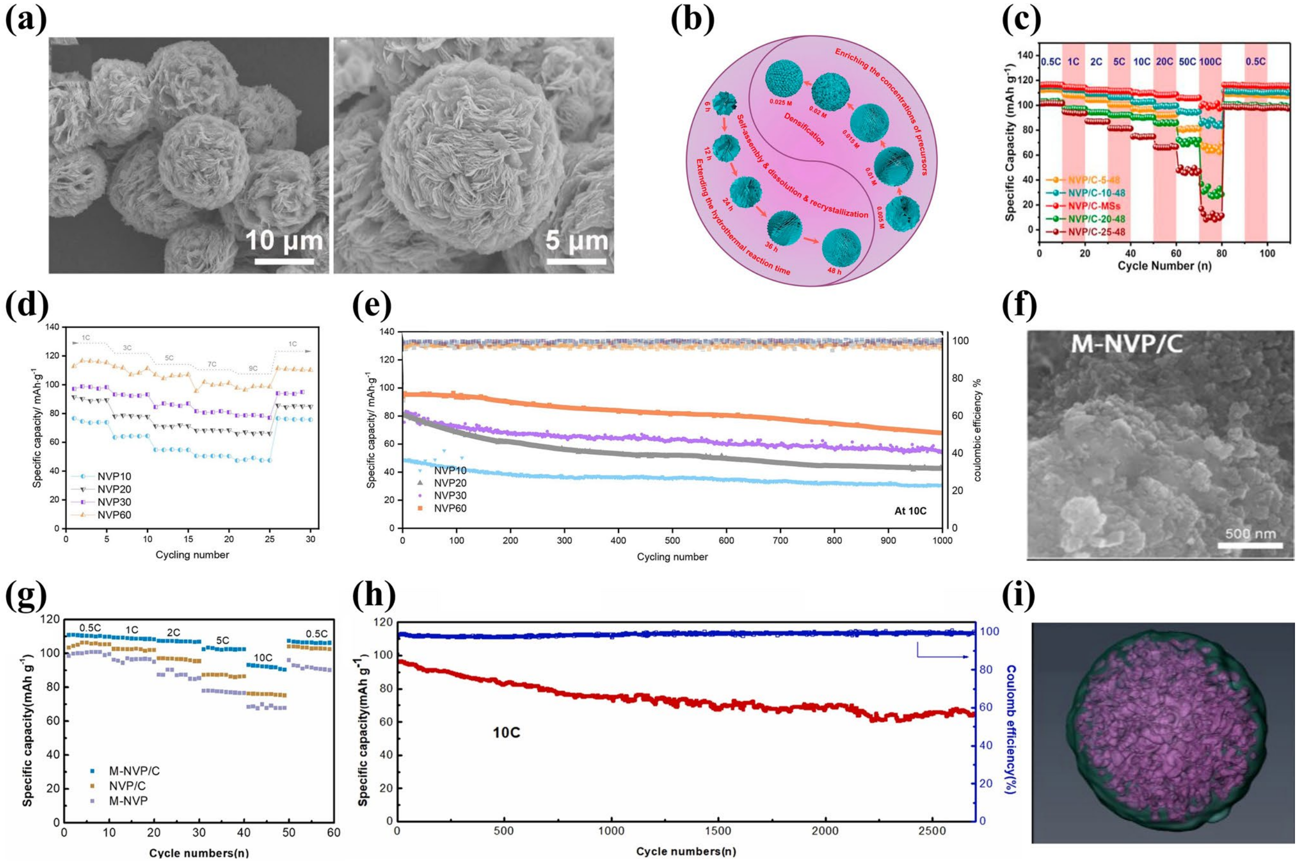

Fig. 17 **a** SEM images of NVP/C-MSs, **b** schematic illustration of formation process for hierarchical microspheres, **c** rate capability of different NVP/C microspheres. Reproduced with permission [208]. Copyright 2019, Elsevier. **d** Rate performance and **e** cycling performance of NVP cathodes synthesized at different conditions. Reproduced with permission [202]. Copyright 2022, Elsevier. **f** SEM image of M-NVP/C sample, **g** rate capability of M-NVP, NVP/C and M-NVP/C samples, **h** cycling performance of M-NVP/C at 10C. Reproduced with permission [210]. Copyright 2022, Elsevier. **i** 3D model of NVP particle. Reproduced with permission [211]. Copyright 2019, Elsevier

by tuning the precursor concentration and hydrothermal reaction time. The optimized NVP-MSs exhibited a nearly theoretical capacity of 116.3 mAh g^{-1} at 0.5 C, as well as a desirable discharge capacity of 99.3 mAh g^{-1} at 100 C (Fig. 17c).

Furthermore, some novel optimization strategies for constructing 3D structures with unique shapes of NVP are proposed, without the help of low-dimensional nanomaterials [202, 210]. Sun et al. [202] constructed 3D crosslinked core–shell micellar structures and prepared nanoflowers-shaped NVP/C materials combined with negative flake V_2O_5 by adding structural guiding agent PEG and surfactant CTAB in the 100% methyl alcohol solvent system. Specifically, the PEG and CTAB played an effective synergistic effect on the formation of the unique nanoflower-shaped NVP (positive charge). Meanwhile, the low polarity methanol protected the nanoflowers from breaking original morphologies. On accountant of the charge attraction, the negative platelike V_2O_5 was compactly absorbed on the surface of NVP, contributing to more active sites for NVP materials. Benefiting from these merits, the optimized NVP cathode obtained outstanding rate performance and cyclic stability, delivering a reversibility capacity of 115.2 mAh g^{-1} at 1 C and 98.7 mAh g^{-1} at 10 C after 1000 cycles (Fig. 17d, e).

In addition, Chen et al. [210] prepared micro-nano NVP/C materials (M-NVP/C) with micro-size hierarchical porous structure and nano particles (Fig. 17f), derived from MOFs precursors. MOFs materials acting as a guider had a positive effect to construct hierarchical porous structure, which possessed high specific surface area to allow ample infiltration of electrolyte and effectively restricted agglomeration of nanoparticles. As displayed in Fig. 17g, h, the M-NVP/V submitted a remarkable discharge capacity of 95.0 mAh g^{-1} at 10 C and 67.7% capacity retention after 2700 cycles at 10 C. Moreover, Yang et al. [211] also developed 3D micro-nano spherical structure NVP/C materials (Fig. 17i) composed of micro spherical particles and internal nano channels via spray-drying method. The as-prepared NVP/C with micro-size displayed competitive rate capability with 106, 104, 101, 96, 89, 70 and 44 mAh g^{-1} discharge capacities at 2, 5, 10, 20, 50, 100 and 200 C, respectively, compared to the nano sized NVP/C with 106, 103, 85, 77 and 60 mAh g^{-1} discharge capacities at 2, 5, 10, 20 and 50 C, respectively.

Generally, the optimal design of structures and morphologies of NVP nanomaterials plays a significant role to optimize the electrochemical performance of NVP cathode materials. Nevertheless, there remain some challenges. Firstly, it is the high specific surface area that is frequently produced through high carbon contents, reducing the volume energy density. Besides, nanoparticles are easily agglomerating and taking side reactions during the high-temperature sintering process and subsequent electrochemical cycles, which limit the utilization of active materials and cause unsatisfactory electrochemical properties. Conversely, the nanomaterials, in the low temperature, obtain inferior crystallinity and impurity phases, which influence the further research. Thirdly, the synthesis routes of NVP nanomaterials are usually complex and adverse to achieve large-scale applications in SIBs.

4 Summary and Outlook

As a promising cathode material for SIBs, $Na_3V_2(PO_4)_3$ (NVP) has been a research hotpot in terms of its robust structure with sufficient ion-diffusion channels and good thermal stability. Nevertheless, NVP remains challenging for the achievement of high capacity and satisfactory energy density because of its poor electronic conductivity and sluggish diffusion kinetics. Currently, significant endeavors to optimize NVP cathode material have been witnessed. Many optimization strategies have been proposed to optimize the electrochemical performance of NVP cathode material. In this review, we have completely summarized and discussed the latest advances in the optimization strategies of NVP cathode material, including carbon coating or modification, foreign-ion doping or substitution and nanostructure and morphology design. The carbon coating or modification, such as coating carbon layer on the surface of NVP or preparing NVP/carbon composite, is a preferred strategy to boost electronic conductivity and suppress the adverse agglomeration of NVP particles. The foreign-ion substitution or doping into NVP, occurring in the Na, V and PO_4^{3-} sites, has become a primary research trend to intrinsically improve its electrical conductivity. The doping or substitution includes single-site doping and multiple-site doping, and for single-site doping, there are single-ion doping and multiple-ion doping. The doping or substitution in V site is very effective for enhancing the sodium storage performance of NVP. It is of constructive significance to rationally design nanostructure with specific morphology comprising 1D, 2D or 3D architectures, which enable NVP with fast Na ion-diffusion kinetics and substantial interfacial contact with electrolyte. Based on these optimization strategies, the electrochemical performance of NVP cathode has been greatly improved, such as its reversible capacity, rate capability and cycling stability.

However, every optimization approach still has some weaknesses. Although carbon materials loaded on NVP can increase electronic conductivity efficiently, most of carbon coating and composing with high carbon content may slow down the transfer of electrons and ions and impair the capacity of NVP. The alien ions introduced into NVP will inevitably give rise to crystal distortion and thus lead to unsatisfactory cycling stability in view of the lattice compatibility. In addition, complex preparation and technologies of nanostructured NVP are hardly to meet with the large-scale and low-cost commercial requirements for the practical applications. Meantime, nanosized NVP particles easily agglomerate and therefore decrease the availability of NVP cathode materials. Accordingly, aiming at the high-performance NVP cathode materials in the field of commercialization for SIBs, to further develop new optimization strategies is imperative. Herein, we propose some considerations and perspectives for the further explorations in designing and developing high-performance NVP cathode materials for practical application in SIBs.

4.1 Optimizing Carbon Coating/Modification

Carbon-based materials have a great influence on the electrochemical performance of carbon-modified NVP cathodes. Selecting suitable carbon source is very important for improving performance and reducing cost. The biomass-derived carbon featuring low-cost, adjustable structure and various heteroatom doping can be a suitable alternative as carbon source to optimize NVP materials. Besides, constructing NVP@C@C 3D spatial structure with combining carbon composite and carbon coating can realize rapid transfer and diffusion of electrons and ions, which is helpful to improve rate capability and cycling performance. Moreover, low loading content and appropriate thickness of carbon layer coated on NVP are critical to efficiently boost electronic conductivity and improve electrochemical activity of NVP. New strategies should be developed to construct NVP/C composites with lower carbon loading content and appropriate thickness of carbon layer. The construction of carbon dot structure is worthy of concentration and necessary to be further investigated. The carbon dot incorporation strategy with trace carbon content can not only significantly boost the electronic conductivity but also elevate the electrochemical activity of NVP [96].

4.2 Integrating and Optimizing Multiple-Ion and Multi-Site Substitution

Foreign-ion doping or substitution is very effective for enhancing electrical conductivity and improving electrochemical performance of NVP cathodes. Most investigations of foreign-ion doping are mainly focused on the single-ion doping at V site. Multiple-ion and multi-site doping or substitution can well combine their own advantages to induce synergistic effect for further improving the electrochemical performance of NVP cathodes, which should be further investigated. These co-substitution strategies of different substitution elements functioned at different sites will be greatly beneficial for the enhancement of rate capability and long-term cyclic stability for NVP cathodes. Furthermore, the concept of high-entropy as a new insight has been employed to optimize the crystal structure of NVP cathode material for enhancing its electrochemical performance. The optimized mechanism and composition of high-entropy modified NVP needs to be explored in depth. In addition, considering the practical application, the V content in NVP need be reduced due to its high cost and toxicity. The low-cost, safe and earth-abundant elements, such as Mn, Fe and Ni, should be selected as transition metal elements for the substitution of V in NVP. The high throughput screening method should be considered for greatly facilitating the investigation to find new composition and structures.

4.3 Optimizing Nanostructure Construction

Nanoscale structure of NVP cathode material exerts positive impacts for narrowing the Na ion-migration pathways, enlarging electrode/electrolyte contact area and accelerating the transfer of ion. Constructing reasonable nanostructured NVP cathode material will contribute to high electrochemical performance. Much efforts need to be made to design and develop nanostructured NVP materials. Moreover, the nanostructure design should be combined with carbon coating or modification to construct 3D conducting network of NVP, which will help to increase specific capacity, enhance rate capability and improve cycling stability. However, the synthesis processes of NVP nanocomposites are generally complicated and time-consuming, which restricts their practical applications. Therefore, it is an essential thing to develop facile and efficient preparation route to construct nanostructured NVP cathode materials.

4.4 Choosing Suitable Electrolyte and Optimizing Cathode/Electrolyte Interface

Electrolyte is also an important component in battery, which affects the electrochemical performance of battery. Choosing suitable electrolyte will be beneficial to enhance the electrochemical performance of NVP cathode. The composition, including sodium salts, solvents and additives and concentration of electrolyte should be investigated for exploring their effects on the rate capability and cycling stability of NVP cathode. Besides, the electrode/electrolyte interface has also great influence on the electrochemical performance of NVP cathode. Constructing high-quality cathode/electrolyte interface can boost charge transfer kinetics and structural evolution of NVP cathode. Meantime, a compatible electrolyte can also promote the formation of a thin and uniform cathode/electrolyte interface. Therefore, the optimization of cathode/electrolyte interface plays a critical role to improve diffusion kinetics and increase electronic conductivity, which can reduce the efforts in different optimizing strategies to achieve high-performance NVP cathode material.

In summary, to achieve high-performance NVP cathode materials, focused efforts should be devoted to developing new optimization strategies. In addition, some proposed optimization strategies should be combined together to form synergistic effect for enhancing the electrochemical performance of NVP cathode materials. Though the commercialization of high-performance NVP cathode materials is a blocked and long road, with determined efforts, it will be finally achieved in the future.

Acknowledgements This work was partly supported by the National Natural Science Foundation of China (Grant No. 52272225).

Author Contributions Jiawen Hu performed investigation, visualization and writing—original draft. Xinwei Li presented formal analysis and visualization. Qianqian Liang, Li Xu and Yu Liu did formal analysis. Changsheng Ding conducted formal analysis, writing—review & editing and supervision. Yanfeng Gao revised writing—review & editing.

Declarations

Conflict of interest The authors declare no interest conflict. They have no known competing financial interests or personal relationships that could have appeared to influence the work reported in this paper.

References

1. T. Bashir, S. Zhou, S. Yang, S.A. Ismail, T. Ali et al., Progress in 3D-MXene electrodes for lithium/sodium/potassium/magnesium/zinc/aluminum-ion batteries. Electrochem. Energy Rev. **6**, 5 (2023). https://doi.org/10.1007/s41918-022-00174-2
2. K. Chayambuka, G. Mulder, D.L. Danilov, P.H.L. Notten, Sodium-ion battery materials and electrochemical properties reviewed. Adv. Energy Mater. **8**, 1800079 (2018). https://doi.org/10.1002/aenm.201800079
3. Z. Chen, A. Yildizbasi, Y. Wang, J. Sarkis, Safety in lithium-ion battery circularity activities: a framework and evaluation methodology. Resour. Conserv. Recycl. **193**, 106962 (2023). https://doi.org/10.1016/j.resconrec.2023.106962
4. M. Sarkar, R. Hossain, V. Sahajwalla, Sustainable recovery and resynthesis of electroactive materials from spent Li-ion batteries to ensure material sustainability. Resour. Conserv. Recycl. **200**, 107292 (2024). https://doi.org/10.1016/j.resconrec.2023.107292
5. L. Zhao, T. Zhang, W. Li, T. Li, L. Zhang et al., Engineering of sodium-ion batteries: opportunities and challenges. Engineering **24**, 172–183 (2023). https://doi.org/10.1016/j.eng.2021.08.032
6. S. Li, R. Dong, Y. Li, X. Lu, J. Qian et al., Advances in free-standing electrodes for sodium ion batteries. Mater. Today **72**, 207–234 (2024). https://doi.org/10.1016/j.mattod.2023.11.013
7. C. Matei Ghimbeu, A. Beda, B. Réty, H. El Marouazi, A. Vizintin et al., Review: insights on hard carbon materials for sodium-ion batteries (SIBs): synthesis–properties–performance relationships. Adv. Energy Mater. **14**, 2303833 (2024). https://doi.org/10.1002/aenm.202303833
8. C. Che, F. Wu, Y. Li, Y. Li, S. Li et al., Challenges and breakthroughs in enhancing temperature tolerance of sodium-ion batteries. Adv. Mater. **36**, e2402291 (2024). https://doi.org/10.1002/adma.202402291
9. H. Zhang, Y. Gao, X. Liu, L. Zhou, J. Li et al., Long-cycle-life cathode materials for sodium-ion batteries toward large-scale energy storage systems. Adv. Energy Mater. **13**, 2300149 (2023). https://doi.org/10.1002/aenm.202300149
10. Y. Zhao, Y. Kang, J. Wozny, J. Lu, H. Du et al., Recycling of sodium-ion batteries. Nat. Rev. Mater. **8**, 623–634 (2023). https://doi.org/10.1038/s41578-023-00574-w
11. X. Rui, X. Zhang, S. Xu, H. Tan, Y. Jiang et al., A low-temperature sodium-ion full battery: superb kinetics and cycling stability. Adv. Funct. Mater. **31**, 2009458 (2021). https://doi.org/10.1002/adfm.202009458
12. P.K. Nayak, L. Yang, W. Brehm, P. Adelhelm, From lithium-ion to sodium-ion batteries: advantages, challenges, and surprises. Angew. Chem. Int. Ed. **57**, 102–120 (2018). https://doi.org/10.1002/anie.201703772
13. P. Yadav, A. Patrike, K. Wasnik, V. Shelke, M. Shelke, Strategies and practical approaches for stable and high energy density sodium-ion battery: a step closer to commercialization. Mater. Today Sustain. **22**, 100385 (2023). https://doi.org/10.1016/j.mtsust.2023.100385
14. Y. Jiang, Z. Zhang, H. Liao, Y. Zheng, X. Fu et al., Progress and prospect of bimetallic oxides for sodium-ion batteries: synthesis, mechanism, and optimization strategy. ACS Nano **18**, 7796–7824 (2024). https://doi.org/10.1021/acsnano.4c00613
15. J. Lu, Z. Zhang, Y. Zheng, Y. Gao, In situ transmission electron microscopy for sodium-ion batteries. Adv. Mater. **35**, 2300359 (2023). https://doi.org/10.1002/adma.202300359

16. X. Zhang, Z. Zhang, S. Xu, C. Xu, X. Rui, Advanced vanadium oxides for sodium-ion batteries. Adv. Funct. Mater. **33**, 2306055 (2023). https://doi.org/10.1002/adfm.202306055
17. Z. Song, R. Liu, W.-D. Liu, Y. Chen, W. Hu, Low-cost polyanion-type cathode materials for sodium-ion battery. Adv. Energy Sustain. Res. **4**, 2300102 (2023). https://doi.org/10.1002/aesr.202300102
18. S. Qiao, Q. Zhou, M. Ma, H.K. Liu, S.X. Dou et al., Advanced anode materials for rechargeable sodium-ion batteries. ACS Nano **17**, 11220–11252 (2023). https://doi.org/10.1021/acsnano.3c02892
19. J. Wu, G. Wang, W. Zhang, L. Wang, J. Peng et al., Universal architecture and defect engineering dual strategy for hierarchical antimony phosphate composite toward fast and durable sodium storage. J. Energy Chem. **90**, 110–119 (2024). https://doi.org/10.1016/j.jechem.2023.11.013
20. Q. Li, W. Zhang, J. Peng, D. Yu, Z. Liang et al., Nanodot-in-nanofiber structured carbon-confined Sb_2Se_3 crystallites for fast and durable sodium storage. Adv. Funct. Mater. **32**, 2112776 (2022). https://doi.org/10.1002/adfm.202112776
21. Q. Liu, Z. Hu, M. Chen, C. Zou, H. Jin et al., Recent progress of layered transition metal oxide cathodes for sodium-ion batteries. Small **15**, 1805381 (2019). https://doi.org/10.1002/smll.201805381
22. J. Park, Y. Jeong, H. Kang, T.-Y. Yu, X. Xu et al., A dual-functional electrolyte additive for high-performance potassium metal batteries. Adv. Funct. Mater. **33**, 2304069 (2023). https://doi.org/10.1002/adfm.202304069
23. Y. Gao, X. Wu, L. Wang, Y. Zhu, G. Sun et al., Structurally stable, low H_2O Prussian blue analogs toward high performance sodium storage. Adv. Funct. Mater. **34**, 2314860 (2024). https://doi.org/10.1002/adfm.202314860
24. W. Shu, J. Li, G. Zhang, J. Meng, X. Wang et al., Progress on transition metal ions dissolution suppression strategies in prussian blue analogs for aqueous sodium-/potassium-ion batteries. Nano-Micro Lett. **16**, 128 (2024). https://doi.org/10.1007/s40820-024-01355-y
25. M. Baumann, M. Häringer, M. Schmidt, L. Schneider, J.F. Peters et al., Prospective sustainability screening of sodium-ion battery cathode materials. Adv. Energy Mater. **12**, 2202636 (2022). https://doi.org/10.1002/aenm.202202636
26. X. Tu, Y. Liu, K. Wang, Z. Ding, X. Xu et al., Ternary-metal Prussian blue analogues as high-quality sodium ion capturing electrodes for rocking-chair capacitive deionization. J. Colloid Interface Sci. **642**, 680–690 (2023). https://doi.org/10.1016/j.jcis.2023.04.007
27. K. Lin, Q. Liu, Y. Zhou, H. Chen, J. Liu et al., Fluorine substitution and pre-sodiation strategies to boost energy density of V-based NASICON-structured SIBs: Combined theoretical and experimental study. Chem. Eng. J. **463**, 142464 (2023). https://doi.org/10.1016/j.cej.2023.142464
28. J. Zhang, Y. Liu, X. Zhao, L. He, H. Liu et al., A novel NASICON-type Na_4 $MnCr(PO_4)_3$ demonstrating the energy density record of phosphate cathodes for sodium-ion batteries. Adv. Mater. **32**, e1906348 (2020). https://doi.org/10.1002/adma.201906348
29. X.X. Zhao, W. Fu, H.X. Zhang, J.Z. Guo, Z.Y. Gu et al., Pearl-structure-enhanced NASICON cathode toward ultrastable sodium-ion batteries. Adv. Sci. **10**, e2301308 (2023). https://doi.org/10.1002/advs.202301308
30. Q. Zhou, L. Wang, W. Li, K. Zhao, M. Liu et al., Sodium superionic conductors (NASICONs) as cathode materials for sodium-ion batteries. Electrochem. Energy Rev. **4**, 793–823 (2021). https://doi.org/10.1007/s41918-021-00120-8
31. W. Zhou, Y. Li, S. Xin, J.B. Goodenough, Rechargeable sodium all-solid-state battery. ACS Cent. Sci. **3**, 52–57 (2017). https://doi.org/10.1021/acscentsci.6b00321
32. J. Chen, S. Feng, H. Lai, Y. Lu, W. Liu et al., Interface ionic/electronic redistribution driven by conversion-alloy reaction for high-performance solid-state sodium batteries. Small Methods **8**, e2301201 (2024). https://doi.org/10.1002/smtd.202301201
33. B. Patra, R. Hegde, A. Natarajan, D. Deb, D. Sachdeva et al., Stabilizing multi-electron NASICON-$Na_{1.5}V_{0.5}Nb_{1.5}(PO_4)_3$ anode via structural modulation for long-life sodium-ion batteries. Adv. Energy Mater. **14**, 2304091 (2024). https://doi.org/10.1002/aenm.202304091
34. M. Li, C. Sun, X. Yuan, Y. Li, Y. Yuan et al., A configuration entropy enabled high-performance polyanionic cathode for sodium-ion batteries. Adv. Funct. Mater. **34**, 2314019 (2024). https://doi.org/10.1002/adfm.202314019
35. Z.L. Jian, C.C. Yuan, W.Z. Han, X. Lu, L. Gu et al., Atomic structure and kinetics of NASICON $Na_xV_2(PO_4)_3$ cathode for sodium-ion batteries. Adv. Funct. Mater. **24**, 4265–4272 (2014). https://doi.org/10.1002/adfm.201400173
36. Z. Yang, G. Li, J. Sun, L. Xie, Y. Jiang et al., High performance cathode material based on $Na_3V_2(PO_4)_2F_3$ and $Na_3V_2(PO_4)_3$ for sodium-ion batteries. Energy Storage Mater. **25**, 724–730 (2020). https://doi.org/10.1016/j.ensm.2019.09.014
37. Y. Wu, X. Meng, L. Yan, Q. Kang, H. Du et al., Vanadium-free NASICON-type electrode materials for sodium-ion batteries. J. Mater. Chem. A **10**, 21816–21837 (2022). https://doi.org/10.1039/d2ta05653d
38. Y. Zhao, Y. Zhang, Y. Li, C. Ma, X. Qi et al., Dual-complexing agent dominated synthesis of carbon coated $Na_3V_2(PO_4)_3$ cathodes for high-performance sodium ion batteries. J. Alloys Compd. **986**, 174127 (2024). https://doi.org/10.1016/j.jallcom.2024.174127
39. Z. Wang, L. Chen, K. Yang, B. Liang, X. Guo et al., Exploration of a novel vanadium source for the synthesis of a $Na_3V_2(PO_4)_3$ cathode of sodium-ion batteries. ACS Sustain Chem. Eng. **12**, 1973–1983 (2024). https://doi.org/10.1021/acssuschemeng.3c06339
40. Z.L. Jian, W.Z. Han, X. Lu, H.X. Yang, Y.S. Hu et al., Superior electrochemical performance and storage mechanism of $Na_3V_2(PO_4)_3$ cathode for room-temperature sodium-ion batteries. Adv. Energy Mater. **3**, 156–160 (2013). https://doi.org/10.1002/aenm.201200558
41. Y. Zhou, X. Yang, M. Hou, L. Zhao, X. Zhang et al., Manipulating amorphous and crystalline hybridization of $Na_3V_2(PO_4)_3$/C for enhancing sodium-ion diffusion kinetics.

J. Colloid Interface Sci. **667**, 64–72 (2024). https://doi.org/10.1016/j.jcis.2024.04.046

42. Y. Zhu, H. Xu, S. Li, Y. Chen, N-doped dual carbon-layer-modified $Na_3V_2(PO_4)_3$ as a high-performance cathode material for sodium-ion batteries. Electrochim. Acta **480**, 143895 (2024). https://doi.org/10.1016/j.electacta.2024.143895
43. G. Chen, Q. Huang, T. Wu, L. Lu, Polyanion sodium vanadium phosphate for next generation of sodium-ion batteries—a review. Adv. Funct. Mater. **30**, 2001289 (2020). https://doi.org/10.1002/adfm.202001289
44. R.S. Kate, H.S. Jadhav, U.P. Chothe, K. Bhattacharjee, M.V. Kulkarni et al., Critical review of the recent progress and challenges of polyanion $Na_3V_2(PO_4)_3$ cathode materials in rechargeable sodium-ion batteries. J. Mater. Chem. A **12**, 7418–7451 (2024). https://doi.org/10.1039/D3TA07545A
45. Q. Huang, Z. Hu, K. Chen, Z. Zeng, Y. Sun et al., Partial modification strategies of NASICON-type $Na_3V_2(PO_4)_3$ materials for cathodes of sodium-ion batteries: progress and perspectives. ACS Appl. Energy Mater. **6**, 2657–2679 (2023). https://doi.org/10.1021/acsaem.2c04083
46. R. Thirupathi, V. Kumari, S. Chakrabarty, S. Omar, Recent progress and prospects of NASICON framework electrodes for Na-ion batteries. Prog. Mater. Sci. **137**, 101128 (2023). https://doi.org/10.1016/j.pmatsci.2023.101128
47. Y. Chen, Y. Xu, X. Sun, C. Wang, Effect of Al substitution on the enhanced electrochemical performance and strong structure stability of $Na_3V_2(PO_4)_3$/C composite cathode for sodium-ion batteries. J. Power. Sources **375**, 82–92 (2018). https://doi.org/10.1016/j.jpowsour.2017.11.043
48. Y. Liu, X. Wu, A. Moeez, Z. Peng, Y. Xia et al., Na-rich $Na_3V_2(PO_4)_3$ cathodes for long cycling rechargeable sodium full cells. Adv. Energy Mater. **13**, 2203283 (2023). https://doi.org/10.1002/aenm.202203283
49. W. Song, X. Ji, Z. Wu, Y. Zhu, Y. Yang et al., First exploration of Na-ion migration pathways in the NASICON structure $Na_3V_2(PO_4)_3$. J. Mater. Chem. A **2**, 5358–5362 (2014). https://doi.org/10.1039/C4TA00230J
50. Q. Wang, M. Zhang, C. Zhou, Y. Chen, Concerted ion-exchange mechanism for sodium diffusion and its promotion in $Na_3V_2(PO_4)_3$ framework. J. Phys. Chem. C **122**, 16649–16654 (2018). https://doi.org/10.1021/acs.jpcc.8b06120
51. Z. Jian, L. Zhao, H. Pan, Y.-S. Hu, H. Li et al., Carbon coated $Na_3V_2(PO_4)_3$ as novel electrode material for sodium ion batteries. Electrochem. Commun. **14**, 86–89 (2012). https://doi.org/10.1016/j.elecom.2011.11.009
52. Z. Ahsan, Z. Cai, S. Wang, M. Moin, H. Wang et al., Recent development of phosphate based polyanion cathode materials for sodium-ion batteries. Adv. Energy Mater. **14**, 2400373 (2024). https://doi.org/10.1002/aenm.202400373
53. Y. Liu, C. Sun, Q. Ni, Z. Sun, M. Li et al., Enhanced electrochemical performance of NASICON-type sodium ion cathode based on charge balance theory. Energy Storage Mater. **53**, 881–889 (2022). https://doi.org/10.1016/j.ensm.2022.10.011
54. X. Dong, X. Zhao, Y. Chen, C. Wang, Investigations about the influence of different carbon matrixes on the electrochemical performance of $Na_3V_2(PO_4)_3$ cathode material for sodium ion batteries. Adv. Compos. Hybrid Mater. **4**, 1070–1081 (2021). https://doi.org/10.1007/s42114-021-00319-9
55. T. Akçay, M. Häringer, K. Pfeifer, J. Anhalt, J.R. Binder et al., $Na_3V_2(PO_4)_3$—a highly promising anode and cathode material for sodium-ion batteries. ACS Appl. Energy Mater. **4**, 12688–12695 (2021). https://doi.org/10.1021/acsaem.1c02413
56. W. Li, Z. Yao, C.-A. Zhou, X. Wang, X. Xia et al., Boosting high-rate sodium storage performance of N-doped carbon-encapsulated $Na_3V_2(PO_4)_3$ nanoparticles anchoring on carbon cloth. Small **15**, e1902432 (2019). https://doi.org/10.1002/smll.201902432
57. X. Jiang, L. Yang, B. Ding, B. Qu, G. Ji et al., Extending the cycle life of $Na_3V_2(PO_4)_3$ cathodes in sodium-ion batteries through interdigitated carbon scaffolding. J. Mater. Chem. A **4**, 14669–14674 (2016). https://doi.org/10.1039/C6TA05030A
58. R.S. Kate, S.V. Kadam, M.V. Kulkarni, R.J. Deokate, B.B. Kale et al., Highly stable and nanoporous $Na_3V_2(PO_4)_3$@C cathode material for sodium-ion batteries using thermal management. J. Energy Storage **74**, 109245 (2023). https://doi.org/10.1016/j.est.2023.109245
59. D. Fan, Q. Shen, H. Li, X. Qu, L. Jiao et al., Redox couple modulation in NASICON phosphates toward high-performance cathodes for Na-ion batteries. Energy Mater. Adv. **5**, 73 (2024). https://doi.org/10.34133/energymatadv.0073
60. S. Zhao, W. Qi, C. Yang, R. Ling, Triggering reversible V^{4+}/V^{5+} redox couples in $Na_3V_2(PO_4)_3$ porous flower-like cathodes by Mg^{2+} substitution for high-performance Na-ion batteries. J. Power. Sources **595**, 234076 (2024). https://doi.org/10.1016/j.jpowsour.2024.234076
61. Y. Chen, X. Liao, P. Wang, J. Chen, X. Zhang et al., A high-energy-density NASICON-type $Na_3V_{1.25}Ga_{0.75}(PO_4)_3$ cathode with reversible V^{4+}/V^{5+} redox couple for sodium ion batteries. J. Colloid Interface Sci. **653**, 1–10 (2024). https://doi.org/10.1016/j.jcis.2023.09.057
62. S. Liu, Z. Xu, L. Ren, W. Xu, Y. Liu et al., Fe-modified NASICON-type $Na_3V_2(PO_4)_3$ as a cathode material for sodium ion batteries. RSC Adv. **14**, 4835–4843 (2024). https://doi.org/10.1039/D3RA08714J
63. P.B. Madambikkattil, S.V. Nair, D. Santhanagopalan, Synergetic effect of isovalent- and aliovalent-ion dual-doping in the vanadium site of $Na_3V_2(PO_4)_3$ for wide-temperature operating sodium-ion batteries. ACS Appl. Energy Mater. **5**, 10473–10482 (2022). https://doi.org/10.1021/acsaem.2c01053
64. J. Yan, C. Zhang, Z. Li, F. Liu, H. Wang et al., Trace topological doping strategy and deep learning to reveal high-rate sodium storage regulation of barium-doped $Na_3V_2(PO_4)_3$. Nanoscale **16**, 4578–4590 (2024). https://doi.org/10.1039/D3NR04300B
65. R. Zhang, Y. Hu, J. Li, X. Zhu, Y. Peng et al., In situ constructing ultrafast ion channel for promoting high-rate cycle stability of nano-$Na_3V_2(PO_4)_3$ cathode. ACS Appl. Mater.

Interfaces **16**, 2389–2396 (2024). https://doi.org/10.1021/acsami.3c16409

66. J. Li, Y. Chen, T. Zhou, H. Shi, Z. Zheng et al., Dual-carbon coated $Na_3V_2(PO_4)_3$ derived from reduced graphene oxide and nanocellulose with porous structure for high performance sodium-ion batteries. Appl. Surf. Sci. **610**, 155553 (2023). https://doi.org/10.1016/j.apsusc.2022.155553
67. J. Cong, S.-H. Luo, P.-Y. Li, K. Li, P.-W. Li et al., Towards enhanced structural stability by investigation of the mechanism of K ion doping in $Na_3V_2(PO_4)_3$/C for sodium ion batteries. J. Energy Storage **72**, 108808 (2023). https://doi.org/10.1016/j.est.2023.108808
68. N. Li, Y. Tong, D. Yi, X. Cui, X. Zhang, 3D interconnected porous carbon coated $Na_3V_2(PO_4)_3$/C composite cathode materials for sodium-ion batteries. Ceram. Int. **46**, 27493–27498 (2020). https://doi.org/10.1016/j.ceramint.2020.07.238
69. Y. Zhu, H. Xu, J. Ma, P. Chen, Y. Chen, The N-doped carbon coated $Na_3V_2(PO_4)_3$ with different N sources as cathode material for sodium-ion batteries: experimental and theoretical study. Surf. Interfaces **45**, 103888 (2024). https://doi.org/10.1016/j.surfin.2024.103888
70. Q. Wei, X. Chang, J. Wang, T. Huang, X. Huang et al., An ultrahigh-power mesocarbon microbeads|Na^+-diglyme|$Na_3V_2(PO_4)_3$ sodium-ion battery. Adv. Mater. **34**, e2108304 (2022). https://doi.org/10.1002/adma.202108304
71. J. Cong, S.-H. Luo, P. Li, K. Li, P. Li et al., Ultracapacity properties of the refined structure in Na-rich $Na_{3.4}V_2(PO_4)_3$/C as sodium-ion battery cathodes by tapping the Na-vacancy potential. ACS Sustain Chem. Eng. **11**, 16341–16353 (2023). https://doi.org/10.1021/acssuschemeng.3c05572
72. B. Pandit, M. Johansen, C. Susana Martínez-Cisneros, J.M. Naranjo-Balseca, B. Levenfeld et al., $Na_3V_2(PO_4)_3$ cathode for room-temperature solid-state sodium-ion batteries: advanced *in situ* synchrotron X-ray studies to understand intermediate phase evolution. Chem. Mater. **36**, 2314–2324 (2024). https://doi.org/10.1021/acs.chemmater.3c02585
73. H. Shi, L. Guo, Y. Chen, Unraveling the modified mechanism of ruthenium substitution on $Na_3V_2(PO_4)_3$ with superior rate capability and ultralong cyclic performance. J. Colloid Interface Sci. **664**, 487–499 (2024). https://doi.org/10.1016/j.jcis.2024.03.061
74. J. Li, Y. Chen, H. Shi, T. Zhou, Z. Tian et al., One step in situ synthesis of $Na_3V_2(PO_4)_3$/$Na_3V_3(PO_4)_4$ biphase coexisted cathode with high energy density by inducing of polyvinylpyrrolidone for sodium ion batteries. J. Power. Sources **562**, 232802 (2023). https://doi.org/10.1016/j.jpowsour.2023.232802
75. J. Xu, E. Gu, Z. Zhang, Z. Xu, Y. Xu et al., Fabrication of porous $Na_3V_2(PO_4)_3$/reduced graphene oxide hollow spheres with enhanced sodium storage performance. J. Colloid Interface Sci. **567**, 84–91 (2020). https://doi.org/10.1016/j.jcis.2020.01.121
76. B. Zare, S.K. Sadrnezhaad, State-of-the-art design of cathodes of multivalent batteries by electrospinning: a mini review on opportunities and challenges. J. Energy Storage **82**, 110514 (2024). https://doi.org/10.1016/j.est.2024.110514
77. T. Zhu, W. Liu, X. Liao, M. Wang, H. Fan et al., A novel NASICON-type $Na_{3.5}MnCr_{0.5}Ti_{0.5}(PO_4)_3$ nanofiber with multi-electron reaction for high-performance sodium-ion batteries. Adv. Fiber Mater. **6**, 561–569 (2024). https://doi.org/10.1007/s42765-023-00367-4
78. X. Hu, X. Fan, Z. Mou, W. Kang, D. Sun, Controlled synthesis of multi-doped highly-disordered porous biomass carbon microsphere for ultra-stable and fast sodium storage. J. Energy Storage **83**, 110619 (2024). https://doi.org/10.1016/j.est.2024.110619
79. L. Yu, N. Liu, B. Liu, F. Yu, J. Ma, In-situ-derived carbon coated sea urchin-like $Na_3V_2(PO_4)_3$ from V_2C MXene for high-performance capacitive deionization. J. Alloys Compd. **965**, 171501 (2023). https://doi.org/10.1016/j.jallcom.2023.171501
80. J. Li, Y. Chen, Z. Tian, Y. Wang, L. Guo, Mechanisms and principles of $Na_3V_2(PO_4)_3$ modification by carbon materials. Curr. Opin. Electrochem. **37**, 101200 (2023). https://doi.org/10.1016/j.coelec.2022.101200
81. L. Shen, Y. Li, S. Roy, X. Yin, W. Liu et al., A robust carbon coating of $Na_3V_2(PO_4)_3$ cathode material for high performance sodium-ion batteries. Chin. Chem. Lett. **32**, 3570–3574 (2021). https://doi.org/10.1016/j.cclet.2021.03.005
82. U. Nisar, N. Muralidharan, R. Essehli, R. Amin, I. Belharouak, Valuation of surface coatings in high-energy density lithium-ion battery cathode materials. Energy Storage Mater. **38**, 309–328 (2021). https://doi.org/10.1016/j.ensm.2021.03.015
83. Z. Wang, C. Tang, Z. Wang, Q. Zhang, P. Lv et al., High-energy $Na_4MnCr(PO_4)_3$@C cathode for solid-state sodium metal batteries. Energy Mater. Adv. **4**, 0036 (2023). https://doi.org/10.34133/energymatadv.0036
84. S.Y. Gültekin, A. Güler, D. Kuruahmet, H. Güngör, M.M. Singil et al., Graphene aerogel-supported $Na_3V_2(PO_4)_3$/C cathodes for sodium-ion batteries. Diam. Relat. Mater. **139**, 110399 (2023). https://doi.org/10.1016/j.diamond.2023.110399
85. H.H. Li, H. Zhang, M. Zarrabeitia, H.P. Liang, D. Geiger et al., Metal–organic framework derived copper chalcogenides-carbon composites as high-rate and stable storage materials for Na ions. Adv. Sustain. Syst. **6**, 2200109 (2022). https://doi.org/10.1002/adsu.202200109
86. C. Luo, Q. Li, D. Shen, R. Zheng, D. Huang et al., Enhanced interfacial kinetics and fast Na^+ conduction of hybrid solid polymer electrolytes for all-solid-state batteries. Energy Storage Mater. **43**, 463–470 (2021). https://doi.org/10.1016/j.ensm.2021.09.031
87. H. Chen, M. Zhou, X. Zhang, S. Xu, H. Zhou, V-MOFs derived $Na_3V_2(PO_4)_3$/C core-shell spheres toward ultrastable sodium-ion batteries. J. Energy Storage **77**, 109932 (2024). https://doi.org/10.1016/j.est.2023.109932
88. H. Shi, Y. Chen, J. Li, L. Guo, Outstanding long cycle stability provide by bismuth doped $Na_3V_2(PO_4)_3$ enwrapped with carbon nanotubes cathode for sodium-ion batteries. J. Colloid

Interface Sci. **652**, 195–207 (2023). https://doi.org/10.1016/j.jcis.2023.08.067

89. Y. Jiang, X. Zhou, D. Li, X. Cheng, F. Liu et al., Highly reversible Na storage in $Na_3V_2(PO_4)_3$ by optimizing nanostructure and rational surface engineering. Adv. Energy Mater. **8**, 1800068 (2018). https://doi.org/10.1002/aenm.201800068
90. Y. Li, M. Chen, B. Liu, Y. Zhang, X. Liang et al., Heteroatom doping: an effective way to boost sodium ion storage. Adv. Energy Mater. **10**, 2000927 (2020). https://doi.org/10.1002/aenm.202000927
91. Z. Chen, X. Wu, Z. Sun, J. Pan, J. Han et al., Enhanced fast-charging and longevity in sodium-ion batteries through nitrogen-doped carbon frameworks encasing flower-like bismuth microspheres. Adv. Energy Mater. **14**, 2400132 (2024). https://doi.org/10.1002/aenm.202400132
92. H. Zhang, L. Wang, L. Ma, Y. Liu, B. Hou et al., Surface crystal modification of $Na_3V_2(PO_4)_3$ to cast intermediate $Na_2V_2(PO_4)_3$ phase toward high-rate sodium storage. Adv. Sci. **11**, e2306168 (2024). https://doi.org/10.1002/advs.202306168
93. T. Zhou, Y. Chen, Thiourea induced the N/S Co-doped carbon skeleton suppressing the dissolution of V to boost superior cyclic stability of $Na_3V_2(PO_4)_3$. Carbon **218**, 118778 (2024). https://doi.org/10.1016/j.carbon.2023.118778
94. C. Shi, J. Xu, T. Tao, X. Lu, G. Liu et al., Zero-strain $Na_3V_2(PO_4)_2F_3$@rGO/CNT composite as a wide-temperature-tolerance cathode for Na-ion batteries with ultrahigh-rate performance. Small Methods **8**, e2301277 (2024). https://doi.org/10.1002/smtd.202301277
95. J.C. Xi, Y.F. Yuan, M. Zhu, S.M. Yin, Y.B. Chen et al., Achieving long-life and efficient sodium storage through encapsulating Fe_3Se_4 nanoparticles within hollow mesoporous carbon nanospheres. J. Energy Storage **81**, 110499 (2024). https://doi.org/10.1016/j.est.2024.110499
96. R. Huang, D. Yan, Q. Zhang, G. Zhang, B. Chen et al., Unlocking charge transfer limitation in NASICON structured $Na_3V_2(PO_4)_3$ cathode via trace carbon incorporation. Adv. Energy Mater. **14**, 2400595 (2024). https://doi.org/10.1002/aenm.202400595
97. S. Li, Y. Dong, L. Xu, X. Xu, L. He et al., Effect of carbon matrix dimensions on the electrochemical properties of $Na_3V_2(PO_4)_3$ nanograins for high-performance symmetric sodium-ion batteries. Adv. Mater. **26**, 3545–3553 (2014). https://doi.org/10.1002/adma.201305522
98. L. Li, Y. Qin, S. Zhang, H. Zhao, J. Zhao et al., Ion transport through carbon nanotubes enable highly crystalline $Na_3V_2(PO_4)_2F_3$ cathode for ultra-stable sodium-ion storage. J. Power. Sources **576**, 233226 (2023). https://doi.org/10.1016/j.jpowsour.2023.233226
99. C. Qian, M. Shi, C. Fan, C. Liu, Q. Huang et al., Facile Al_2O_3 coating suppress dissolution of Mn^{2+} in Mn-substituted $Na_3V_2(PO_4)_3$ with outstanding electrochemical performance for full sodium ion batteries. J. Colloid Interface Sci. **664**, 573–587 (2024). https://doi.org/10.1016/j.jcis.2024.03.072
100. J. Guan, Q. Huang, L. Shao, X. Shi, D. Zhao et al., Polyanion-type $Na_3V_2(PO_4)_2F_3$@rGO with high-voltage and ultralong-life for aqueous zinc ion batteries. Small **19**, e2207148 (2023). https://doi.org/10.1002/smll.202207148
101. Z. Li, L. Yu, X. Tao, Y. Li, L. Zhang et al., Honeycomb-structured $MoSe_2$/rGO composites as high-performance anode materials for sodium-ion batteries. Small **20**, e2304124 (2024). https://doi.org/10.1002/smll.202304124
102. B. Chen, Z. Peng, Z. Yuan, Constructing sandwich structure of Nb-substituted $Na_3V_2(PO_4)_3$/C nanoparticles enwrapped on three-dimensional graphene with superior sodium storage property. Ceram. Int. **48**, 33957–33966 (2022). https://doi.org/10.1016/j.ceramint.2022.07.345
103. S. Li, H. Zhu, Y. Liu, Q. Wu, S. Cheng et al., Space-confined guest synthesis to fabricate Sn-monodispersed N-doped mesoporous host toward anode-free Na batteries. Adv. Mater. **35**, e2301967 (2023). https://doi.org/10.1002/adma.202301967
104. Y. Jiang, Z. Yang, W. Li, L. Zeng, F. Pan et al., Nanoconfined carbon-coated $Na_3V_2(PO_4)_3$ particles in mesoporous carbon enabling ultralong cycle life for sodium-ion batteries. Adv. Energy Mater. **5**, 1402104 (2015). https://doi.org/10.1002/aenm.201402104
105. N. Mubarak, F. Rehman, J. Wu, M. Ihsan-Ul-Haq, Y. Li et al., Morphology, chemistry, performance trident: Insights from hollow, mesoporous carbon nanofibers for dendrite-free sodium metal batteries. Nano Energy **86**, 106132 (2021). https://doi.org/10.1016/j.nanoen.2021.106132
106. J. Wang, X. Zhang, W. He, Y. Yue, Y. Wang et al., Layered hybrid phase $Li_2NaV_2(PO_4)_3$/carbon dot nanocomposite cathodes for Li^+/Na^+ mixed-ion batteries. RSC Adv. **7**, 2658–2666 (2017). https://doi.org/10.1039/C6RA25808E
107. Z. Tian, Y. Chen, S. Sun, H. Liu, C. Wang et al., Constructing hierarchical heterojunction structure for K/Co co-substituted $Na_3V_2(PO_4)_3$ by integrating carbon quantum dots. J. Colloid Interface Sci. **613**, 536–546 (2022). https://doi.org/10.1016/j.jcis.2021.12.195
108. S. Liu, X. Cao, Y. Zhang, K. Wang, Q. Su et al., Carbon quantum dot modified $Na_3V_2(PO_4)_2F_3$ as a high-performance cathode material for sodium-ion batteries. J. Mater. Chem. A **8**, 18872–18879 (2020). https://doi.org/10.1039/d0ta04307a
109. Y. Li, Y. Mei, R. Momen, B. Song, Y. Huang et al., Boosting the interfacial dynamics and thermodynamics in polyanion cathode by carbon dots for ultrafast-charging sodium ion batteries. Chem. Sci. **15**, 349–363 (2023). https://doi.org/10.1039/d3sc05593k
110. Y. Kim, G. Oh, J. Lee, J. Baek, G. Alfaza et al., High-voltage and high-rate cathode materials for sodium-ion batteries NASICON-type $Na_3V_{1.5}Cr_{0.4}Fe_{0.1}(PO_4)_3$ ACS Appl. Mater. Interfaces **16**(5896), 5904 (2024). https://doi.org/10.1021/acsami.3c17166
111. R. Chen, X. Zhang, D. Li, Y. Li, S. Li et al., Novel NASICON-type Na-V-Mn-Ni-containing cathodes for high-rate and long-life SIBs. Small **20**, e2306589 (2024). https://doi.org/10.1002/smll.202306589

112. Z.-Y. Gu, J.-Z. Guo, J.-M. Cao, X.-T. Wang, X.-X. Zhao et al., An advanced high-entropy fluorophosphate cathode for sodium-ion batteries with increased working voltage and energy density. Adv. Mater. **34**, e2110108 (2022). https://doi.org/10.1002/adma.202110108
113. S. Sun, S. Liu, Y. Chen, L. Li, Q. Bai et al., Quantum physics and deep learning to reveal multiple dimensional modified regulation by ternary substitution of iron, manganese, and cobalt on $Na_3V_2(PO_4)_3$ for superior sodium storage. Adv. Funct. Mater. **33**, 2213711 (2023). https://doi.org/10.1002/adfm.202213711
114. K. Wang, C. Gao, J. Tu, K. Guo, Y.-L. Ding, Na-site coordination environment regulation of Mn-based phosphate cathodes for sodium-ion batteries with elevated working voltage and energy density. J. Mater. Chem. A **12**, 6681–6692 (2024). https://doi.org/10.1039/D3TA07300A
115. A. Das, S.B. Majumder, A. Roy, Chaudhuri K^+ and Mg^{2+} Co-doped bipolar $Na_3V_2(PO_4)_3$: an ultrafast electrode for symmetric sodium ion full cell. J. Power. Sources **461**, 228149 (2020). https://doi.org/10.1016/j.jpowsour.2020.228149
116. H. Yu, Y. Gao, J. Wang, Q. Liang, J. Kang et al., Potassium doping towards enhanced Na-ion diffusivity in a fluorophosphate cathode for sodium-ion full cells. J. Mater. Chem. A **10**, 22105–22113 (2022). https://doi.org/10.1039/D2TA05593G
117. L. Shen, Y. Li, C. Hu, Z. Huang, B. Wang et al., A high-rate cathode material based on potassium-doped $Na_3V_2(PO_4)_3$ for high/low-temperature sodium-ion batteries. Mater. Today Chem. **30**, 101506 (2023). https://doi.org/10.1016/j.mtchem.2023.101506
118. J. Cong, S.-H. Luo, P.-Y. Li, X. Yan, L.-X. Qian et al., Stable cycling performance of lituium-doping $Na_{3-x}Li_xV_2(PO_4)_3$/C ($0 \leq x \leq 0.4$) cathode materials by Na-site manipulation strategy. Appl. Surf. Sci. **643**, 158646 (2024). https://doi.org/10.1016/j.apsusc.2023.158646
119. Q. Tao, H. Ding, H. Zhao, J. Huang, B. Dai et al., Ca-doped Na-site $NaNi_{1/3}Fe_{1/3}Mn_{1/3}O_2$ as a high-performance cathode material for sodium ion batteries. J. Alloys Compd. **976**, 172977 (2024). https://doi.org/10.1016/j.jallcom.2023.172977
120. M. Matsui, F. Mizukoshi, H. Hasegawa, N. Imanishi, Ca-substituted P3-type $Na_xNi_{1/3}Mn_{1/3}Co_{1/3}O_2$ as a potential high voltage cathode active material for sodium-ion batteries. J. Power. Sources **485**, 229346 (2021). https://doi.org/10.1016/j.jpowsour.2020.229346
121. P. Chen, C. Wu, Z. Wang, S. Li, X. Xu et al., Synergistically boosting sodium-storage performance of $Na_3V_2(PO_4)_3$ by regulating Na sites and constructing 3D interconnected carbon nanosheet frameworks. ACS Appl. Energy Mater. **5**, 2542–2552 (2022). https://doi.org/10.1021/acsaem.1c04061
122. A. Rudola, R. Sayers, C.J. Wright, J. Barker, Opportunities for moderate-range electric vehicles using sustainable sodium-ion batteries. Nat. Energy **8**, 215–218 (2023). https://doi.org/10.1038/s41560-023-01215-w
123. X. Shen, M. Han, Y. Su, M. Wang, F. Wu, Alkali metal ion induced lattice regulation for all climate NASICON-type cathode with superior Na-storage performance. Nano Energy **114**, 108640 (2023). https://doi.org/10.1016/j.nanoen.2023.108640
124. M. Chen, W. Hua, J. Xiao, J. Zhang, V.W. Lau et al., Activating a multielectron reaction of NASICON-structured cathodes toward high energy density for sodium-ion batteries. J. Am. Chem. Soc. **143**, 18091–18102 (2021). https://doi.org/10.1021/jacs.1c06727
125. P. Hu, T. Zhu, C. Cai, X. Wang, L. Zhang et al., A high-energy NASICON-type $Na_{3.2}MnTi_{0.8}V_{0.2}(PO_4)_3$ cathode material with reversible 3.2-electron redox reaction for sodium-ion batteries. Angew. Chem. Int. Ed. **62**, e202219304 (2023). https://doi.org/10.1002/anie.202219304
126. Z.-Y. Gu, X.-X. Zhao, K. Li, J.-M. Cao, X.-T. Wang et al., Homeostatic solid solution reaction in phosphate cathode: breaking high-voltage barrier to achieve high energy density and long life of sodium-ion batteries. Adv. Mater. **36**, e2400690 (2024). https://doi.org/10.1002/adma.202400690
127. H. Dong, C. Liu, Q. Huang, Y. Chen, Se-induced defective carbon nanotubes promoting superior kinetics and electrochemical performance in $Na_3V_2(PO_4)_3$ for half and full Na ion cells. J. Colloid Interface Sci. **660**, 277–289 (2024). https://doi.org/10.1016/j.jcis.2024.01.087
128. H. Dong, C. Liu, Q. Huang, Z. Sun, T. Liang et al., Sc^{3+} substituted $Na_3V_2(PO_4)_3$ on N-doped porous carbon skeleton boosting high structural stability and superior electrochemical performance for full sodium ion batteries. J. Colloid Interface Sci. **667**, 371–384 (2024). https://doi.org/10.1016/j.jcis.2024.04.105
129. Y. Chen, Q. Li, P. Wang, X. Liao, J. Chen et al., High-energy-density cathode achieved via the activation of a three-electron reaction in sodium manganese vanadium phosphate for sodium-ion batteries. Small **19**, e2304002 (2023). https://doi.org/10.1002/smll.202304002
130. Q. Hu, J.-Y. Liao, X.-D. He, S. Wang, L.-N. Xiao et al., In situ catalytic formation of graphene-like graphitic layer decoration on $Na_3V_{2-x}Ga_x(PO_4)_3$ ($0 \leq x \leq 0.6$) for ultrafast and high energy sodium storage. J. Mater. Chem. A **7**, 4660–4667 (2019). https://doi.org/10.1039/C8TA11890F
131. X. Liu, G. Feng, E. Wang, H. Chen, Z. Wu et al., Insight into preparation of Fe-doped $Na_3V_2(PO_4)_3$@C from aspects of particle morphology design, crystal structure modulation, and carbon graphitization regulation. ACS Appl. Mater. Interfaces **11**, 12421–12430 (2019). https://doi.org/10.1021/acsami.8b21257
132. Y. Zhao, X. Gao, H. Gao, H. Jin, J.B. Goodenough, Three electron reversible redox reaction in sodium vanadium chromium phosphate as a high-energy-density cathode for sodium-ion batteries. Adv. Funct. Mater. **30**, 1908680 (2020). https://doi.org/10.1002/adfm.201908680
133. R. Liu, G. Xu, Q. Li, S. Zheng, G. Zheng et al., Exploring highly reversible 1.5-electron reactions ($V^{3+}/V^{4+}/V^{5+}$) in $Na_3VCr(PO_4)_3$ cathode for sodium-ion batteries. ACS Appl. Mater. Interfaces **9**, 43632–43639 (2017). https://doi.org/10.1021/acsami.7b13018
134. W. Zhang, Y.L. Wu, Z.M. Xu, H.X. Li, M. Xu et al., Rationally designed sodium chromium vanadium phosphate

cathodes with multi-electron reaction for fast-charging sodium-ion batteries. Adv. Energy Mater. **12**, 2201065 (2022). https://doi.org/10.1002/aenm.202201065

135. J. Lee, S. Park, Y. Park, J. Song, B. Sambandam et al., Chromium doping into NASICON-structured $Na_3V_2(PO_4)_3$ cathode for high-power Na-ion batteries. Chem. Eng. J. **422**, 130052 (2021). https://doi.org/10.1016/j.cej.2021.130052
136. B. Mai, B. Xing, Y. Yue, N. Cai, C. Cai et al., Cr-doped $Na_3V_2(PO_4)_3$@C enables high-capacity with V^{2+}/V^{5+} reaction and stable sodium storage. J. Mater. Sci. Technol. **165**, 1–7 (2023). https://doi.org/10.1016/j.jmst.2023.05.005
137. Y. Lu, L. Wang, J. Song, D. Zhang, M. Xu et al., Aluminum-stabilized NASICON-structured $Li_3V_2(PO_4)_3$. J. Mater. Chem. A **1**, 68–72 (2013). https://doi.org/10.1039/c2ta00029f
138. G. Taveri, A. Güneren, M. Barlog, M. Hnatko, I. Zhukova et al., Understanding the benefits of Al^{3+}-doping on NaSICONs explained through an out-of-the-scheme isovalent substitution of Fe^{3+} in $Na_3Fe_2(PO_4)_3$ series. J. Power. Sources **592**, 233917 (2024). https://doi.org/10.1016/j.jpowsour.2023.233917
139. Q. Wang, H. Gao, J. Li, G.-B. Liu, H. Jin, Importance of crystallographic sites on sodium-ion extraction from NASICON-structured cathodes for sodium-ion batteries. ACS Appl. Mater. Interfaces **13**, 14312–14320 (2021). https://doi.org/10.1021/acsami.1c01663
140. Q.-Y. Zhao, J.-Y. Li, M.-J. Chen, H. Wang, Y.-T. Xu et al., Bimetal substitution enabled energetic polyanion cathode for sodium-ion batteries. Nano Lett. **22**, 9685–9692 (2022). https://doi.org/10.1021/acs.nanolett.2c03916
141. F. Lalère, V. Seznec, M. Courty, R. David, J.N. Chotard et al., Improving the energy density of $Na_3V_2(PO_4)_3$-based positive electrodes through V/Al substitution. J. Mater. Chem. A **3**, 16198–16205 (2015). https://doi.org/10.1039/C5TA03528G
142. C. Sun, Y. Zhao, Q. Ni, Z. Sun, X. Yuan et al., Reversible multielectron redox in NASICON cathode with high energy density for low-temperature sodium-ion batteries. Energy Storage Mater. **49**, 291–298 (2022). https://doi.org/10.1016/j.ensm.2022.04.025
143. X. Liu, Y. Chen, P. Wang, Q. Zheng, Y. Huo et al., Activating three electron reaction in sodium vanadium ferric phosphate toward high energy density for Na-ion batteries. J. Alloys Compd. **972**, 172890 (2024). https://doi.org/10.1016/j.jallcom.2023.172890
144. M.J. Aragón, P. Lavela, G.F. Ortiz, J.L. Tirado, Effect of iron substitution in the electrochemical performance of $Na_3V_2(PO_4)_3$ as cathode for Na-ion batteries. J. Electrochem. Soc. **162**, A3077–A3083 (2015). https://doi.org/10.1149/2.0151502jes
145. T. Zhou, Y. Chen, Heterojunction of Y^{3+}−substituted $Na_3V_2(PO_4)_3$-$NaYO_2$ accelerating kinetics with superior performance for full sodium-ion batteries. J. Colloid Interface Sci. **654**, 1163–1176 (2024). https://doi.org/10.1016/j.jcis.2023.10.124
146. X. Shen, Y. Su, S. He, Y. Li, L. Xu et al., A zero-strain Na-deficient NASICON-type $Na_{2.8}Mn_{0.4}V_{1.0}Ti_{0.6}(PO_4)_3$ cathode for wide-temperature rechargeable Na-ion batteries. J. Mater. Chem. A **11**, 16860–16870 (2023). https://doi.org/10.1039/D3TA03555G
147. B. Li, D. Xiao, C. Shang, X. Wang, M. Yan et al., Superior reversibility of NASICON-$Na_{3.5}Mn_{0.5}V_{1.5}(PO_4)_3$ cathode enabled by dual-carbon conductive network. J. Alloys Compd. **977**, 173259 (2024). https://doi.org/10.1016/j.jallcom.2023.173259
148. Z. Wang, G. Cui, Q. Zheng, X. Ren, Q. Yang et al., Ultrafast charge-discharge capable and long-life $Na_{3.9}Mn_{0.95}Zr_{0.05}V(PO_4)_3$/C cathode material for advanced sodium-ion batteries. Small **19**, e2206987 (2023). https://doi.org/10.1002/smll.202206987
149. J. Fang, S. Wang, X. Yao, X. Hu, Y. Wang et al., Ration design of porous Mn-doped $Na_3V_2(PO_4)_3$ cathode for high rate and super stable sodium-ion batteries. Electrochim. Acta **295**, 262–269 (2019). https://doi.org/10.1016/j.electacta.2018.10.150
150. M.V. Zakharkin, O.A. Drozhzhin, S.V. Ryazantsev, D. Chernyshov, M.A. Kirsanova et al., Electrochemical properties and evolution of the phase transformation behavior in the NASICON-type $Na_{3+x}Mn_xV_{2-x}(PO_4)_3$ ($0 \leq x \leq 1$) cathodes for Na-ion batteries. J. Power. Sources **470**, 228231 (2020). https://doi.org/10.1016/j.jpowsour.2020.228231
151. S. Ghosh, N. Barman, M. Mazumder, S.K. Pati, G. Rousse et al., High capacity and high-rate NASICON-$Na_{3.75}V_{1.25}Mn_{0.75}(PO_4)_3$ cathode for Na-ion batteries via modulating electronic and crystal structures. Adv. Energy Mater. **10**, 1902918 (2020). https://doi.org/10.1002/aenm.201902918
152. J. Zhang, X. Zhao, Y. Song, Q. Li, Y. Liu et al., Understanding the superior sodium-ion storage in a novel $Na_{3.5}Mn_{0.5}V_{1.5}(PO_4)_3$ cathode. Energy Storage Mater. **23**, 25–34 (2019). https://doi.org/10.1016/j.ensm.2019.05.041
153. F. Lu, J. Wang, S. Chang, L. He, M. Tang et al., New-type NASICON-$Na_4FeV(PO_4)_3$ cathode with high retention and durability for sodium ion batteries. Carbon **196**, 562–572 (2022). https://doi.org/10.1016/j.carbon.2022.05.033
154. S. Park, J.-N. Chotard, D. Carlier, I. Moog, M. Duttine et al., An asymmetric sodium extraction/insertion mechanism for the Fe/V-mixed NASICON $Na_4FeV(PO_4)_3$. Chem. Mater. **34**, 4142–4152 (2022). https://doi.org/10.1021/acs.chemmater.2c00501
155. B.M. de Boisse, J. Ming, S.-I. Nishimura, A. Yamada, Alkaline excess strategy to NASICON-type compounds towards higher-capacity battery electrodes. J. Electrochem. Soc. **163**, A1469–A1473 (2016). https://doi.org/10.1149/2.0041608jes
156. S. Park, J.-N. Chotard, D. Carlier, I. Moog, M. Courty et al., Crystal structures and local environments of NASICON-type $Na_3FeV(PO_4)_3$ and $Na_4FeV(PO_4)_3$ positive electrode materials for Na-ion batteries. Chem. Mater. **33**, 5355–5367 (2021). https://doi.org/10.1021/acs.chemmater.1c01457
157. C. Wang, J. Xiu, K. Lü, Y. Li, M. Wei, Compositing pine pollen derived carbon matrix with $Na_4FeV(PO_4)_3$ nanoparticle for cost-effective sodium-ion batteries cathode. J. Colloid

Interface Sci. **667**, 510–519 (2024). https://doi.org/10.1016/j.jcis.2024.04.143

158. C. Xu, J. Zhao, Y.-A. Wang, W. Hua, Q. Fu et al., Reversible activation of V^{4+}/V^{5+} redox couples in NASICON phosphate cathodes. Adv. Energy Mater. **12**, 2200966 (2022). https://doi.org/10.1002/aenm.202200966
159. M. Hadouchi, N. Yaqoob, P. Kaghazchi, M. Tang, J. Liu et al., Fast sodium intercalation in $Na_{3.41}£_{0.59}FeV(PO_4)_3$: a novel sodium-deficient NASICON cathode for sodium-ion batteries. Energy Storage Mater. **35**, 192–202 (2021). https://doi.org/10.1016/j.ensm.2020.11.010
160. Y. Zhou, G. Xu, J. Lin, Y. Zhang, G. Fang et al., Reversible multielectron redox chemistry in a NASICON-type cathode toward high-energy-density and long-life sodium-ion full batteries. Adv. Mater. **35**, e2304428 (2023). https://doi.org/10.1002/adma.202304428
161. R. Chen, D.S. Butenko, S. Li, D. Li, X. Zhang et al., Effects of low doping on the improvement of cathode materials $Na_{3+x}V_{2-x}M_x(PO_4)_3$ ($M = Co^{2+}$, Cu^{2+}; $x = 0.01–0.05$) for SIBs. J. Mater. Chem. A **9**, 17380–17389 (2021). https://doi.org/10.1039/D1TA05000A
162. C. Liu, C. Qian, H. Dong, Z. Lu, Q. Huang et al., Defect regulation of Co^{2+} substituting V^{3+} in $Na_3V_2(PO_4)_3$ for superior sodium storage performance: experimental and theoretical study. Compos. Commun. **40**, 101610 (2023). https://doi.org/10.1016/j.coco.2023.101610
163. M. Jiang, D. Xu, B. Yang, C. Zhang, M. Cao, Oxygen vacancy engineering in $Na_3V_2(PO_4)_3$ for boosting sodium storage kinetics. Adv. Mater. Interfaces **8**, 2100188 (2021). https://doi.org/10.1002/admi.202100188
164. M. Akhtar, S.B. Majumder, Effect of nickel doping on the electrochemical performances of carbon-coated $Na_3V_2(PO_4)_3$ cathodes for hybrid lithium-ion batteries. ACS Appl. Energy Mater. **4**, 13538–13549 (2021). https://doi.org/10.1021/acsaem.1c02080
165. B. Zhang, H. Chen, H. Tong, X. Wang, J. Zheng et al., Synthesis and electrochemical performance of Ni doped $Na_3V_2(PO_4)_3$/C cathode materials for sodium ion batteries. J. Alloys Compd. **728**, 976–983 (2017). https://doi.org/10.1016/j.jallcom.2017.09.020
166. H. Li, X. Yu, Y. Bai, F. Wu, C. Wu et al., Effects of Mg doping on the remarkably enhanced electrochemical performance of $Na_3V_2(PO_4)_3$ cathode materials for sodium ion batteries. J. Mater. Chem. A **3**, 9578–9586 (2015). https://doi.org/10.1039/C5TA00277J
167. A. Inoishi, Y. Yoshioka, L. Zhao, A. Kitajou, S. Okada, Improvement in the energy density of $Na_3V_2(PO_4)_3$ by Mg substitution. ChemElectroChem **4**, 2755–2759 (2017). https://doi.org/10.1002/celc.201700540
168. S. Ghosh, N. Barman, E. Gonzalez-Correa, M. Mazumder, A. Zaveri et al., Elucidating the impact of Mg substitution on the properties of NASICON-$Na_{3+y}V_{2-y}Mg_y(PO_4)_3$ cathodes. Adv. Funct. Mater. **31**, 2105463 (2021). https://doi.org/10.1002/adfm.202105463
169. D.A. Puspitasari, J. Patra, R.F.H. Hernandha, Y.S. Chiang, A. Inoishi et al., Enhanced electrochemical performance of Ca-doped $Na_3V_2(PO_4)_2F_3$/C cathode materials for sodium-ion batteries. ACS Appl. Mater. Interfaces **16**, 496–506 (2024). https://doi.org/10.1021/acsami.3c12772
170. L. Zhao, H. Zhao, Z. Du, J. Wang, X. Long et al., Delicate lattice modulation enables superior Na storage performance of $Na_3V_2(PO_4)_3$ as both an anode and cathode material for sodium-ion batteries: understanding the role of calcium substitution for vanadium. J. Mater. Chem. A **7**, 9807–9814 (2019). https://doi.org/10.1039/C9TA00869A
171. X. Jiang, C. Liu, Z. Tian, S. Sun, J. Li et al., Constructing p-type substitution induced by Ca^{2+} in defective $Na_3V_{2-x}Ca_x(PO_4)_3$/C wrapped with conductive CNTs for high-performance sodium-ion batteries. Dalton Trans. **51**, 16145–16157 (2022). https://doi.org/10.1039/d2dt02602c
172. S. Tong, H. Pan, H. Liu, X. Zhang, X. Liu et al., Titanium doping induced the suppression of irreversible phase transformation at high voltage for V-based phosphate cathodes of Na-ion batteries. ChemSusChem **16**, e202300244 (2023). https://doi.org/10.1002/cssc.202300244
173. D. Wang, X. Bie, Q. Fu, D. Dixon, N. Bramnik et al., Sodium vanadium titanium phosphate electrode for symmetric sodium-ion batteries with high power and long lifespan. Nat. Commun. **8**, 15888 (2017). https://doi.org/10.1038/ncomms15888
174. H. Ding, X. He, Q. Tao, J. Teng, J. Li, Ti-doped $Na_3v_2(PO_4)_3$ activates additional Ti^{3+}/Ti^{4+} and V^{4+}/V^{5+} redox pairs for superior sodium ion storage. Energy Fuels **37**, 4132–4142 (2023). https://doi.org/10.1021/acs.energyfuels.3c00242
175. Y. Huang, X. Li, J. Wang, L. Miao, C. Li et al., Superior Na-ion storage achieved by Ti substitution in $Na_3V_2(PO_4)_3$. Energy Storage Mater. **15**, 108–115 (2018). https://doi.org/10.1016/j.ensm.2018.03.021
176. X. Li, Y. Huang, J. Wang, L. Miao, Y. Li et al., High valence Mo-doped $Na_3V_2(PO_4)_3$/C as a high rate and stable cycle-life cathode for sodium battery. J. Mater. Chem. A **6**, 1390–1396 (2018). https://doi.org/10.1039/C7TA08970H
177. X.-X. Zhao, X.-T. Wang, Z.-Y. Gu, J.-Z. Guo, J.-M. Cao et al., Unlocking quasi-monophase behavior in NASICON cathode to drive fast-charging toward durable sodium-ion batteries. Adv. Funct. Mater. (2024). https://doi.org/10.1002/adfm.202402447
178. Y. Liu, C. Sun, Y. Li, H. Jin, Y. Zhao, Recent progress of Mn-based NASICON-type sodium ion cathodes. Energy Storage Mater. **57**, 69–80 (2023). https://doi.org/10.1016/j.ensm.2023.02.005
179. W. Fu, B. Li, P. Wang, Z. Lin, K. Zhu, A high-entropy carbon-coated $Na_3V_{1.9}(Mg, Cr, Al, Mo, Nb)_{0.1}(PO_4)_2F_3$ cathode for superior performance sodium-ion batteries. Ceram. Int. **50**, 16166–16171 (2024). https://doi.org/10.1016/j.ceramint.2024.02.096
180. M. Li, C. Sun, Q. Ni, Z. Sun, Y. Liu et al., High entropy enabling the reversible redox reaction of V^{4+}/V^{5+} couple in NASICON-type sodium ion cathode. Adv. Energy Mater. **13**, 2203971 (2023). https://doi.org/10.1002/aenm.202203971
181. Z. Hao, X. Shi, W. Zhu, Z. Yang, X. Zhou et al., Boosting multielectron reaction stability of sodium vanadium

phosphate by high-entropy substitution. ACS Nano **18**, 9354–9364 (2024). https://doi.org/10.1021/acsnano.3c09519

182. H. Li, M. Xu, H. Long, J. Zheng, L. Zhang et al., Stabilization of multicationic redox chemistry in polyanionic cathode by increasing entropy. Adv. Sci. **9**, e2202082 (2022). https://doi.org/10.1002/advs.202202082
183. M.-Y. Wang, J.-Z. Guo, Z.-W. Wang, Z.-Y. Gu, X.-J. Nie et al., Isostructural and multivalent anion substitution toward improved phosphate cathode materials for sodium-ion batteries. Small **16**, e1907645 (2020). https://doi.org/10.1002/smll.201907645
184. V. Kapoor, B. Singh, G. Sai Gautam, A.K. Cheetham, P. Canepa, Rational design of mixed polyanion electrodes $Na_xV_2P_{3-i}(Si/S)_iO_{12}$ for sodium batteries. Chem. Mater. **34**, 3373–3382 (2022). https://doi.org/10.1021/acs.chemmater.2c00230
185. P. Hu, X. Wang, T. Wang, L. Chen, J. Ma et al., Boron substituted $Na_3V_2(P_{1-x}B_xO_4)_3$ cathode materials with enhanced performance for sodium-ion batteries. Adv. Sci. **3**, 1600112 (2016). https://doi.org/10.1002/advs.201600112
186. Q. Qiu, C. Li, H. Liu, Y. Liao, C. Zhao et al., NMR evidence for the multielectron reaction mechanism of $Na_3V_2(PO_4)_3$ cathode and the impact of polyanion site substitution. J. Phys. Chem. C **125**, 15200–15209 (2021). https://doi.org/10.1021/acs.jpcc.1c04099
187. X. Liu, J. Gong, X. Wei, L. Ni, H. Chen et al., MoO42– mediated engineering of $Na_3V_2(PO_4)_3$ as advanced cathode materials for sodium-ion batteries. J. Colloid Interface Sci. **606**, 1897–1905 (2022). https://doi.org/10.1016/j.jcis.2021.10.007
188. T. Zhou, Y. Chen, Constructing heterostructure by co-doping of Ta^{5+} and F^- with carbon nanotubes to improve kinetic properties of $Na_3V_2(PO_4)_3$. J. Energy Storage **85**, 111139 (2024). https://doi.org/10.1016/j.est.2024.111139
189. Z.J. Song, Y.H. Liu, Z.X. Guo, Z.D. Liu, Z.K. Li et al., Ultrafast synthesis of large-sized and conductive $Na_3V_2(PO_4)_2F$ simultaneously approaches high tap density, rate and cycling capability. Adv. Funct. Mater. **34**, 2313998 (2024). https://doi.org/10.1002/adfm.202313998
190. J. Wang, Q. Liu, S. Cao, H. Zhu, Y. Wang, Boosting sodium-ion battery performance with binary metal-doped $Na_3V_2(PO_4)_2F_3$ cathodes. J. Colloid Interface Sci. **665**, 1043–1053 (2024). https://doi.org/10.1016/j.jcis.2024.04.003
191. Y. Chen, Y. Xu, X. Sun, B. Zhang, S. He et al., Preventing structural degradation from $Na_3V_2(PO_4)_3$ to $V_2(PO_4)_3$: F-doped $Na_3V_2(PO_4)_3$/C cathode composite with stable lifetime for sodium ion batteries. J. Power. Sources **378**, 423–432 (2018). https://doi.org/10.1016/j.jpowsour.2017.12.073
192. Y. Chen, Y. Xu, X. Sun, B. Zhang, S. He et al., F-doping and V-defect synergetic effects on $Na_3V_2(PO_4)_3$/C composite: a promising cathode with high ionic conductivity for sodium ion batteries. J. Power. Sources **397**, 307–317 (2018). https://doi.org/10.1016/j.jpowsour.2018.07.006
193. P. Li, M. Gao, D. Wang, Z. Li, Y. Liu et al., Optimizing vanadium redox reaction in $Na_3V_2(PO_4)_3$ cathodes for sodium-ion batteries by the synergistic effect of additional electrons from heteroatoms. ACS Appl. Mater. Interfaces **15**, 9475–9485 (2023). https://doi.org/10.1021/acsami.2c22038
194. S.K. Pal, R. Thirupathi, S. Chakrabarty, S. Omar, Improving the electrochemical performance of $Na_3V_2(PO_4)_3$ cathode in Na-ion batteries by Si-doping. ACS Appl. Energy Mater. **3**, 12054–12065 (2020). https://doi.org/10.1021/acsaem.0c02188
195. Y. Chen, J. Cheng, Z. He, Y. Wang, C. Wang et al., Silicon substituted $Na_3V_2(PO_4)_3$/C nanocomposites enwrapped on conducting graphene for high-rate and long-lifespan sodium ion batteries. Ceram. Int. **46**, 27660–27669 (2020). https://doi.org/10.1016/j.ceramint.2020.07.262
196. J. Cheng, Y. Chen, Y. Wang, C. Wang, Z. He et al., Insights into the enhanced sodium storage property and kinetics based on the Zr/Si codoped $Na_3V_2(PO_4)_3$/C cathode with superior rate capability and long lifespan. J. Power. Sources **474**, 228632 (2020). https://doi.org/10.1016/j.jpowsour.2020.228632
197. M. Dou, Y. Zhang, J. Wang, X. Zheng, J. Chen et al., Simultaneous cation-anion regulation of sodium vanadium phosphate cathode materials for high-energy and cycle-stable sodium-ion batteries. J. Power. Sources **560**, 232709 (2023). https://doi.org/10.1016/j.jpowsour.2023.232709
198. Y. Chen, J. Cheng, S. Sun, Z. Tian, X. Jiang et al., Constructing hierarchical porous Fe/F-codoped $Na_3V_2(PO_4)_3$/C composite enwrapped with carbon nanotubes as high-performance cathode for symmetric sodium ion batteries. J. Power. Sources **513**, 230545 (2021). https://doi.org/10.1016/j.jpowsour.2021.230545
199. Y. Chen, Z. Tian, J. Li, T. Zhou, *In-situ* constructing pearl necklace-shaped heterostructure: Zn^{2+} substituted $Na_3V_2(PO_4)_3$ attached on carbon nano fibers with high performance for half and full Na ion cells. Chem. Eng. J. **472**, 145041 (2023). https://doi.org/10.1016/j.cej.2023.145041
200. L. Wu, S. Shi, X. Zhang, Y. Yang, J. Liu et al., Room-temperature pre-reduction of spinning solution for the synthesis of $Na_3V_2(PO_4)_3$/C nanofibers as high-performance cathode materials for Na-ion batteries. Electrochim. Acta **274**, 233–241 (2018). https://doi.org/10.1016/j.electacta.2018.04.122
201. C. Liu, Z.-X. Zhang, R. Tan, J.-W. Deng, Q.-H. Li et al., Design of cross-welded $Na_3V_2(PO_4)_3$/C nanofibrous mats and their application in sodium-ion batteries. Rare Met. **41**, 806–813 (2022). https://doi.org/10.1007/s12598-021-01825-x
202. S. Sun, Y. Chen, Q. Bai, Z. Tian, Q. Huang et al., Unravelling the regulation mechanism of nanoflower shaped $Na_3V_2(PO_4)_3$ in methanol–water system for high performance sodium ion batteries. Chem. Eng. J. **451**, 138780 (2023). https://doi.org/10.1016/j.cej.2022.138780
203. W. Ren, Z. Zheng, C. Xu, C. Niu, Q. Wei et al., Self-sacrificed synthesis of three-dimensional $Na_3V_2(PO_4)_3$ nanofiber network for high-rate sodium–ion full batteries. Nano Energy **25**, 145–153 (2016). https://doi.org/10.1016/j.nanoen.2016.03.018
204. X. Li, S. Wang, X. Tang, R. Zang, P. Li et al., Porous $Na_3V_2(PO_4)_3$/C nanoplates for high-performance sodium

storage. J. Colloid Interface Sci. **539**, 168–174 (2019). https://doi.org/10.1016/j.jcis.2018.12.071

205. M. Guo, J. Wang, H. Dou, G. Gao, S. Wang et al., Agglomeration-resistant 2D nanoflakes configured with super electronic networks for extraordinary fast and stable sodium-ion storage. Nano Energy **56**, 502–511 (2019). https://doi.org/10.1016/j.nanoen.2018.11.091
206. Y. Zhou, X. Zhang, Y. Liu, X. Xie, X. Rui et al., A high-temperature Na-ion battery: boosting the rate capability and cycle life by structure engineering. Small **16**, e1906669 (2020). https://doi.org/10.1002/smll.201906669
207. Q. Su, Y. Zhou, J. Zhu, H. Chang, M. Hou et al., Nanoflake-assembled hierarchical $Na_3V_2(PO_4)_3$@C microspheres for ultrafast and highly durable sodium storage. ACS Appl. Energy Mater. **6**, 10128–10136 (2023). https://doi.org/10.1021/acsaem.3c01871
208. X. Cao, A. Pan, B. Yin, G. Fang, Y. Wang et al., Nanoflake-constructed porous $Na_3V_2(PO_4)_3$/C hierarchical microspheres as a bicontinuous cathode for sodium-ion batteries applications. Nano Energy **60**, 312–323 (2019). https://doi.org/10.1016/j.nanoen.2019.03.066
209. Y. Wang, G. Su, X. Li, L. Hou, L. Liang et al., Boosting sodium-storage properties of hierarchical $Na_3V_2(PO_4)_3$@C micro-flower cathodes by tiny Cr doping: The effect of "four ounces moving a thousand pounds". Nano Res. **17**, 235–244 (2024). https://doi.org/10.1007/s12274-023-5555-8
210. H. Chen, Y. Yang, R. Nie, C. Li, S. Xu et al., Micro-nano $Na_3V_2(PO_4)_3$/C derived from metal-organic frameworks for high performance sodium ion batteries. J. Alloys Compd. **932**, 167695 (2023). https://doi.org/10.1016/j.jallcom.2022.167695
211. J. Yang, D. Li, X. Wang, X. Zhang, J. Xu et al., Constructing micro-nano $Na_3V_2(PO_4)_3$/C architecture for practical high-loading electrode fabrication as superior-rate and ultralong-life sodium ion battery cathode. Energy Storage Mater. **24**, 694–699 (2020). https://doi.org/10.1016/j.ensm.2019.07.002